AXISYMMETRIC JET IMPINGEMENT ONTO A HEATED CYLINDER

AXISYMMETRIC JET IMPINGEMENT ONTO A HEATED CYLINDER

By
DAVID ANDRÉ JOYAL
B.Math (University of Waterloo)
BBA (Wilfrid Laurier University)

A Thesis Submitted to the School of Graduate Studies in Partial Fulfilment of the Requirements
for the Degree of Master of Applied Science

McMaster University

MASTER OF APPLIED SCIENCE (2017)
(Engineering Physics)

MCMASTER UNIVERSITY
Hamilton, Ontario, Canada

TITLE: Axisymmetric Jet Impingement onto a Heated Cylinder

AUTHOR: David André Joyal, B.Math, BBA

SUPERVISOR: Dr. D. R. Novog

NUMBER OF PAGES: xi, 89

ABSTRACT

The prediction of the flows and temperatures in the moderator system of CANDU reactors is important in the safety evaluation during some potential transients. An experimental program to collect data for CFD validation, including integrated moderator circulation tests has been funded by the CANDU Owners Group. This thesis constitutes a separate effect test within this larger moderator flow study, investigating the behaviour of a jet impinging onto a single heated cylinder.

A number of experiments were conducted to investigate the behaviour of the jet flow under a variety of scenarios. The inlet Reynolds number and the heater power level were the primary variables considered to assess the impact of the buoyant forces generated by the heated cylinder on the flow. Alongside the experiments, simulations were performed using the experimental geometry to evaluate the performance of some of the most commonly-used turbulence modelling approaches – namely the standard k-ε, realizable k-ε, and standard k-ω RANS models.

The agreement between the turbulence models and experimental results was determined to be reasonable in the free jet regions, however nearer the cylinder, the simulated results exhibited a wider core region and steeper gradient in the shear layer than the experimental data. At lower Reynolds numbers, over-prediction of velocities both in the axial and lateral direction was also seen. The impact of heating proved minimal in the jet core, however differences were observed in the shear layer at lower Reynolds numbers, with the heated case exhibiting decreased lateral velocities as compared to the isothermal case.

ACKNOWLEDGEMENTS

I would like to express my appreciation to my supervisor Dr. David Novog for his guidance and support throughout my graduate studies. I would also like to thank Dr. Alex Rashkovan for all of the assistance and input to this thesis. The financial support of the CANDU Owners Group and National Science and Engineering Research Council (NSERC) is gratefully acknowledged.

Next I would like to extend my thanks to James Strack, for guiding me through my initial ignorance in the lab, and the members of my lab group – Travis, Chris, and Garik – for always being ready to assist with experiments or discuss problems that arose. I also would like to acknowledge the WEB group - Jay, Fred, Ivan, Matt, Haley, Zack, Travis, Kendall and others too numerous to name for the reliable good times every Wednesday, blowing off steam singing along with Chris Clause.

I am grateful to my family and their support during both the pursuit of this degree, and in everyday life. I would like to thank Emily-Rose Creighton for her endless patience and support as I dealt with the struggles of life during graduate school. Finally I would like to dedicate this thesis to my father, whose love of learning and years of support and encouragement let me know that I can accomplish anything I set my mind to.

TABLE OF CONTENTS

1 INTRODUCTION 1

1.1 Project Description and Scope 1

1.2 CANDU Moderator 1

1.3 Review of Existing Literature 3

1.3.1 Moderator Cooling 3

1.3.2 Free Jets 6

1.3.3 Impingement 7

1.3.4 Heat Transfer and Buoyancy 11

2 THEORETICAL BACKGROUND 12

2.1 Overview of Fluid Dynamics Basics 12

2.1.1 Laminar and Turbulent Flow 12

2.1.2 Incompressible Flow 13

2.1.3 Viscosity and Shear Stress 13

2.1.4 Buoyancy and Natural Convection 14

2.2 Conservation Equations 15

2.2.1 Continuity Equation 15

2.2.2 Navier Stokes Equation 16

2.2.3 Energy Equation 17

2.3 Dimensionless Numbers 17

2.4 Turbulence Modelling 19

2.4.1 Reynolds Averaging 20

2.4.2 Reynolds Stress and the Boussinesq Approximation 22

2.4.3 k-ε Turbulence Models 24

2.4.4 k-ω Turbulence Models 26

2.4.5 Other Models 27

3 EXPERIMENTAL DETAILS 28

3.1 Loop Design and Specifications 28

3.1.1 Instrumentation 33

3.2 Particle Image Velocimetry 34

3.2.1 PIV Overview 34

3.2.2 PIV setup 35

3.2.3 Model Selections 35

4 CFD SETUP 41

4.1 Geometry and Meshing 41

4.2 Models and Parameters 43

4.2.1 Boundary Conditions 43

4.2.2 Physics Models 45

5 RESULTS 47

5.1 Benchmark Study 47

5.2 General Profiles 49

5.3 Performance of Turbulence Models 52

5.3.1 Jet Velocity 53

5.3.2 Turbulence 58

5.4 Reynolds Number Effects 63

5.4.1 Jet Velocity 63

5.4.2 Turbulence 69

5.5 Buoyancy Effects 72

5.5.1 Jet Velocity 72

5.5.2 Turbulence 77

5.5.3 Heated CFD 79

6 CONCLUSION 82

6.1 Recommendations for Future Work 83

7 References 84

Appendix A: Experimental Setup

Appendix B: Vector Fields

LIST of FIGURES

Figure 1.1: Arrangement of fuel elements, pressure and calandria tubes (Bereznai, 2005) 2
Figure 1.2: Grids used for moderator simulations a) (Kim, Yu, & Kim, 2006) b) (Kim & Chang, 2015) 5
Figure 1.3: Schematic diagram showing flow upstream and downstream from (a) smooth contraction, (b) orifice plate, and (c) long pipe (Smith, Mi, Nathan, & Dally, 2004) 7
Figure 1.4: Flow zones in an impinging jet (Jambunathan, Lai, Moss, & Button, 1992).............. 8
Figure 1.5: Impingement on a convex surface (Re = 6000, H/d = 4) (Cornaro, Fleischer, & Goldstein, 1999)... 10
Figure 3.1: Experimental Loop 28
Figure 3.2: Heater Rod Schematic 29
Figure 3.3: Heater Axial Power Profile 30
Figure 3.4: Effect of optical distortion suppression.. 32
Figure 3.5: Sample PIV Timing Diagram... 34
Figure 3.6: Effect of PIV Time Interval Selection.. 36
Figure 3.7: Effect of Image Pre-Processing 38
Figure 3.8: Final Result of Image Processing 40
Figure 4.1: Straight Line Probe across Curved Grid.. 41
Figure 4.2: Meshed Geometry 42
Figure 4.3: Jet Inlet Velocity Profile.. 44
Figure 5.1: Comparison of Benchmark Simulation to Experimental Data 48
Figure 5.2: Comparison of CFD to Experimental Data (Singh, Premachandran, & Kohli, Experimental and numerical investigation of jet impingement cooling of a circular cylinder, 2013a) 48
Figure 5.3: Typical Jet Velocity Profiles (Experimental, Zero Power, Re = 5 000) 50
Figure 5.4: Typical Jet Velocity Profiles (CFD, Standard k-ε, Re = 5 000)................................ 51
Figure 5.5: Typical U Velocity Profiles (Experimental, Zero Power, Re = 5 000)...................... 51
Figure 5.6: Typical U Velocity Profiles (CFD, Standard k-ε, Re = 5 000) 52
Figure 5.7: Comparison of CFD and PIV Results (Re = 10 000, Realizable k-ε Model)............. 53
Figure 5.8: Comparison of Experimental and Simulation Results (y/d = 3.75, Re = 5 000)........ 54
Figure 5.9: Comparison of Experimental and Simulation Results (y/d = 3.75, Re = 10 000)...... 55
Figure 5.10: Comparison of Experimental and Simulation Results (y/d = 3.75, Re = 25 000).... 56
Figure 5.11: Velocity Profiles Perpendicular to Jet (Re = 10 000, y/d = 3.75) 58
Figure 5.12: Comparison of TKE Profiles (y/d = 2, Re = 5 000) 59
Figure 5.13: Comparison of TKE Profiles (y/d = 3.75, Re = 5 000) 60
Figure 5.14: Realizable k-ε Turbulence Kinetic Energy Profile (Re = 5 000) 61
Figure 5.15: Experimental Turbulence Kinetic Energy Profile (Re = 5 000).............................. 61
Figure 5.16: Experimental Turbulence Kinetic Energy Profile (Re = 25 000)............................ 62
Figure 5.17: Impact of Reynolds Number on V Velocities 64
Figure 5.18: Impact of Reynolds Number on Jet Half-Width 66

Figure 5.19: Impact of Reynolds Number on U Velocities (Realizable *k-ε,* y/d = 3.75).............. 68
Figure 5.20: Impact of Reynolds Number on U velocities (Experimental Data, y/d = 3.75)....... 68
Figure 5.21: Normalized Turbulence Kinetic Energy – Standard k-ε (y/d = 2) 69
Figure 5.22: Normalized Turbulence Kinetic Energy – Realizable k-ε (y/d = 2)......................... 70
Figure 5.23: Normalized Turbulence Kinetic Energy – Standard k-ω (y/d = 2) 70
Figure 5.24: Normalized Turbulence Kinetic Energy – Experimental (y/d = 2).......................... 71
Figure 5.25: Jet Velocity Decay across Jet (Re = 5000, y/d = 3.75) 73
Figure 5.26: Comparison of Heated and Unheated V Velocity Profiles (Re = 5 000) 74
Figure 5.27: Jet Half-Width Profiles (Re = 5000, y/d = 3.75).. 75
Figure 5.28: Effect of Heating on U Velocities (Re = 5000, y/d = 3.75) 76
Figure 5.29: Effect of Heating on U Velocities (Re = 10 000, y/d = 3.75) 77
Figure 5.30: Turbulence Profile for Heated Test (Re = 5 000, 500 W).. 78
Figure 5.31: Turbulence Profile for Unheated Test (Re = 5 000, Zero Power)............................ 78
Figure 5.32: Comparison of Heated and Unheated Jet Half-Width.. 79
Figure 5.33: Heating Comparison of Average Normalized TKE Profile (Realizable k-e, y/d = 3.75) 80

LIST of TABLES

Table 3-1: Equipment Uncertainties 34

Table 4-1: Inlet Boundary Turbulence Specifications 45

NOTATION AND ABBREVIATIONS

CANDU	Canada Deuterium Uranium
CFD	Computational Fluid Dynamics
CHF	Critical Heat Flux
ECC	Emergency Core Cooling
FFT	Fast Fourier Transform
LDV	Laser Doppler Velocimetry
LOCA	Loss of Coolant Accident
MODTURC-CLAS	MODerator TURbulent Circulation Co-Located Advanced Solution
PIV	Particle Image Velocimetry
RANS	Reynolds Averaged Navier-Stokes
RMS	Root Mean Squared
RTD	Resistance Temperature Detector
TKE	Turbulence Kinetic Energy
α_t	Turbulent Thermal Diffusivity
ρ	Density
τ	Shear Stress
τ^R	Reynolds Shear Stress
μ	Dynamic Viscosity
f_b	Body Force Term
h	Heat Transfer Coefficient
I	Turbulence Intensity
β	Thermal Expansion Coefficient
c_p	Specific Heat Capacity (at constant pressure)
k_t	Thermal Conductivity
k	Turbulence Kinetic Energy
ε	Turbulence Dissipation Rate
p	Pressure
q''	Heat Flux
ω	Specific Turbulence Dissipation Rate/Turbulence Frequency
U	Velocities Along the x-Axis (Perpendicular to the Jet Axis)
V	Velocities Along the y-Axis (Parallel to the Jet Axis)

DECLARATION of ACADEMIC ACHIEVEMENT

I declare that all of the work described in the following thesis was performed by the author under the guidance of Dr. David Novog and with occasional assistance and support from James Strack, Garik Patterson, Travis Sheasgreen, and Christopher Hollingshead. The only material work presented in this thesis not performed by the author are the meshes for the CFD simulations and the heated CFD simulations, which were created and run by Dr. Alex Rashkovan, and the labVIEW program used to collect temperature and flow measurements, which was created by Brian McCrindle under the supervision of the author.

1 INTRODUCTION

1.1 Project Description and Scope

In this research project, the behaviour of a fluid emerging from an axisymmetric jet and impinging onto a cylinder under various degrees of opposing buoyancy forces is investigated.

This research project emerged from the desire to perform a separate effect test to supplement integral tests that are currently being performed investigating the flow patterns of the moderator in CANDU reactors. The larger tests are studying the flow patterns around and within an array of cylinders, both heated and unheated, designed to represent Calandria tubes in CANDU reactors. Due to the number and complexity of the components and features affecting the flows in these larger tests, it was deemed useful to investigate the flows around a single heated cylinder to better understand the local fluid behaviour.

The decision to use a jet as the source of the flow was made due to the simplicity of the geometry as well as the clearly defined boundary conditions for the fully developed flow at the jet exit. This thesis seeks to build on the existing body of research on jet impingement in order to gain further clarity on the flow behaviour in particular scenarios of interest.

1.2 CANDU Moderator

In Canada Deuterium Uranium (CANDU) reactors, the core is situated inside a horizontal cylindrical tank known as the calandria. The calandria is filled with heavy water (D_2O) which serves as a moderator – absorbing energy from the “fast” high-energy neutrons released by fission occurring in the fuel, and converting them to thermal neutrons which have a higher probability of causing fissions when interacting with fissile nuclei in the fuel.

Inside the calandria is an array of cylindrical channels known as calandria tubes, ranging in number from 380-480 depending on the particular reactor design. Within the calandria tubes are situated the pressure tubes, which house the Uranium Oxide fuel bundles. The annular space between these two tubes is filled with a carbon dioxide gas which provides thermal insulation and is a suitable place from which to monitor for cracks or leaks in the pressure tube. Figure 1.1 provides an illustration of the arrangement of fuel and supporting tubes.

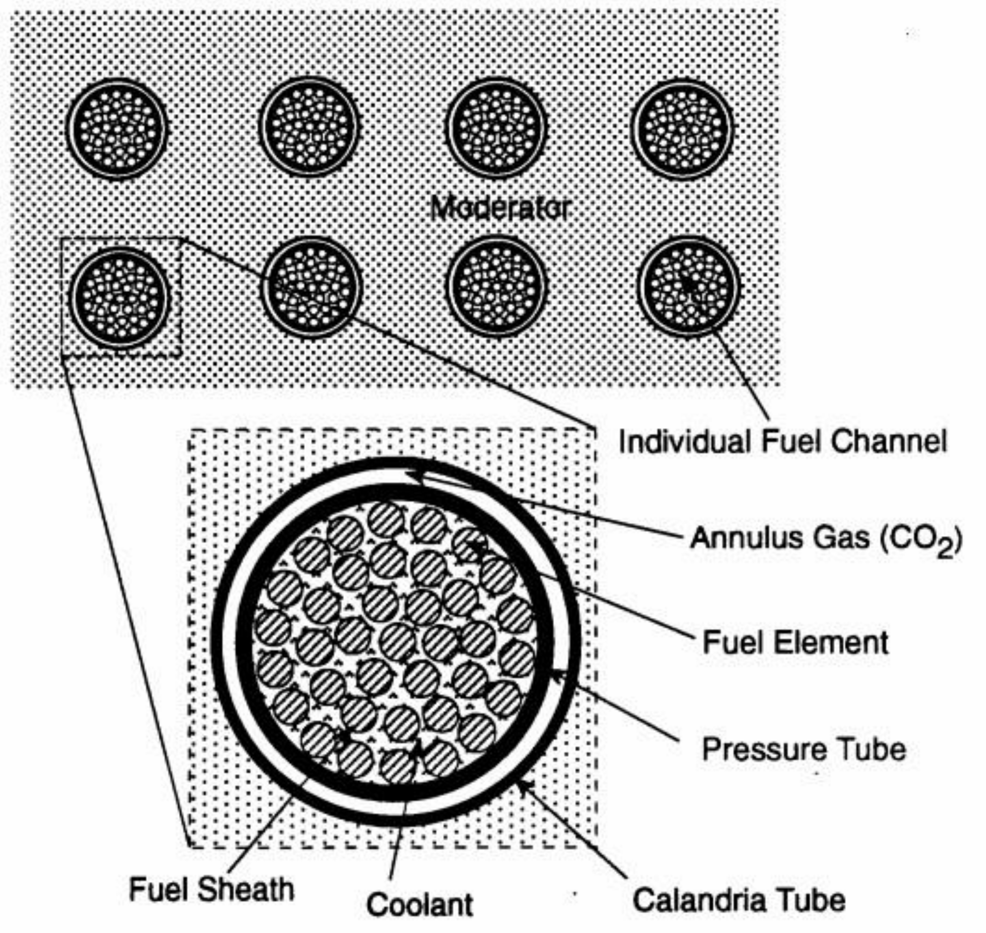

Figure 1.1: Arrangement of fuel elements, pressure and calandria tubes (Bereznai, 2005)

As the annulus does not provide perfect thermal insulation, a secondary feature of the moderator is to provide a heat sink for excess heat; approximately 5% of the heat generated by the reactor is deposited in the moderator. The vast majority (70-80%) of this heat is produced during the scattering process from neutron thermalization and from the absorption of released gamma rays. A further 15%-25% of the heat is deposited by gamma rays created from the decay of fission products, leaving only about 3-5% coming from conventional heat sources such as thermal radiation, convection, and conduction across the annulus (Bereznai, 2005).

The prediction of the flows and temperatures in the moderator system can be important in the safety evaluation during some hypothetical transients (e.g. LOCA with loss of ECC). An experimental program to collect data for CFD validation, including integrated moderator circulation tests as well as the separate effect tests discussed in this thesis, has been funded by the CANDU Owners Group.

1.3 Review of Existing Literature

1.3.1 Moderator Cooling

Due to the role of the moderator as a heat sink, the moderator temperature and circulation patterns are a topic of great interest for many safety analysts and researchers. CANDU moderator safety analysis calculations in the industry are most commonly performed using the Computational Fluid Dynamics (CFD) code MODTURC (MODerator TURbulent Circulation) or its adaptation MODTURC-CLAS (MODerator TURbulent Circulation Co-Located Advanced Solution) codes. These codes treat the array of fuel channels as a porous medium with experimentally calibrated hydraulic resistances (Teyssedou, Necciari, Reggio, Zadeh, & Étienne, 2014) and use CFD simulations for the other regions within the calandria.

As this porous media approach cannot capture local details of the flow around the calandria tubes, efforts have recently been put into modelling all geometries present in the moderator. While many of the reports on CFD simulation of moderator behaviour are internal reports and presentations, of the publicly available papers, Kim et al. (Kim, Yu, & Kim, 2006) and Kim et al. (Kim & Chang, 2015) are some of the studies that investigated the moderator flow and temperature fields with all calandria geometrical details modelled without incorporating the porous media approximation. Although these provide more local flow characteristics, a full understanding of the fine detail is still limited by computational restrictions. The former study tackled the computational difficulties by using a fairly coarse unstructured grid, where the circumference of each tube was split into eight mesh cells with six cells between each channel, while the latter used a finer mesh around and between channels but only modelled a limited depth (0.02m or 1/10 of the actual calandria depth); see Figure 1.2 for a sample of the grids used for each study.

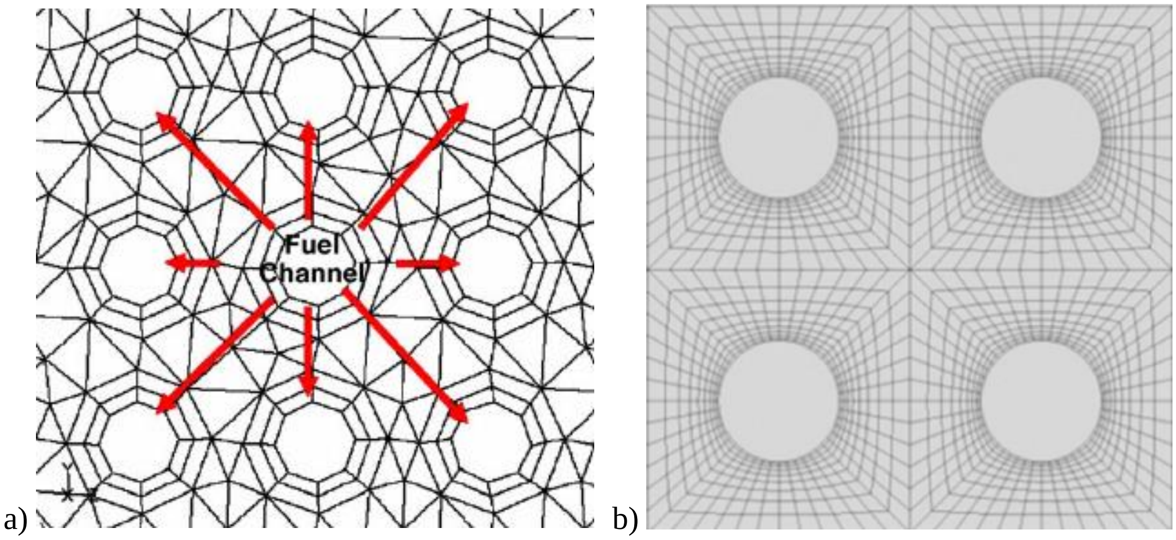

Figure 1.2: Grids used for moderator simulations a) (Kim, Yu, & Kim, 2006)
b) (Kim & Chang, 2015)

While significant research has been conducted into moderator circulation and flow patterns, most of these studies model flow throughout the entire calandria, or through an array of channels. A reasonable representation of these studies is present in the previously mentioned Kim and Teyssedou papers and in a paper by Yoon et al. which used more modern CFD codes to assess MODTURC-CLAS predictions; some discrepancies were found in the predictions, however most of the differences identified led to more conservative predictions on the part of MODTURC-CLAS, and as such no concerns were raised (Yoon, Rhee, & Min, 2004). In addition, studies which focus on a single channel tend to concern themselves more with the heat transfer or critical heat flux (CHF) conditions than surrounding flow patterns (Gillespie, 1981) (Tanase, Szymanski, El-Hawary, & Delja, 2015). It is of interest for this research to focus primarily on local flow patterns around a single heated calandria tube.

1.3.2 Free Jets

Free jet flows have been studied extensively, particularly as a test case for turbulence modelling as the geometries are simple, while the behaviour of the flow is rather complex. Free jets provide a good benchmark case for modelling free shear flows. An extensive review of the flow field in turbulent round free jets has been compiled, providing a thorough overview of the research completed on round free jets (Ball, Fellouah, & Pollard, 2012). It is notable that of the many papers cited in the review, very few used a fully developed turbulent profile, opting instead for a smooth contraction nozzle which results in a top-hat velocity distribution. An additional study conducted a Large Eddy Simulation (LES) of a steady circular air jet issuing into quiescent air from a pipe inlet in order to characterize the vortical structures and jet dissipation (Jewkes, King, & Chung, 2011).

Other studies have investigated the impact of the nozzle shape – circular, square, or rectangular (Singh, Premachandran, & Kohli, 2015) – and the design of the jet inlet – comparing smooth contraction, orifice, or long pipe inlets (Mi, Nathan, & Nobes, 2001) (Xu & Antonia, 2002) – on the velocity and turbulence profiles both at the inlet and downstream. Further work has been done on how well these differences are predicted by common turbulence models (Smith, Mi, Nathan, & Dally, 2004). Figure 1.3 shows the typical velocity and turbulence profiles for these different nozzle types.

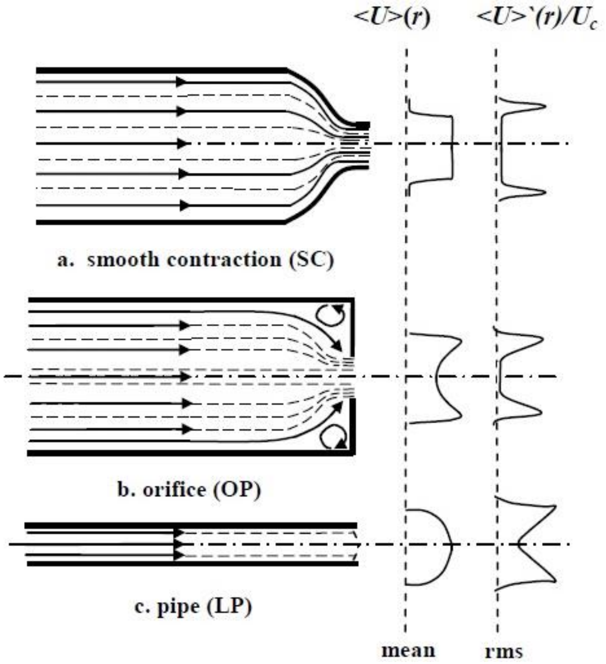

Figure 1.3: Schematic diagram showing flow upstream and downstream from (a) smooth contraction, (b) orifice plate, and (c) long pipe (Smith, Mi, Nathan, & Dally, 2004)

One other notable paper regarding turbulence modelling for free jets was published by Pope. He developed an adjusted value for one of the key empirical coefficients in the k-ε turbulence model and included a term to capture the effects of vortex stretching, which in combination significantly improved predictions for spreading and dissipation of round jets (Pope, 1978). While this model improves predictions of turbulence kinetic energy for both free and impinging jets, the predicted TKE values in the impingement zone are still far from measured values.

1.3.3 Impingement

Impinging jet flows have been studied in great detail for certain geometries such as plates, and less so for others. A review of studies on heat transfer due to a single circular jet impinging a heated plate, which considered 27 studies performed between 1962 and 1991, provides an overview of the existing literature on the topic (Jambunathan, Lai, Moss, & Button, 1992). A round jet impinging onto a flat plate is commonly divided into four zones – see Figure 1.4:

1) The initial mixing region where surrounding fluid is entrained into the jet flow, reducing the jet velocity. The centreline velocity is approximately equal to the jet exit velocity as the shear layers have not expanded to the centre of the jet.
2) The established region may be present if the object onto which the jet is impinging is sufficiently far from the jet exit. In this scenario the turbulent layers will interact and the centreline velocities will decline proportionally to the distance from the jet exit.
3) The impingement area or deflection zone of the jet is where the jet velocity begins to rapidly decrease as the pressure builds at the area of impingement. This deflection zone is thought to extent approximately 1.2 – 2 jet diameters above the impingement surface.
4) The wall jet expands radially, accelerating away from the jet impingement region, then slowing due to the shear between both the jet and the wall, as well as the jet and surrounding fluid. While the previous three zones are similar for impingement onto a cylinder, this final zone exhibits notably different behaviour due to the surface curvature.

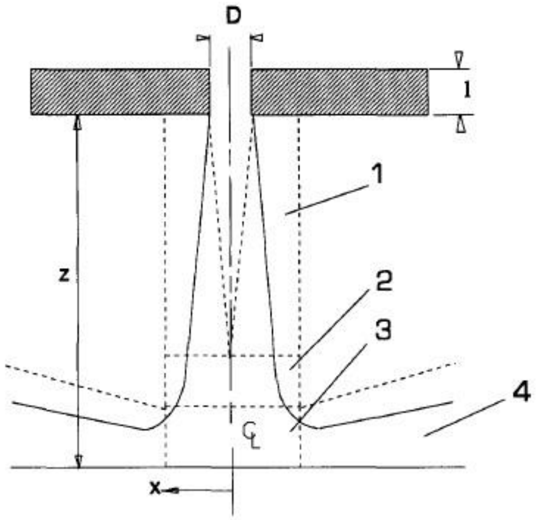

Figure 1.4: Flow zones in an impinging jet (Jambunathan, Lai, Moss, & Button, 1992)

While circular jet impingement onto heated cylinders studies are limited, there exists a more substantial body of literature on slot jets. Various researchers have investigated heat transfer and flow patterns of slot jets (Olsson, Ahrne, & Trägårdh, 2004) (Dirita, De Bonis, & Ruocco, 2007). One study covered slot jets with Reynolds numbers ranging from 4000-22000 at jet heights of 6-20 times the jet diameter (Gori & Bossi, 2003). Another research team used PIV to examine impinging flows from a slot jet and validate their numerical investigation (Singh & Singh, 2008). Fewer studies examine round jets impinging onto cylinders, and even fewer of those focus on the flow patterns, opting instead to study only the heat transfer.

A thorough investigation providing a summary of research conducted on the velocity fields and heat transfer as circular jets impinge a heated plate and how various turbulence models perform to simulate such a scenario has also been conducted (Cooper, Jackson, Launder, & Liao, 1993).

One of the most relevant studies to this research was conducted by Ezirgemez at al., who quantified the velocity fields in the impingements zone of a jet impinging an unheated cylinder (Esirgemez, Newby, Nott, Ölçmen, & Ötügen, 2007). Similar work had previously been performed, however the emphasis was on visualization of the flow and no velocity fields were quantified (Cornaro, Fleischer, & Goldstein, 1999). While their work uses different parameters and working fluid than the experiments in this thesis, the phenomena are similar; see Figure 1.5. Another paper describes an investigation conducted to observe heat transfer from a jet impinging a heated cylinder but limited discussion of flow patterns or velocity fields was included (Tawfek, 1999).

Figure 1.5: Impingement on a convex surface (Re = 6000, H/d = 4) (Cornaro, Fleischer, & Goldstein, 1999)

Literature also exists regarding a study of air impinging on a heated cylinder with d/D of 0.11-0.25 at heights of 4-6 jet diameters above the cylinder, and Reynolds numbers of 10 000-25 000 and comparing the velocities and heat transfer data to those predicted with various turbulence models (Singh, Premachandran, & Kohli, 2013a) (Singh, Premachandran, & Kohli, 2013b). The velocity profiles were not quantified in detail but significant discrepancies were found between the experimental and numerical results; Nusselt number errors at the stagnation point varied from 23% to 740% depending on the turbulence model and parameters used.

This thesis seeks to expand on the research of round jet impingement onto a heated cylinder, focusing on water as the fluid of interest; this is important because, as noted by Ball in the aforementioned review, the differences in fluid properties such as density and viscosity may significantly alter the near field phenomena.

1.3.4 Heat Transfer and Buoyancy

There is a great deal of research on natural and mixed convection heat transfer and flows around heated cylinders. Often this research focuses on laminar flows and situations in which the entire fluid is in motion – rather than a single turbulent jet momentum source such as the impact of a round jet onto a cylinder.

Studies such as those performed by Badr (Badr, 1984), Gandikota (Gandikota, Amiroudine, Chatterjee, & Biswas, 2010), Sparrow (Sparrow & Lee, 1976), and Fand (Fand & Keswani, 1973) provide a sample of the work that has been conducted. Fand observes mixed convection heat transfer for a Richardson number (a dimensionless number indicative of the relative impact of forced and natural convection) between 0.5 and 40, ranging from primarily forced convection to primarily natural convection. Badr and Gandikota both examined scenarios of aiding (parallel) flow, where the forced flow follows the same direction as the buoyant force, and opposing (contra) flow, in which the forced flow acts against the buoyant force.

2 THEORETICAL BACKGROUND

This section provides an overview of the underlying principles and governing equations that describe the behaviour of fluids. The primary focus is on turbulence and the various approaches to modelling turbulent flows utilized in CFD simulations.

Throughout the section and the remainder of the thesis, the velocity and dimension vectors are defined as:

$$\boldsymbol{u} = [\boldsymbol{u}, \boldsymbol{v}, \boldsymbol{w}]^{\boldsymbol{T}} \tag{2.1}$$

$$\boldsymbol{x} = [\boldsymbol{x}, \boldsymbol{y}, \boldsymbol{z}]^{\boldsymbol{T}} \tag{2.2}$$

2.1 Overview of Fluid Dynamics Basics

2.1.1 Laminar and Turbulent Flow

Laminar flow is described as steady, well-structured flow where momentum transfer is controlled by viscous diffusion. Fluid properties such as velocity and pressure are fairly constant throughout the flow and do not exhibit random, time-dependent fluctuations.

Turbulent flows, in contrast, occur when the internal viscous forces are overcome by the inertia of the fluid, leading to unsteady fluctuations in velocity and pressure. The most concise description of turbulent flow may be Lewis Richardson's adaptation of "The Siphonaptera":

Big whorls have little whorls,
which feed on their velocity;
And little whorls have lesser whorls,
And so on to viscosity.

This captures the key ideas that turbulent flow consists of eddies on a wide range of time and length scales. The kinetic energy of these eddies cascades down to smaller and smaller eddies until eventually the energy is dissipated as heat through viscous action.

2.1.2 Incompressible Flow

Incompressible flows are those in which changes in pressure do not lead to changes in density. This allows for the simplification of some of the equations used in the modelling and calculations of flow parameters. For the purposes of this project, water as the fluid of interest is considered incompressible. The only density differences considered are those that arise due to temperature differences.

Mathematically this is expressed by setting the substantial derivative to zero:

$$\frac{D\boldsymbol{\rho}}{D\boldsymbol{t}} = \frac{\partial \boldsymbol{\rho}}{\partial \boldsymbol{t}} + \nabla \boldsymbol{\rho} \cdot \boldsymbol{u} = \mathbf{0} \tag{2.3}$$

2.1.3 Viscosity and Shear Stress

Viscosity is a key factor in fluid behaviour. It is defined as the ability of a fluid to resist flow or deformation, acting as the constant of proportionality between the shear stress (F/A = τ) and the rate of deformation.

$$\boldsymbol{\tau} = \frac{\boldsymbol{F}}{\boldsymbol{A}} = \boldsymbol{\mu} \frac{\partial \boldsymbol{u}}{\partial \boldsymbol{x}} \tag{2.4}$$

where μ is the fluid viscosity.

Newtonian fluids such as water are defined as those in which the above relationship is linear, i.e. the strain rate is linearly proportional to the shear stress. A corollary of this definition is that viscosity, as the constant of proportionality, is constant for a given temperature and pressure, however μ still may vary with changes in these thermodynamic properties. Typically the change in viscosity with changes in pressure is negligible; however temperature can have large effects. In addition, fluids may either be ideal ($\mu = 0$) or Non-Newtonian, where the relationship between shear stress and strain rate is non-linear, therefore μ is variable and can itself depend on the strain rate.

2.1.4 Buoyancy and Natural Convection

Natural convection describes the movement of fluid due to buoyant forces. As the temperature of a fluid near a heated surface rises, the density decreases, causing the fluid to rise. Newton's law of cooling describes the change in temperature for a specified heat flux q'':

$$\boldsymbol{q'' = h(\Delta T)} \tag{2.5}$$

where h is the convective heat transfer coefficient.

This temperature difference causes a density change according to the thermal expansion coefficient of the fluid at an assumed constant pressure:

$$\boldsymbol{\beta = -\frac{1}{\rho}\frac{\partial\rho}{\partial T} \quad \rightarrow \quad \Delta\rho \approx -\rho\beta\Delta T} \tag{2.6}$$

Leading to a buoyancy force given by:

$$\boldsymbol{F = g\,\Delta\rho V = -\,g\rho\beta\Delta T\,V} \tag{2.7}$$

2.2 Conservation Equations

Conservation equations are the fundamental equations that describe fluid behaviour. These equations are derived from the principles of conservation of mass, momentum, and energy; any change in the value of one of these parameters for a given control volume must be equal to the surface flux across the control volume plus any source or sink within the volume.

The general conservation equation for a conserved quantity Φ is written as follows.

$$\frac{\partial(\boldsymbol{\rho\Phi})}{\partial \boldsymbol{t}} + \nabla \cdot (\boldsymbol{\rho u \Phi}) = \nabla \cdot (\boldsymbol{\Gamma}^{\boldsymbol{\Phi}} \nabla \boldsymbol{\Phi}) + \boldsymbol{Q}^{\boldsymbol{\Phi}} \tag{2.8}$$

where the first term on the left side represents the unsteady or accumulation term, the second term on the left represents the convection of the parameter, the first term on the right side is the diffusion term with Γ acting as the diffusion coefficient, and the final term represents a source or sink within the control volume.

This section describes the application of this conservation equation to the key fluid properties of mass, momentum, and energy.

2.2.1 Continuity Equation

The continuity equation describes the conservation of mass within the control volume. The change in mass for a given control volume must equal the mass that enters the volume less the mass that leaves, plus any changes in density:

$$\frac{\partial \boldsymbol{\rho}}{\partial \boldsymbol{t}} + \boldsymbol{\nabla} \cdot (\boldsymbol{\rho u}) = \mathbf{0} \qquad \textbf{(2.9)}$$

For incompressible flows, the density terms are eliminated by applying equation (2.3) and noting that $\nabla \cdot (\rho \boldsymbol{u}) = \boldsymbol{u} \cdot \nabla \rho + \rho \nabla \cdot \boldsymbol{u}$, leaving the incompressible continuity equation:

$$\boldsymbol{\nabla} \cdot \boldsymbol{u} = \mathbf{0} \qquad \textbf{(2.10)}$$

2.2.2 Navier Stokes Equation

The Navier-Stokes equations describe the conservation of linear momentum in the system. According to this principle, the change in momentum (i.e. acceleration) for a control volume is proportional to the sum of forces acting on the volume. This force term is typically split into surface forces, which are comprised of pressure and viscous stresses, and the body forces, namely gravity; however there are other possible body forces such as Coriolis forces that can be present, so in order to preserve generality, the body force term is left as f_b.

$$\frac{\partial (\boldsymbol{\rho u})}{\partial \boldsymbol{t}} + \boldsymbol{\nabla} \cdot (\boldsymbol{\rho u u}) = -\boldsymbol{\nabla p} + \boldsymbol{\nabla} \cdot \boldsymbol{\tau} + \boldsymbol{f_b} \qquad \textbf{(2.11)}$$

In this equation $\boldsymbol{\tau}$ is the incompressible viscous stress tensor defined as:

$$\boldsymbol{\tau} = \boldsymbol{\mu}[\boldsymbol{\nabla u} + (\boldsymbol{\nabla u})^{\boldsymbol{T}}] \qquad \textbf{(2.12)}$$

where μ is molecular viscosity. These equations are often combined and simplified to give a more recognizable form of the N-S equation, however it will be seen later that the form of equation (2.11) is useful to illustrate differences in the statistical approaches.

2.2.3 Energy Equation

Just as with the continuity and Navier-Stokes equations, the energy equation is based on the principle of conservation. This equation may be written in a variety of ways, for example, in terms of internal energy, specific enthalpy, etc. For the purposes of this thesis the energy equation will be considered in terms of temperature:

$$\frac{\partial\left(\rho c_p T\right)}{\partial t} + \nabla \cdot \left(\rho c_p \boldsymbol{u} T\right) = \nabla \cdot (k_t \nabla T) + Q^T \tag{2.13}$$

where c_p is the specific heat capacity at constant pressure, k_t is the thermal conductivity of the fluid, and Q^T is a source or sink within the control volume.

2.3 Dimensionless Numbers

There are several dimensionless numbers that are used in the field of fluid dynamics to describe certain characteristics of flows, or to allow for the comparison of flows of different scales or geometries.

The Reynolds number is one of the most important dimensionless numbers. It represents the ratio of inertial to viscous forces. This can be interpreted as the relative importance of advection as compared to diffusion for the momentum in the flow.

$$Re = \frac{\rho U L}{\mu} \tag{2.14}$$

where ρ represents density, U is the average velocity, L is the characteristic length, often the diameter in pipe flow, and μ is the dynamic or shear viscosity. The Reynolds number provides a good indication of when the transition from laminar to turbulent flow occurs; for internal flows, a Reynolds number below 2 300 generally corresponds to laminar flow, while above Re ≈ 4 000 flow is turbulent, flows with Reynolds numbers between these thresholds are transitional and cannot be described as either fully laminar or fully turbulent.

The Prandlt number represents the ratio of momentum to thermal diffusivity. I.e. it represents the relative thickness of the viscous or hydrodynamic boundary layer as compared to the thermal boundary layer:

$$Pr = \frac{\mu}{\rho} / \frac{k_t}{c_p \rho} = \frac{\mu c_p}{k_t} \tag{2.15}$$

where μ is the dynamic or shear viscosity, c_p is the specific heat capacity of the fluid at constant pressure, and k_t is the thermal conductivity. For turbulent flow, a similar definition is applied however the momentum eddy diffusivity and thermal eddy diffusivity are used. These represent the diffusion of momentum and heat due to turbulent eddies rather than the viscous and conductive dissipation that dominate in laminar flow. The turbulent Prandlt number cannot be computed directly for reasons that are discussed later, and as such must rely on empirical correlations or assumptions about the relation between turbulent and viscous stresses.

The Grashof number represents the ratio of buoyant to viscous forces. As such it can be thought of as the analogue in natural convection for the Reynolds number in forced convection:

$$Gr = \frac{g\beta\Delta T L^3}{\nu^2} \tag{2.16}$$

where g represents gravity and ΔT is the temperature difference between the surface and bulk temperatures, and ν represents the kinematic viscosity.

Finally the Richardson number allows a comparison of the forced and natural convection:

$$Ri = \frac{g\beta\Delta T L^3}{U^2} = \frac{Gr}{Re^2} \tag{2.17}$$

Typically if a Richardson number is less than 0.1, the natural convection is deemed negligible, and for Richardson numbers greater than 10, forced convection is considered negligible.

2.4 Turbulence Modelling

Turbulent flows are described as "chaotic, diffusive causing rapid mixing, time-dependant, and involve three-dimensional vorticity fluctuation with a broad range of time and length scales." Due to this wide variety of time and length scales, a direct numerical simulation (DNS) of turbulent flows requires a very fine mesh and very small time step, in order to properly resolve all of the properties of the flow, rendering this approach impractical for most applications.

In order to improve simulation time, statistical analyses are used to model flow behaviour. The most common approach is Reynolds averaging.

2.4.1 Reynolds Averaging

The process of Reynolds averaging involves decomposing each flow variable (e.g. pressure, velocity, temperature, etc.) into a mean component and a fluctuating component, such that for a given flow variable $\Phi(\boldsymbol{x}, t)$:

$$\Phi(\boldsymbol{x}, t) = \overline{\Phi(\boldsymbol{x}, t)} + \Phi'(\boldsymbol{x}, t) \tag{2.18}$$

The average component can be determined in a variety of ways, depending on the nature of the flow. The most common averaging technique is time averaging, where $\overline{\Phi}$ is calculated as follows:

$$\overline{\Phi(\boldsymbol{x})} = \lim_{T \to \infty} \frac{1}{T} \int_{t}^{t+T} \Phi(\boldsymbol{x}, t) dt \tag{2.19}$$

Time averaging is most appropriate for stationary or steady flows where the flows do not change, or change very slowly, with time. For the sake of practicality, finite time scales must be used for the averaging, which is acceptable providing that the T chosen is relatively long compared to the period of the fluctuations.

Other common techniques include spatial averaging, which is suitable for homogeneous flows, and ensemble averaging, which is a general technique that involves computing the average over many identical experiments. The remainder of the discussion on turbulence modelling will use the time average defined above, however the application can be similarly used for all averaging techniques.

To obtain the Reynolds Averaged Navier-Stokes (RANS) equations, the time average decomposition is applied to velocity and pressure. These decomposed variables are then substituted into equations (2.10) - (2.13) and a time average is taken to result in the following equations:

$$\overline{\nabla \cdot (\overline{\boldsymbol{u}} + \boldsymbol{u}') = 0} \tag{2.20}$$

$$\overline{\frac{\partial[\rho(\overline{\boldsymbol{u}} + \boldsymbol{u}')]}{\partial t} + \nabla \cdot [\rho(\overline{\boldsymbol{u}} + \boldsymbol{u}')(\overline{\boldsymbol{u}} + \boldsymbol{u}')] = -\nabla(\overline{p} + p') + \nabla \cdot \mu \left[\nabla(\overline{\boldsymbol{u}} + \boldsymbol{u}') + \left(\nabla(\overline{\boldsymbol{u}} + \boldsymbol{u}')\right)^{T}\right] + f_b} \tag{2.21}$$

$$\frac{\left[\boldsymbol{\rho c_p}\left(\overline{\boldsymbol{T}} + \boldsymbol{T}'\right)\right]}{\boldsymbol{\partial t}} + \boldsymbol{\nabla} \cdot \left[\boldsymbol{\rho c_p}(\overline{\boldsymbol{u}} + \boldsymbol{u}')\left(\overline{\boldsymbol{T}} + \boldsymbol{T}'\right)\right] = \boldsymbol{\nabla} \cdot \left[\boldsymbol{k}\,\boldsymbol{\nabla}\left(\overline{\boldsymbol{T}} + \boldsymbol{T}'\right)\right] + \boldsymbol{Q^T} \tag{2.22}$$

Noting that, by definition, the average of the fluctuating component for any variable must be zero, as well as the fact that the average of an average is itself, these equations simplify to:

$$\nabla \cdot \overline{\boldsymbol{u}} = 0 \tag{2.23}$$

$$\frac{\partial[\rho\overline{\boldsymbol{u}}]}{\partial t} + \nabla \cdot [\rho\overline{\boldsymbol{u}\boldsymbol{u}}] = -\nabla\overline{p} + \nabla \cdot \left[\overline{\boldsymbol{\tau}} - \rho\overline{\boldsymbol{u}'\boldsymbol{u}'}\right] + f_b \tag{2.24}$$

$$\frac{\partial\left(\rho c_p\overline{T}\right)}{\partial t} + \nabla \cdot \left(\rho c_p\overline{\boldsymbol{u}T}\right) = \nabla \cdot \left[k_t\nabla\overline{T} - \rho c_p\overline{\boldsymbol{u}'T'}\right] + \overline{Q^T} \tag{2.25}$$

These equations are the RANS equations and form the basis of many of the most common approaches used for modelling turbulent flows. Note that these equations are nearly identical to the general continuity, Navier-Stokes, and energy conservation equations (2.10), (2.11), and (2.13), except that the variables are now the time-averaged quantities.

The other key difference in the RANS equation is apparent in the diffusion terms. In addition to the averaged viscous stresses in the momentum equation ($\overline{\boldsymbol{\tau}}$) there is a term which captures the momentum diffusion due to turbulence ($-\rho\overline{\boldsymbol{u'u'}}$). This term is the primary focus of RANS turbulence modelling, wherein additional equations discussed later are included in the mathematical system in order to resolve this term. A similar term appears in the energy equation representing the heat flux due to turbulence.

The following sections describe the issues that arise when attempting to solve these equations and common approaches to resolving those issues.

2.4.2 Reynolds Stress and the Boussinesq Approximation

The critical problem for RANS turbulence modelling arises from the turbulent stress term in the momentum equation. Whereas the general Navier-Stokes equations form a closed system with four equations and four unknowns (three velocity components and pressure), the turbulent shear stress tensor that emerges in the Reynolds averaged equations introduces six additional unknowns into the equation system of equations. This term is known as the Reynolds stress tensor, given by:

$$\boldsymbol{\tau}^R = -\rho\overline{\boldsymbol{u'u'}} = \begin{matrix} \overline{u'u'} & \overline{u'v'} & \overline{u'w'} \\ \overline{v'u'} & \overline{v'v'} & \overline{v'w'} \\ \overline{w'u'} & \overline{w'v'} & \overline{w'w'} \end{matrix} \qquad \textbf{(2.26)}$$

Attempts to derive additional equations for the Reynolds stress tensor lead to the emergence of higher order terms with even more unknowns. The so called 'closure problem' now becomes clear, there are more unknown values than equations, and no mathematical way to close the system.

The most common approach to dealing with the Reynolds stress term is known as the Boussinesq Approximation. This is an assumption that the Reynolds stress tensor is proportional to the mean strain rate tensor (i.e. the mean velocity gradients), with the turbulent eddy viscosity (μ_t) defined as the constant of proportionality.

$$\boldsymbol{\tau}^R = -\rho\overline{\boldsymbol{u}'\boldsymbol{u}'} = \mu_t[\nabla\boldsymbol{u} + (\nabla\boldsymbol{u})^T] - \frac{2}{3\rho k}I \tag{2.27}$$

where k is the turbulence kinetic energy:

$$k = \frac{1}{2}\overline{\boldsymbol{u}'\boldsymbol{u}'} = \frac{1}{2}\left(\overline{u'^2} + \overline{v'^2} + \overline{w'^2}\right) \tag{2.28}$$

This is an analogy with the molecular diffusion term. Here μ_t is known as the eddy viscosity, which acts as the molecular viscosity would in the viscous stress tensor.

A similar analogy is used to relate the turbulent heat fluxes to Fourier's law:

$$\boldsymbol{q}^R = -\rho c_p\overline{\boldsymbol{u}'T'} = \alpha_t\nabla T \tag{2.29}$$

where α_t is the turbulent thermal diffusivity, analogous to the thermal conductivity in Fourier's law.

Although the Boussinesq approximation works well for a wide variety of engineering flows, it does possess some deficiencies. Chief among these is the fact that it is an approximation - there is little physical justification for why this should hold true. In addition, whereas molecular viscosity is a property of the fluid, the eddy viscosity is solely a function of the movement of the flow, therefore treating it as an isotropic scalar quantity (as the Boussinesq approximation does) is unlikely to be valid for all cases. Weaknesses of the Boussinesq approximation can be seen in flows which experience sudden changes in mean strain rate or flow over curved surfaces, both of which are present in this research (Pope, A more general effective-viscosity hypothesis, 1975) (Wilcox, 1998).

The primary differences in the following turbulence models are in how they calculate the eddy viscosity and turbulent kinetic energy used in the Boussinesq approximation.

2.4.3 *k*-*ε* Turbulence Models

The *k*-*ε* turbulence model and its many variations are some of the most commonly used closure relationships. The standard *k*-*ε* model defines the eddy viscosity and turbulent thermal diffusivity as follows:

$$\mu_t = \rho C_\mu \frac{k^2}{\epsilon} \tag{2.30}$$

$$\alpha_t = \frac{c_p \mu_t}{Pr_t} \tag{2.31}$$

As the name suggests, these equations leave *k* and *ε* as the unknown variables (C_μ is an experimentally derived constant, typically set to 0.09). Where *k* is the turbulent kinetic energy described in equation (2.28) and *ε* is the specific rate of dissipation of turbulent kinetic energy due to viscous forces, defined as:

$$\epsilon = \frac{1}{2}\frac{\mu}{\rho}\left[\nabla \boldsymbol{u}' + (\nabla \boldsymbol{u}')^T\right]:\left[\nabla \boldsymbol{u}' + (\nabla \boldsymbol{u}')^T\right] \tag{2.32}$$

The *k* and *ε* values are then calculated using the following equations, which are derived by taking respectively the trace and a particular moment of the Navier-Stokes equations then simplifying:

$$\frac{\partial(\rho k)}{\partial t} + \nabla \cdot (\rho \boldsymbol{u} k) = \nabla \cdot \left[\left(\mu + \frac{\mu_t}{\sigma_k}\right)\nabla k\right] + \tau^R : \nabla \boldsymbol{u} - \rho \epsilon \qquad \textbf{(2.33)}$$

$$\boldsymbol{\frac{\partial(\rho \epsilon)}{\partial t} + \nabla \cdot (\rho u \epsilon) = \nabla \cdot \left[\left(\mu + \frac{\mu_t}{\sigma_\epsilon}\right)\nabla \epsilon\right] + C_{\epsilon 1}\,\frac{\epsilon}{k}(\tau^R : \nabla u) - C_{\epsilon 2}\,\rho\frac{\epsilon^2}{k}} \qquad \textbf{(2.34)}$$

where the model constants are typically assigned the following values: $C_{\epsilon 1}$ = 1.44, $C_{\epsilon 2}$ = 1.92, σ_k = 1.0, σ_ϵ= 1.3, and Pr_t = 0.9 based on a wide range of experiments (Moukalled, Mangani, & Darwish, 2016). It is important to note that while equation (2.33) can be derived rigorously, equation (2.34) is an approximation relying on empirical data, and as such is widely blamed for the failures in the *k-ε* model in certain scenarios.

One key assumption in the *k-ε* model is that the flow is fully turbulent and the molecular viscosity is negligible relative to the turbulent viscosity. Some important results of these assumptions are first that the model is only valid for relatively high Reynolds numbers, and second that it cannot be applied to flows near the wall where viscous forces dominate. Damping wall models must be used alongside the standard k-ε equations to deal with the viscous boundary layer.

Variations of the *k-ε* model have been developed in an attempt to solve some of these issues. Researchers have attempted, with varying degrees of success, to adjust the values of the constants or develop equations that treat constants such as C_μ as variable to better model particular flow scenarios. Two common examples of adjustments made to improve the *k-ε* turbulence model for jet flows are the Chien Model (Chien, 1982), which is identical to the standard k-ε model aside from changing the constant values of $C_{\epsilon 1}$, $C_{\epsilon 2}$, and $\mathrm{Pr}_{t.}$, and the Tam-Thies Model (Thies & Tam, 1996), which modified constants, as well as splitting $C_{\epsilon 2}$ into 2 terms to include effects of vortex stretching. These and other models were investigated by

Georgiadis and Yoder and found to offer some improvements over the standard *k-ε* model for free jet flows, however no model is without its deficiencies (Georgiadis & Yoder, 2006).

2.4.4 *k-ω* Turbulence Models

The *k-ω* turbulence model is another of the most common RANS turbulence models. It is similar in form to the *k-ε* equation but defines the dissipation rate using ω, which is the rate at which turbulence kinetic energy is converted into thermal energy per unit volume and time:

$$\omega = \frac{\epsilon}{C_\mu k} \tag{2.35}$$

The eddy viscosity and turbulent heat fluxes, along with the transport equations, are described and derived similarly to their counterparts in the *k-ε* model (equations (2.30) - (2.34)(2.31)):

$$\mu_t = \rho \frac{k}{\omega} \tag{2.36}$$

$$\alpha_t = \frac{\mu_t}{Pr_t} \tag{2.37}$$

$$\frac{\partial(\rho k)}{\partial t} + \nabla \cdot (\rho \boldsymbol{u} k) = \nabla \cdot \left[\left(\mu + \frac{\mu_t}{\sigma_{k1}}\right)\nabla k\right] + \tau^R : \nabla \boldsymbol{u} - \beta^* \rho k \omega \tag{2.38}$$

$$\frac{\partial(\rho \omega)}{\partial t} + \nabla \cdot (\rho \boldsymbol{u} \omega) = \nabla \cdot \left[\left(\mu + \frac{\mu_t}{\sigma_{\omega 1}}\right)\nabla \omega\right] + C_{\alpha 1} \frac{\omega}{k}(\tau^R : \nabla \boldsymbol{u}) - C_{\beta 1} \rho \omega^2 \tag{2.39}$$

Where the model constants are typically assigned the following values: $C_{\alpha 1}$ = 5/9, $C_{\beta 1}$ = 0.075, σ_{k1} = 2.0, $\sigma_{\omega 1}$ = 2.0, β^*= 0.09, and Pr_t = 0.9 (Moukalled, Mangani, & Darwish, 2016).

This model solves some of the issues with the k-ε model in that it does not require high Reynolds numbers and can be fully integrated through the viscous sub-layer, eliminating the need for damping functions. One key drawback is that the solution has a strong dependence on the free stream values. This is often overcome by combining the k-ε and k-ω models, using the former in the free stream away from the wall and transitioning to the latter in the boundary layer.

2.4.5 Other Models

There are a variety of other turbulence models available in addition to the two-equation RANS models discussed above. Some of these models employ approaches other than the Boussinesq approximation to solve the closure problem in an attempt to avoid some the deficiencies of the approximation. These models are not nearly as common and are not a key focus of this research so their discussion is limited. Regardless of the model used, traditional validation of turbulence models is commonly performed using free shear flows and wall bounded flows, and as such, struggles to properly characterize flows such as impinging jets where fluctuations normal to the wall are larger than those parallel to it, and turbulent length scales near the wall are affected more by the length scales in the jet than the wall distance.

3 EXPERIMENTAL DETAILS

3.1 Loop Design and Specifications

The scheme of the experimental loop employed in the present study is displayed in Figure 3.1. The flow is supplied to the loop from a holding tank via a centrifugal pump. The flow is controlled via a Variable Frequency Drive to provide the desired flow rates. The initial and final sections of the loop are constructed from stainless steel tubing to ensure proper connections to the pump and the straight pipe lengths required for the magnetic flow meter and the jet development length. These two sections are connected by flexible cross-linked polyethylene pipes. The pipe that serves as the jet inlet development length is ¼” tubing with has an inner diameter of 4.57 mm and is 0.914 m or 200 diameters long; this guarantees the flow is fully developed flow at the exit.

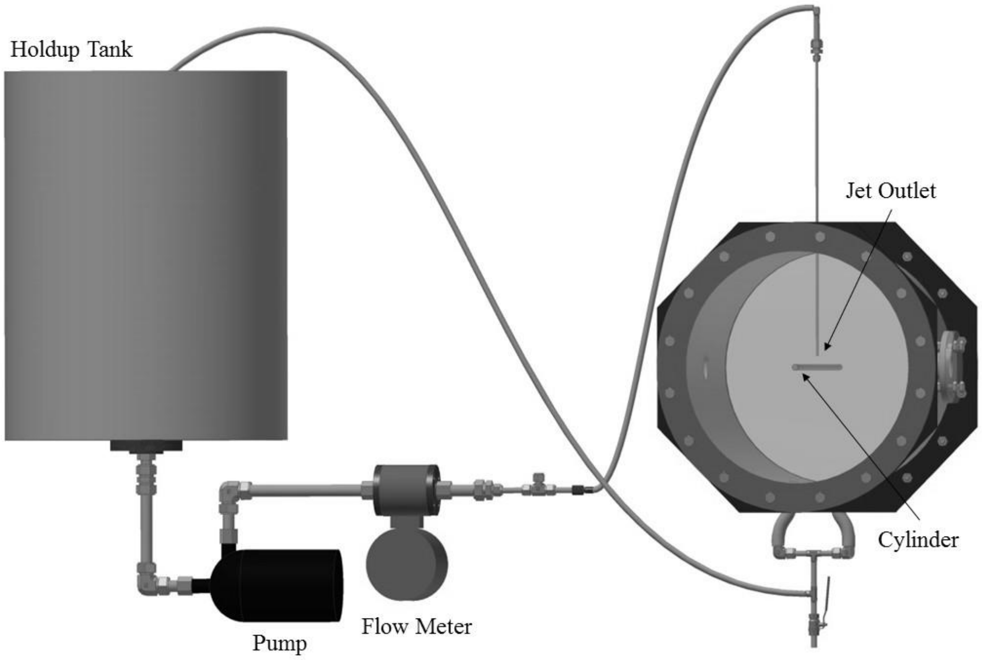

Figure 3.1: Experimental Loop

The cylinder is a resistance heater built by Stern Labs comprised of an Inconel filament surrounded by MgO insulation; a detailed illustration is seen in Figure 3.2. It has a design power of 1 kW with a cosine axial power profile seen in Figure 3.3, with an average surface heat flux of 47.5kW/m^2. For the experiments presented in this thesis, actual powers ranged from 0 to 500W, resulting in average heat fluxes of up to 23.75kW/m^2. Measured resistance of the heater was 0.384Ω.

Power was supplied to the heater from a standard 120V 60Hz AC wall outlet. The voltage across the heater was controlled via a Variac variable autotransformer and then sent though a step-down transformer with a turns ratio of 5:1. This provided a low voltage supply to the heater, with voltages ranging from 0 to 14.4V, resulting in currents of up to 35A.

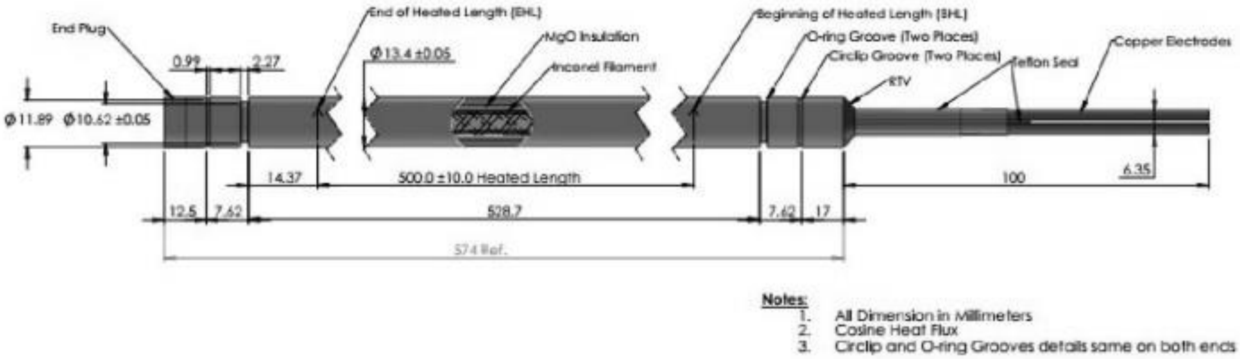

Figure 3.2: Heater Rod Schematic

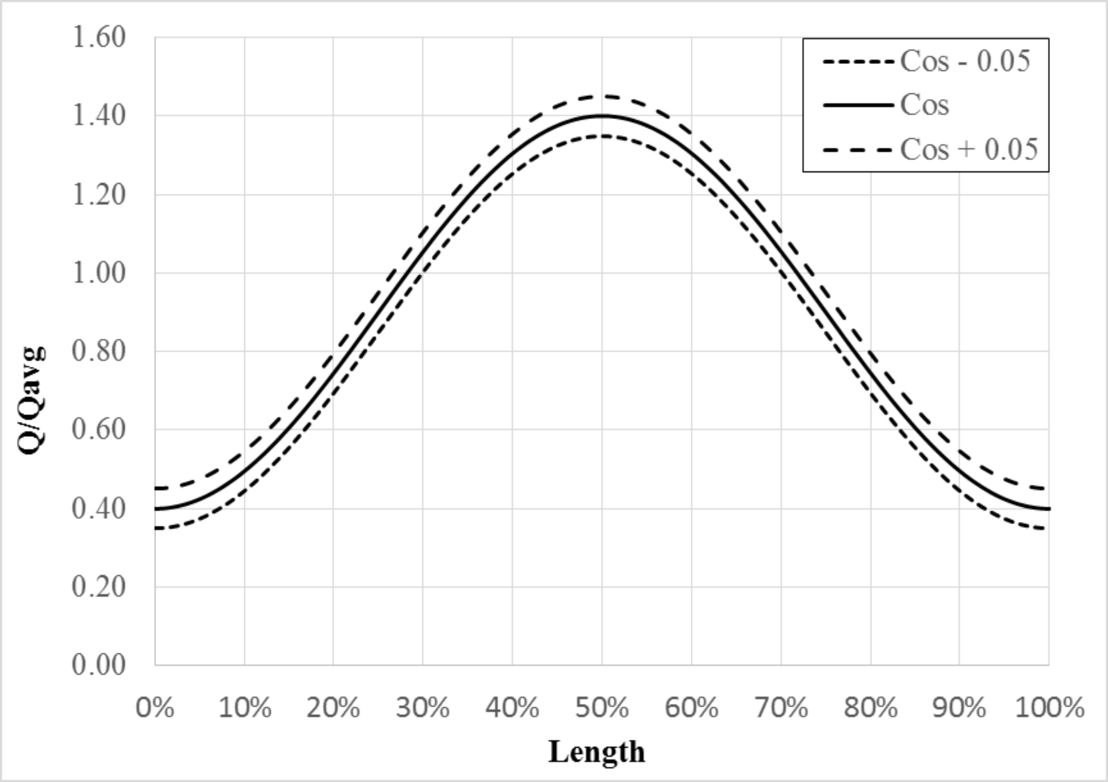

Figure 3.3: Heater Axial Power Profile

Due to the size and design of the tank holding the experiment, it was necessary to place the camera at the end of the heater. Since the only region of the heater that is cooled is the impingement zone of the jet, the segments of the heater outside this area create a heated plume along their lengths. The refractive index variations caused by this heated plume present an issue when attempting to take images of the jet, as there is approximately 25 cm of the generally unsteady plume between the camera and the jet.

To remedy this issue, a device was installed to suppress the distortions by cooling the segment of heater between the camera and jet and diverting any plume that may arise so as not to impede the measurements along the optical path between the PIV system and the measurement plane. This consisted of a pipe with holes in the side running parallel to the heater. Tests were conducted to confirm this optical distortion suppressor did not have any impact on the flows in the jet region. Figure 3.4 a) and b) show normalized velocity profiles at specified distances for Re=10 000 flow over an unheated cylinder with the optical distortion suppression on and off respectively; all differences fall well within the expected uncertainties (RMS of the difference between normalized velocities in the jet region was 0.025).

The cylinder is located at a distance of 18.29 mm or 4 jet diameters from the jet. Studies have examined the decay of the jet core and concluded that there is minimal shear layer interaction, and therefore minimal core decay, until h/d = 6 (Fekklouah, Ball, & Pollard, 2009). Therefore a cylinder distance of h/d = 4 allows confidence that the velocity effects as the jet impinges the cylinder are dominated by the interaction with the cylinder rather than the free jet decay.

There were three mass flow rates tested in this research, each at a variety of heater power levels, ranging from 0 to 500W:

- 4.79 kg/min, corresponding to a Reynolds number at the jet exit of 25 000 and average velocity of 4.87m/s
- 1.92 kg/min, corresponding to a Reynolds number at the jet exit of 10 000 and average velocity of 1.95m/s
- 0.96 kg/min, corresponding to a Reynolds number at the jet exit of 5 000 and average velocity of 0.97m/s

The choice to limit the Reynolds number to a minimum of 5 000 was made in order to avoid transitional Reynolds numbers where flow is not fully turbulent or fully laminar. As flow in CANDU moderators is turbulent, laminar flow cases were not investigated.

a) Without optical distortion suppression

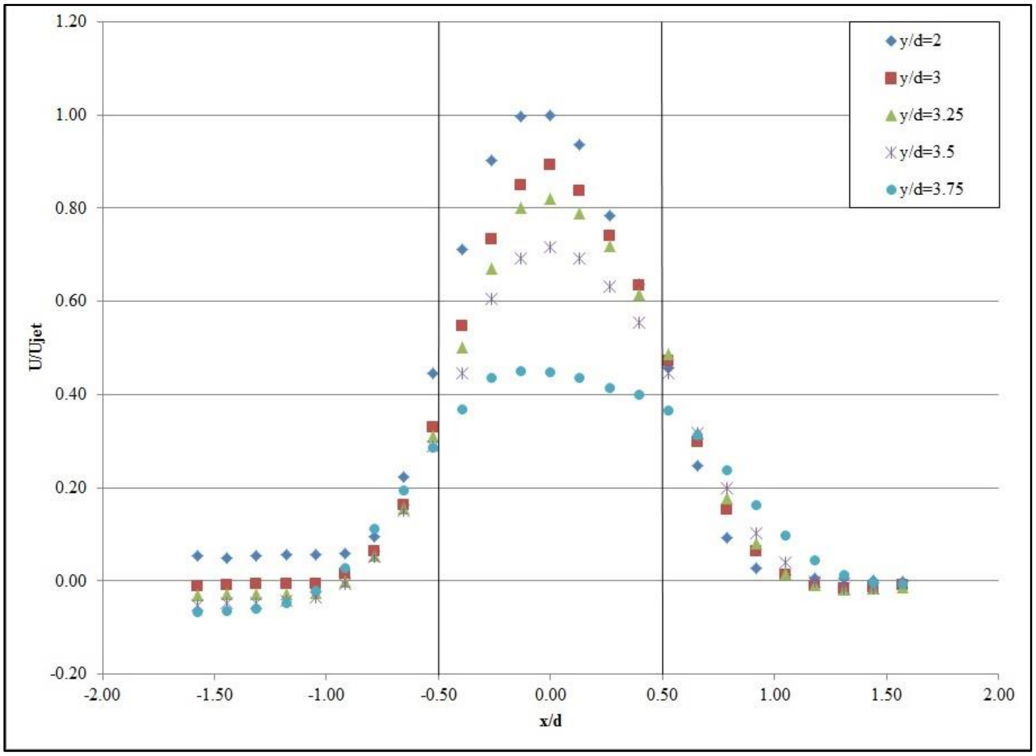

b) With optical distortion suppression

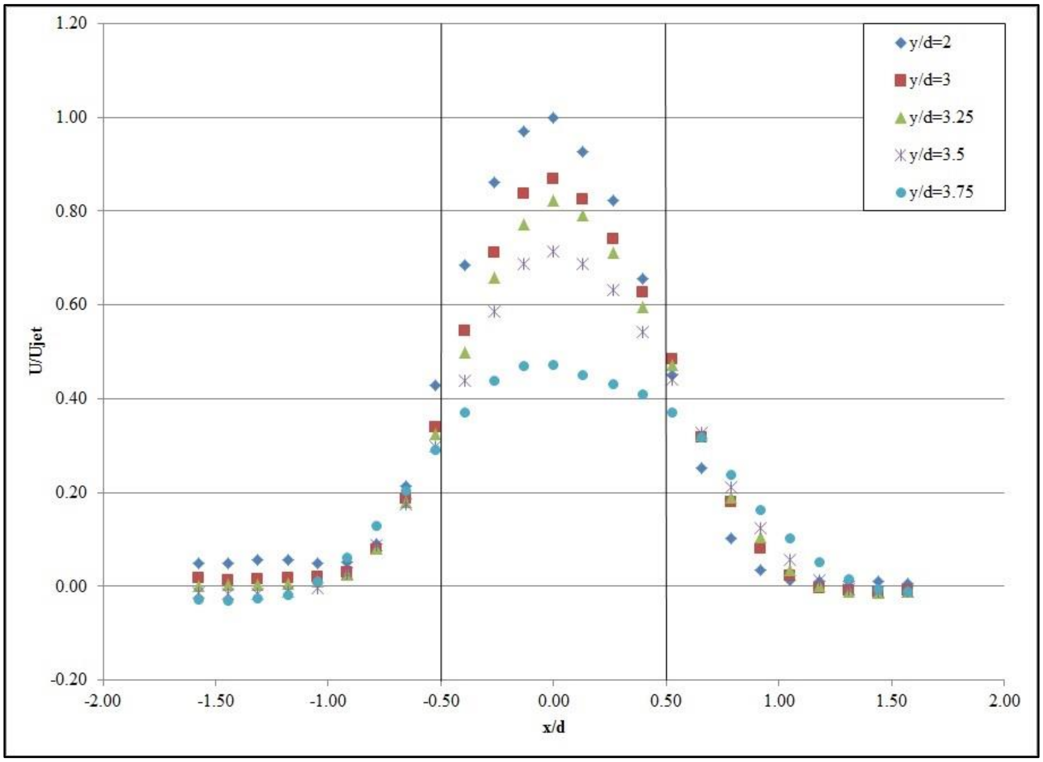

Figure 3.4: Effect of optical distortion suppression

3.1.1 Instrumentation

The heat balance is determined using two threaded Omega Engineering T-type thermocouples, one in the inlet piping before the flow development length, and the other in the outlet line. Four additional T-type thermocouples form the corners of a 40mm by 40mm square around the heater to gather temperature information about the fluid surrounding the jet and heater.

The data for the flow and temperature measurements was collected by a National Instruments CompactDAQ data acquisition system. The magnetic flow meter data was collected via a NI 9208 current input card connected to the CompactDAQ while data from the thermocouples was collected via a NI 9213 analog temperature input card connected to the system. The data was then parsed and saved using LabVIEW software.

To ensure the accuracy of the temperature measurements, the thermocouples were calibrated in the lab using the same wiring and connections as used in the experiments. The thermocouples were placed in a thermal bath with a pre-calibrated resistance temperature detector (RTD). At each 5°C interval, the RTD and thermocouple measurements were recorded. A least squares fit was applied to the data and all temperature measurements in the experiments were adjusted to this fitting.

The flow rate is monitored using a Rosemount magnetic flow meter and the power supplied to the heater was measured via an Ocean Controls MMX-P1-13YB AC Power meter. Both of these were calibrated externally. Table 3-1 shows the maximum uncertainties in each measurement component.

Table 3-1: Equipment Uncertainties

Equipment	Accuracy
NI 9208 – Flow Meter (Current) Module	0.8% F.S.
NI 9213 – Thermocouple Module	<0.25 °C
Ocean Controls Power Meter	0.25% F.S.
Heater	Resistance ±5% (±0.02Ω)
Flow Meter	0.5% F.S.

3.2 Particle Image Velocimetry

3.2.1 PIV Overview

PIV is a non-intrusive measurement technique for obtaining velocity field data. It involves seeding the flow with neutrally buoyant tracer particles that follow the flow. Two images are then taken by pulsing the laser in two different frames of the camera, an example timing diagram can be seen in Figure 3.5. These images are processed by the accompanying software, using correlations to determine the average distance travelled by the tracer particles within a pre-defined grid. Knowing the time between images and the distance travelled allows for the calculation of velocities.

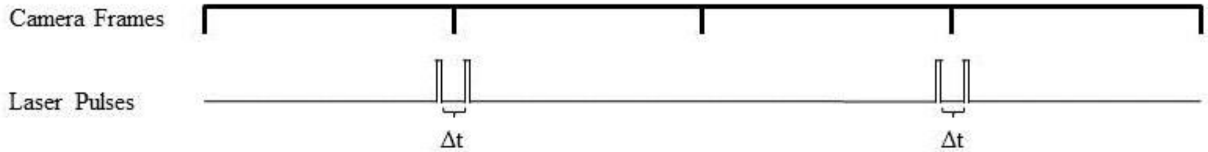

Figure 3.5: Sample PIV Timing Diagram

The primary advantages of PIV over other common measurement techniques are that it is non-invasive and has no influence on the flow, unlike hot wire anemometry, and that it is able to capture the entire velocity field at once, rather than taking line probe measurements or single point measurements as is necessary with Laser Doppler Velocimetry (LDV).

3.2.2 PIV setup

The measurements taken for this thesis used a Litron Model LDY301-PIV150W Pulsed Nd:YLF laser to illuminate the seed particles; the pulse and camera timing were controlled by the accompanying laser pulse synchronizer. The laser beam was directed using the TSI LaserPulse™ Light Arm; it then passed through a 25mm spherical lens to narrow the beam and finally a cylindrical lens with a focal length of 500mm to fan the beam out vertically into a sheet.

The light sheet was shone through a side window onto the side of the heated cylinder at a an angle of 90° from the axis of the cylinder and a distance of approximately 40cm from the jet centreline, while the camera was placed at the end of the cylinder, a distance of approximately 30cm, perpendicular to the light sheet. Orthogonality of the sheet was determined by placing markers on the opposite side of the tank and confirming the light sheet was aligned with these markers before measurements were taken. These markers also enabled confirmation of the thickness of the light sheet to be approximately 1mm in the area of investigation. The images were captured with a Photron SA5 Fastcam high speed camera and processed using INSIGHT 3G software using the models described in the following section.

3.2.3 Model Selections

The timing of the images taken depends on a variety of criteria, the most important of which are the grid size and the expected velocities in the area of interest. The timing interval must be small enough to ensure the seed particles do not travel more that 25% of the width or length of the interrogation spot size (i.e. a single grid square), this ensures most of the particles in a particular grid square are the same between the two images, which is necessary to have confidence in the correlation calculations. An illustration of how a large interval can impact velocity calculations can be seen in Figure 3.6, where image a) shows a clear movement from left to right with an appropriate selection of Δ*t*, whereas in image b) while the particles are still moving left to right, they appear to be moving up and to the left due to poor timing. A time interval that is too small must also be avoided; proper calculations cannot be made if the particles appear stationary; the general rule is that minimum particle displacement should be two particle diameters.

For the Re = 10 000 case, a time interval between laser pulses of 25μs with the images captured at a frequency of 500Hz consistently provided the highest percentage of good vectors. The definition of a good vector is discussed in more detail later in this chapter, but the basic definition is vectors for which the primary correlation peak is higher than any secondary peaks by a pre-defined amount. For the Re = 5 000 and 25 000 cases, the time intervals used were 35μs and 20μs respectively.

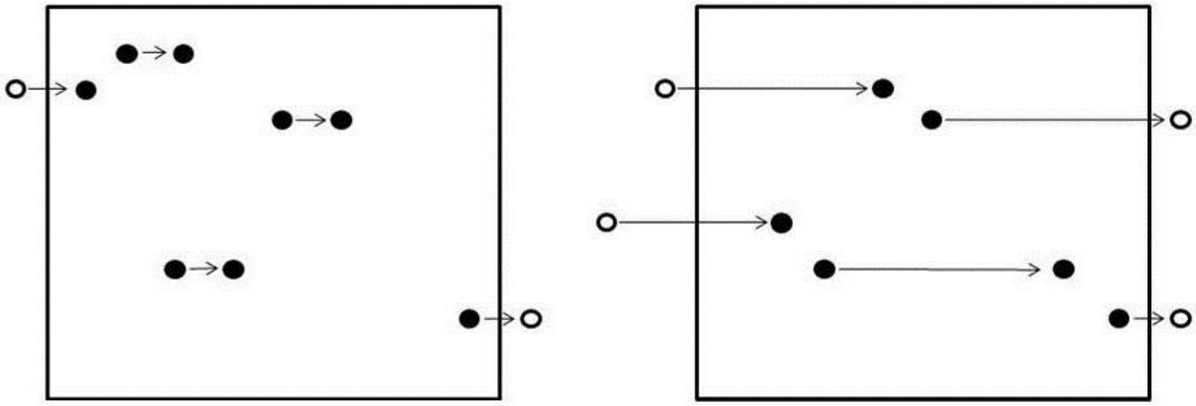

a) Appropriate Δt

b) Large Δt

Figure 3.6: Effect of PIV Time Interval Selection

A sufficient number of images must be taken to ensure the average has converged to the true mean. A 95% confident interval, meaning a 95% certainty that the true mean falls within this interval, can be calculated using Equation (3.1), where $\overline{x}$ is the sample mean, s is the sample standard deviation, and N is the number of images used in the calculation (Benedict & Gould, 1996). Note that the number of images used for a data point is rarely the total number of images taken due to holes or invalid vectors in the processing. For a sample size of 1 000 images, the average interval for axial velocity data points in the jet flow interval was narrower than ±1.5% of the sample average, with the largest 95% confidence interval not exceeding ±3%. This was deemed sufficiently converged for the purposes of this research.

$$\overline{x} \pm 1.96\left(\frac{s}{\sqrt{n}}\right) \tag{3.1}$$

Once a suitable number of images are collected, the images must be processed and the correlations calculated to determine the velocities. There are a number of options for the correlation algorithm, pre- and post-processing, and timing and grid options. The selections that proved most effective for this research are defined as follows.

Before any calculations are performed, the images are pre-processed by taking the minimum pixel intensity of all of the available images and subtracting that value from the pixel intensity of all of the other images. This removes a large amount of the reflected light and leaves the seed particles more clearly distinguishable. Figure 3.7 shows a sample image before and after the pre-processing.

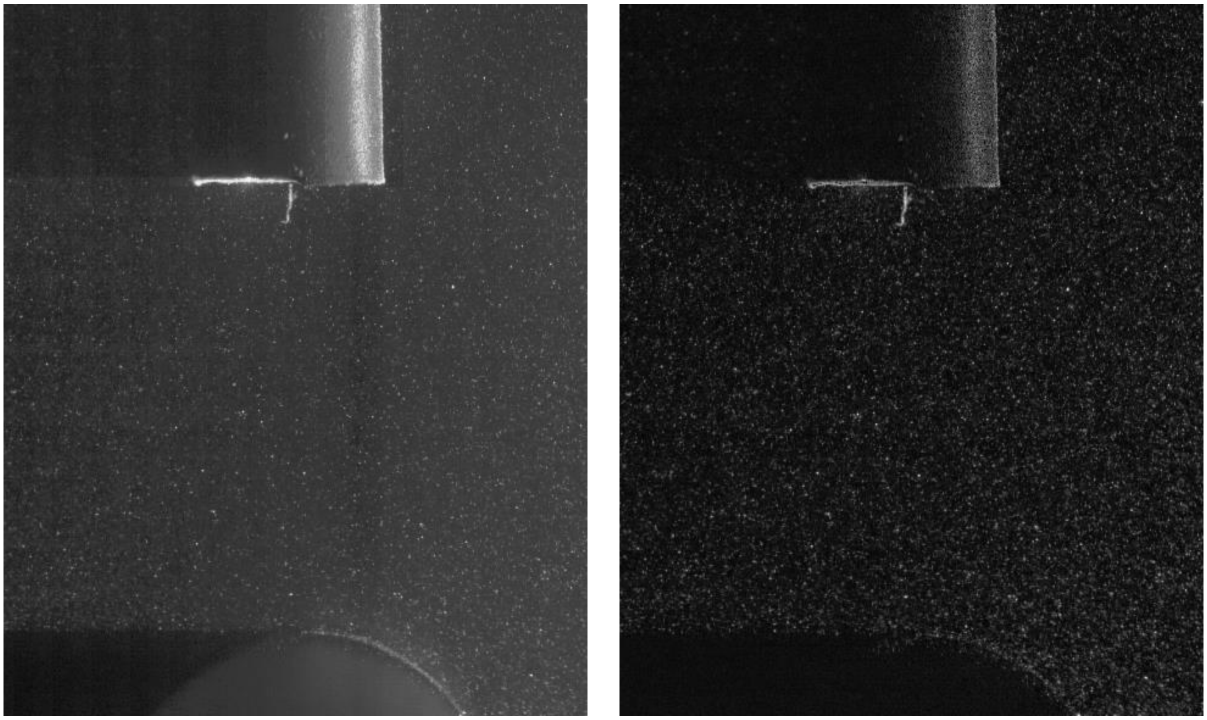

a) Raw Image b) Image after pre-processing

Figure 3.7: Effect of Image Pre-Processing

The resulting images are then processed using a recursive Nyquist grid; this is a two pass algorithm. The first pass uses a larger grid to determine the general direction of the flow. Provided the particles are still distinguishable, more seed particles in an interrogation area provide a higher probability of a valid velocity calculation, therefore a larger grid is more likely to result in a valid velocity vector. The second pass uses a smaller grid but rather than comparing the same area of the two images, the interrogation region for the second image is offset by the average displacement calculated in the first pass. This results in fewer “lost pairs” i.e. particles that exit or enter the interrogation area between images. For these experiments, an initial pass was performed with an interrogation spot size of 32 pixels, with the second pass using a spot size of 24 pixels.

The velocity calculations are performed by the correlation engine, the most common of which is the Fast Fourier Transform (FFT) Correlation. This is a computationally efficient method, however it requires treating the data as periodic, which can lead to difficulty distinguishing signals near the edge of the interrogation region. Once the correlations are calculated, the Gaussian peak engine is used to assess if the signal is distinct from the noise. A Gaussian curve is fit to the highest peak and its 2 closes neighbors in both the x and y directions. A peak is deemed valid if it is at least 1.5 times the magnitude of any other secondary peaks in the interrogation region. A direct correlation may also be performed, however the computational costs are higher with minimal benefit.

Using a Gaussian mask can help reduce issues with the FFT. The Gaussian mask multiplies each pixel by a Gaussian weighting factor so the spot is dark around the edges and brighter in the centre. This also helps to reduce the effect of lost pairs by giving the entering or exiting particles a lower value as these most commonly occur near the edges of an interrogation region.

Finally, post-processing is performed on the resulting vector fields. Given the statistical nature of the processing, there will be occasional occurrences of vectors that are deemed valid by the processing algorithm that are entirely unreasonable. To remove these spurious vectors, both global and local validations checks are implemented. For the Re=10 000 cases, the global validation removed any vectors resulting from a displacement of 10 or more pixels (corresponding to a velocity of 6.65m/s), and the local validation removed any vectors which exhibited a pixel displacement greater than seven pixels above or below the median of the 3x3 neighborhood (again corresponding to a difference of 6.65m/s). While these measures will not remove all spurious vectors, they will eliminate those with the largest magnitudes that would have the most effect on the averaged results.

This processing setup allowed for 95% or greater acceptable vectors for approximately 98% of the image pairs collected. Figure 3.8 shows a representative image of the vector field after all processing steps are complete.

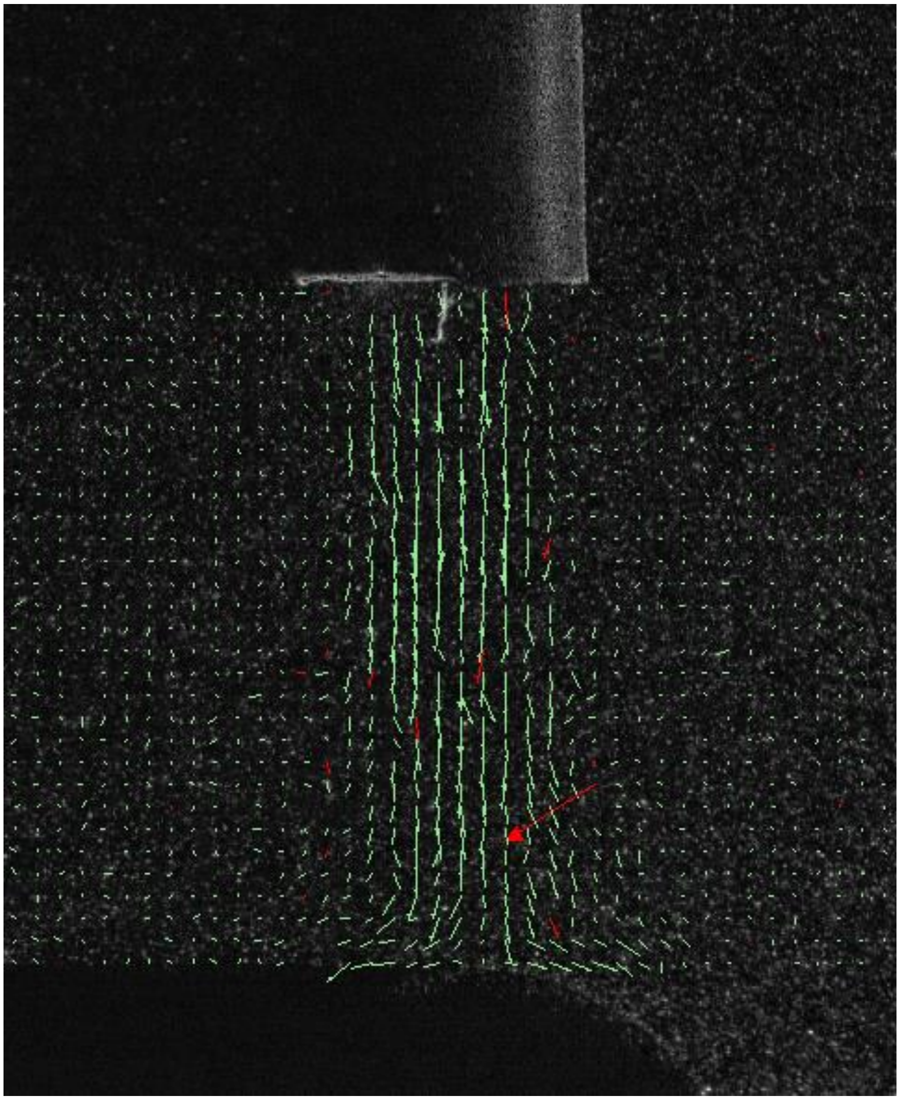

Figure 3.8: Final Result of Image Processing

4 CFD SETUP

4.1 Geometry and Meshing

In order to capture all effects present in the experiment, the entire tank was used as the geometry for the Computational Fluid Dynamics simulations. A structured hexahedral mesh was then applied to the geometry using the GAMBIT meshing software. A butterfly O-grid topology was applied to the inlet face of the jet and projected down onto the cylinder.

A mesh sensitivity study was performed using 14, 28, and 56 cells across the face of the jet. Due to the discordance between the straight line probes used to select the data of interest and the curvature of the grid near the cylinder, a coarse grid caused large discontinuities in the velocity plots as the line probes crossed into non-adjacent cells in a new row of the curved mesh (See Figure 4.1 for illustration). The 28-cell-wide jet face was employed to minimize these discontinuities while still remaining computationally viable. This grid, shown in Figure 4.2 (jet face overlaid on the bottom right), was used for the remainder of the simulations.

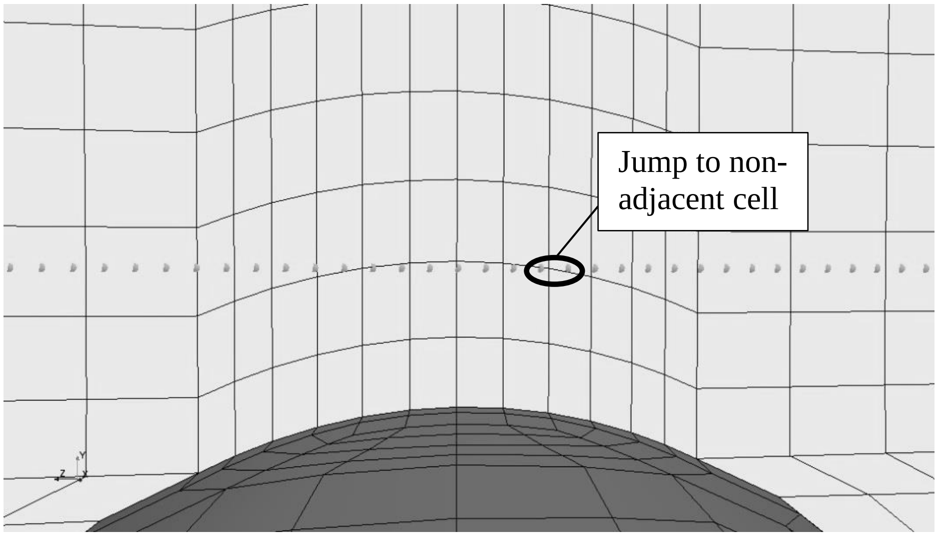

Figure 4.1: Straight Line Probe across Curved Grid

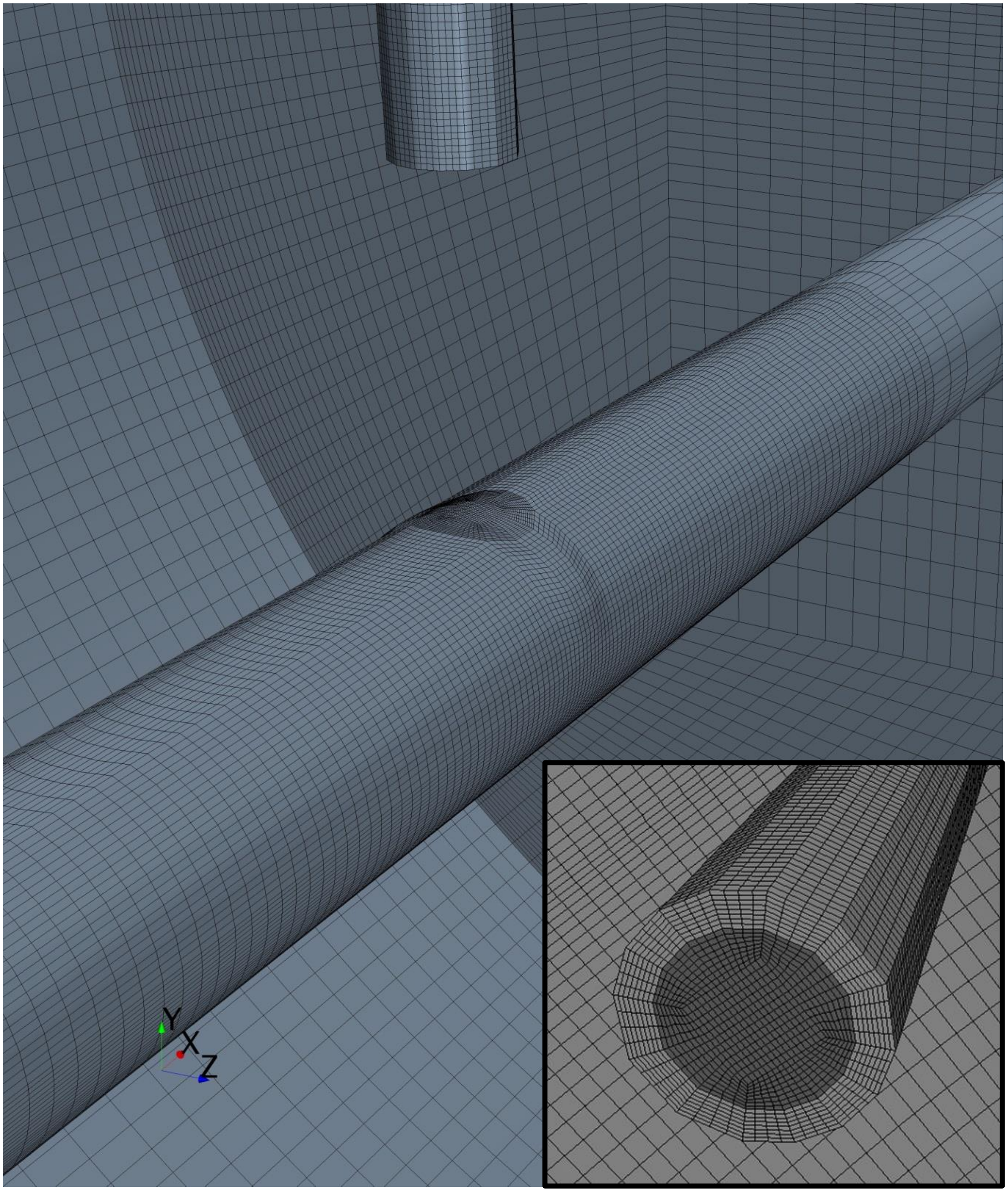

Figure 4.2: Meshed Geometry

Overall the mesh was comprised of 8.8×10^6 cells, concentrated in the region of interest near the jet and cylinder, with 64 cells between the jet and the cylinder corresponding to cells with a height in the jet centreline of 0.286 mm, which is approximately 1/10 of the pipe outlet diameter.

4.2 Models and Parameters

The elements of the turbulence model theory were detailed in prior sections; in this section the specific parameters and models employed in the present study are described. All simulations were performed in Star-CCM+ version 10.04.

4.2.1 Boundary Conditions

Boundary conditions have a large impact on the results for all CFD simulations, and as such, special care must be taken to ensure appropriate conditions are applied so as to allow fair comparisons with the experimental results.

The measured flow parameter in the experiments is the mass flow at the jet exit. Equation (4.1) gives the formula for calculating mass flow in a circular pipe from the velocity and density of the flow, as well as the radius of the pipe (R).

$$\boldsymbol{W = \int_0^R \rho u 2\pi r dr} \tag{4.1}$$

A well tested and widely used method for approximating the velocity profile for turbulent flow in a smooth pipe is the 1/7 power law profile (Xu & Antonia, 2002). Substituting the equation for this profile – given in Equation (4.2) – into Equation (4.1) above allows the maximum (centreline) velocity to be calculated (White, 1999). This maximum velocity can then be used to determine the velocity profile at the jet exit to be used in the simulations.

$$u = u_{max}\left(1-\frac{r}{R}\right)^{\frac{1}{7}} \tag{4.2}$$

The radius of the inlet pipe is 2.286x10^{-3}m, therefore using a reference density of 1000kg/m^3 and the aforementioned mass flows of 4.79 kg/min, 1.92kg/min, and 0.96 kg/min results in corresponding maximum velocities of 5.95m/s, 2.39m/s, and 1.2m/s respectively. Figure 4.3 shows a sample velocity profile across the centre of the jet for the Re = 10 000 case.

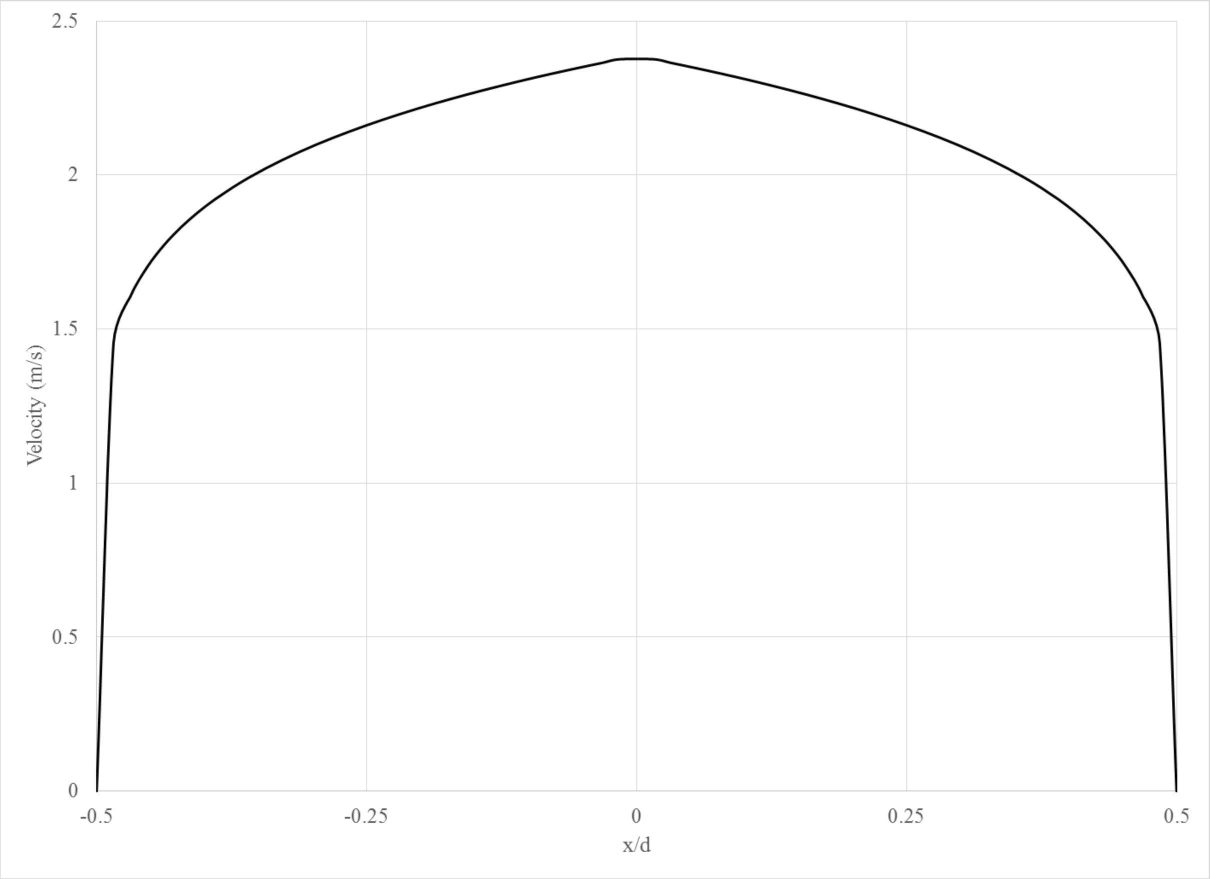

Figure 4.3: Jet Inlet Velocity Profile

In order to initialize the turbulence model, boundary conditions for the turbulence kinetic energy and the energy dissipation rate (whether ε or ω) must also be defined. These may either be specified directly or they can be calculated from a given turbulence intensity and length scale or turbulent viscosity. For circular pipe flow, the manual for Ansys Fluent CFD software recommends estimating the turbulent length scale as 7% of the hydraulic diameter. For the inlet pipe with diameter 4.572x10^{-3}m this gives a turbulent length scale of 3.2x10^{-4}m (ANSYS, Inc. , 2013). The remainder of the inlet conditions are calculated by Star-CCM+ using this length and the Reynolds number as given by the equations in Table 4-1 (C_μ is the same model constant seen in Equation (2.30))

Table 4-1: Inlet Boundary Turbulence Specifications

Re	$\mathrm{I} = \frac{u'}{\bar{u}} = 0.16\mathrm{Re}^{-\frac{1}{8}}$	$\mathrm{k} = \frac{3}{2}(\bar{u}\mathrm{I})^2$	$\epsilon = C_\mu^{\frac{3}{4}} \frac{k^{\frac{3}{2}}}{l}$	$\omega = \frac{k^{\frac{1}{2}}}{C_\mu^{\frac{1}{4}} l}$
5 000	5.52%	4.33x10^{-3} J/kg	0.15 J/(kg·s)	375 s^{-1}
10 000	5.06%	1.46x10^{-2} J/kg	0.90 J/(kg·s)	689 s^{-1}
25 000	4.51%	7.24x10^{-2} J/kg	10.0 J/(kg·s)	1535 s^{-1}

4.2.2 Physics Models

In addition to the turbulence model selected, a variety of other physics models must be chosen to fully define the treatment of the flows in the simulation. For all isothermal flows, the turbulent, three-dimensional, steady, liquid, gradients, segregated flow, and constant density models were selected. For the RANS k-ε simulations, both the standard and realizable variants of the k-ε model were used, in conjunction with a high-y+ wall treatment and all-y+ wall treatment respectively in order to avoid the near wall issues of the model as described in Section 2.4.3.

The high-y+ model uses the log-law velocity profile at the wall to model behaviour near the wall, requiring that the centroid of the first cell abutting the wall is within the log layer. This generally requires y+ values of approximately 30, however it is acceptable for a few cells, especially near stagnation or separation, to have a small y+ value. For the k-ω simulations, the standard (Wilcox) model was employed using an all-y+ wall treatment as the k-ω model does not suffer the same near-wall issues as the k-ε model. The all-y+ model is a hybrid between the high-y+ model and the low-y+ model, which assumes the viscous sublayer is well resolved by the grid. A weighting function based of the local wall-distance-based Reynolds number is used to blend the two approaches. For the all y+ model, the Star-CCM+ manual confirms that intermediate y+ values (i.e. $5 < y+ < 30$) will provide reasonable results.

For the Re = 25 000 and 10 000 simulations, the y+ values were above the general threshold of 30 in nearly all areas of the impingement region. The Re = 5 000 case results in y+ values in the mid-teens. As previously noted this should be acceptable when using the all-y+ model, but may raise concerns for the high-y+ model. As will be shown in the following section, the results of the standard *k-ε* model using the high-y+ model closely resemble those of the models using the all-y+ model. As such it was decided that the importance of grid resolution and consistency between simulations outweighed the need for the y+ value to meet the recommended threshold.

5 RESULTS

5.1 Benchmark Study

Prior to performing the simulations required for this thesis, a benchmark study was conducted to ensure competency with the turbulence modelling and that the turbulence models were returning reasonable results. The geometry and model parameters used in these benchmark tests were based on the experiments performed by Esirgemez et. al. (Esirgemez, Newby, Nott, Ölçmen, & Ötügen, 2007), and subsequently modeled by Sing et. al. in a later study (Singh, Premachandran, & Kohli, Numerical simulation of the jet impingment cooling of a circular cylinder, 2013b).

In the Esirgemez study, air exits a contoured nozzle, resulting in a uniform velocity profile at the jet exit. The jet is situated below a cylinder at a distance of h/d = 4, with d/D = 0.252. Laser Doppler Velocimetry (LDV) measurements were than taken of a jet with Re = 25 000 at distances of y/d = 2, 3, 3.25, 3.5, 3.75 and 3.95.

The geometry was modelled for use in Star-CCM+ and simulations were conducted using the standard *k*-*ε* turbulence model in an attempt to model the flow behaviour. The results of this simulation as compared to the results of the experimental study are shown in Figure 5.1. It was found that this model over-predicted the jet velocities in the free shear flow until between 0.5 and 0.25 jet diameters from the cylinder, at which point the model begins to under-predict the core velocities.

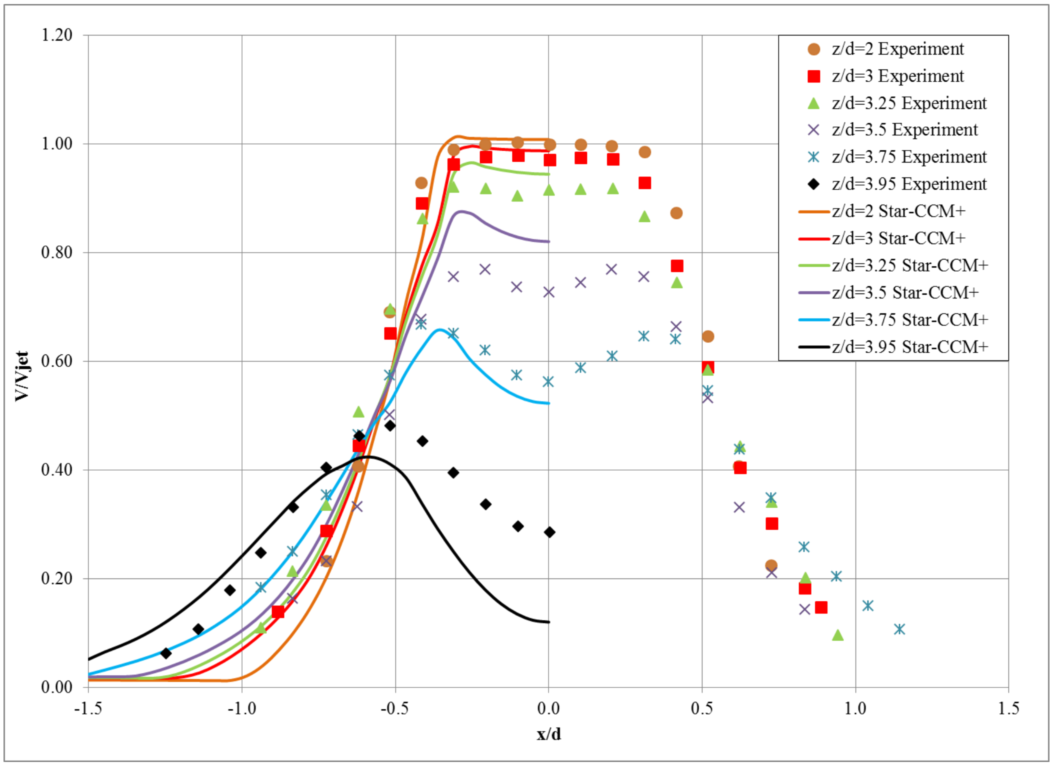

Figure 5.1: Comparison of Benchmark Simulation to Experimental Data

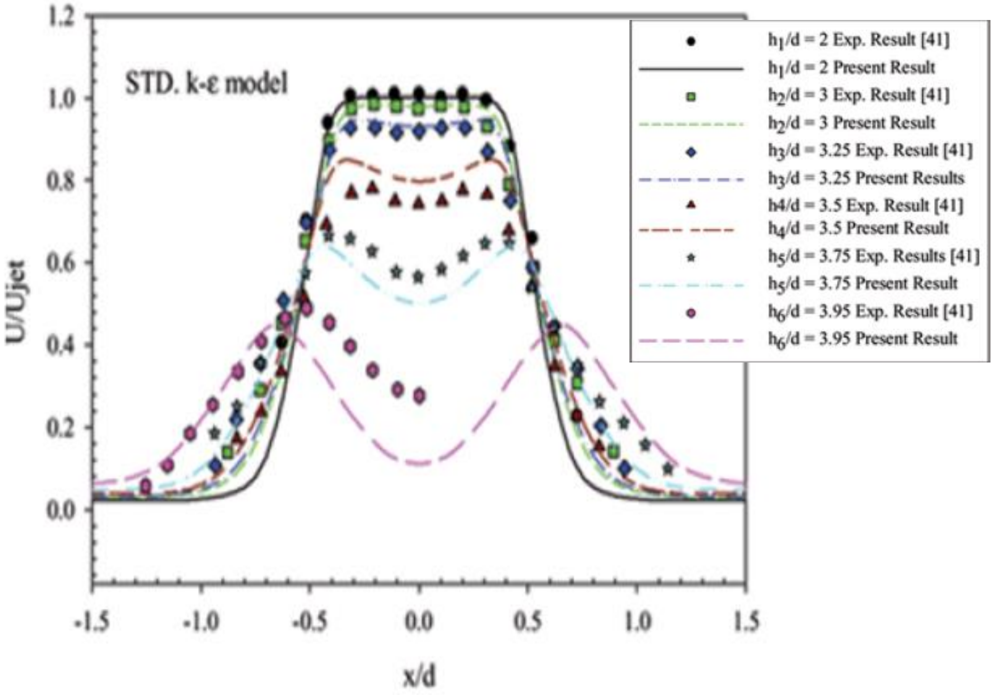

Figure 5.2: Comparison of CFD to Experimental Data (Singh, Premachandran, & Kohli, Experimental and numerical investigation of jet impingement cooling of a circular cylinder, 2013a)

These simulation results were then compared to the study which performed a similar comparison. The results from this published paper matched the benchmark simulation closely, as can be seen in Figure 5.2. A variety of other simulations were conducted to compare grid sizing and assess different model parameters, however this summary should be sufficient to establish that the modelling practices used throughout this thesis are in reasonable agreement with existing literature.

5.2 General Profiles

In the rest of this section, a thorough discussion of the results obtained from the simulations and experiments is presented. Important differences caused by the adjustable parameters such as Reynolds numbers or heating of the cylinder will be highlighted. Figure 5.3 - Figure 5.6 are a good reference point for the following discussions, these are examples of the velocity profile as the jet approaches the cylinder. Two examples are given for both the simulation results and the experimental results, one showing the velocities along the jet axis (V), the others showing those perpendicular to the jet (U), each normalized by the centreline jet velocity at the cross-section at y/d=2. While in similar studies, velocities are often normalized by the jet velocity at the inlet, there is high uncertainty in the PIV measurements at the inlet so the velocity at this cross section is a more reliable metric by which to normalize the data. All results discussed are variations of the same basic behaviour seen here. .

It is evident in Figures Figure 5.4 and Figure 5.6 that there are discontinuities in the simulation data. This is due to the issue previously discussed in the CFD setup section with regards to the conflict between the curved grid and the straight cross section probes. The data presented here represents the best compromise between the computational requirements for the simulation grid and the collection of the desired information.

All experiments were repeated a multiple times to ensure the reliability of the measurements taken. A typical standard deviation for the jet velocities between tests was in the range of 2-4% of the centreline jet velocity. The error bars on these charts of the experimental data are based on typical PIV uncertainty measurements and are an indication of the uncertainties of measurements throughout the remainder of this thesis (Lazar, BeBlauw, Glumac, Dutton, & Elliot, 2010)

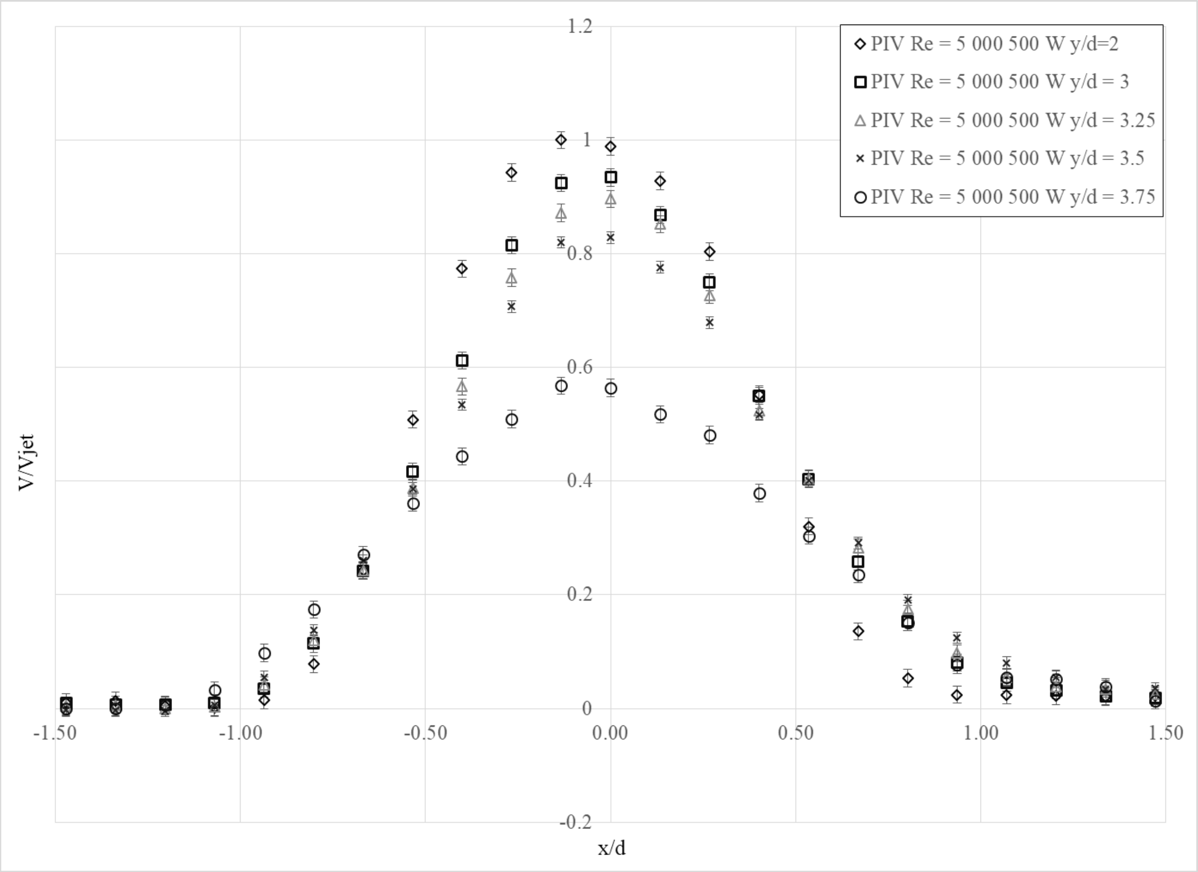

Figure 5.3: Typical Jet Velocity Profiles (Experimental, Zero Power, Re = 5 000)

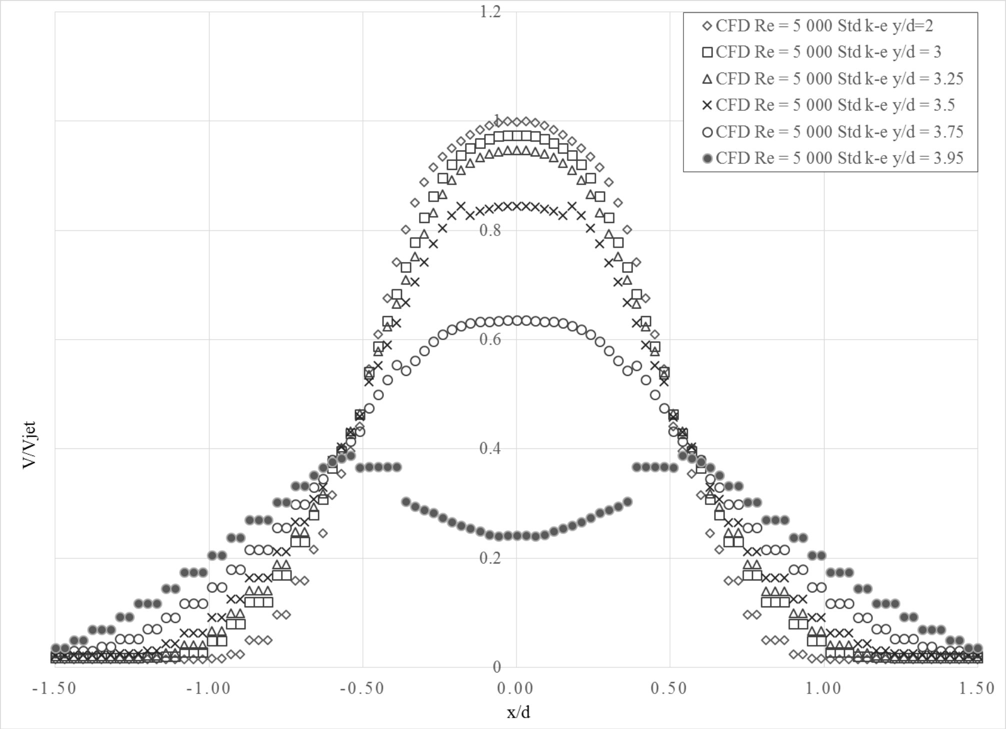

Figure 5.4: Typical Jet Velocity Profiles (CFD, Standard k-ε, Re = 5 000)

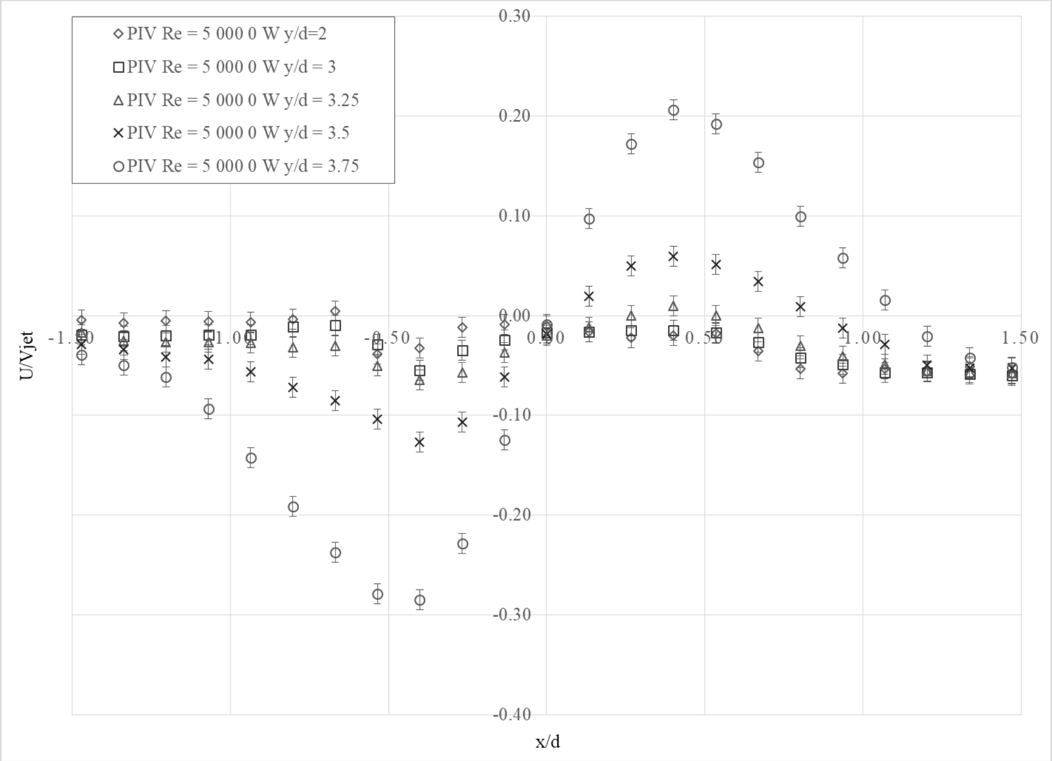

Figure 5.5: Typical U Velocity Profiles (Experimental, Zero Power, Re = 5 000)

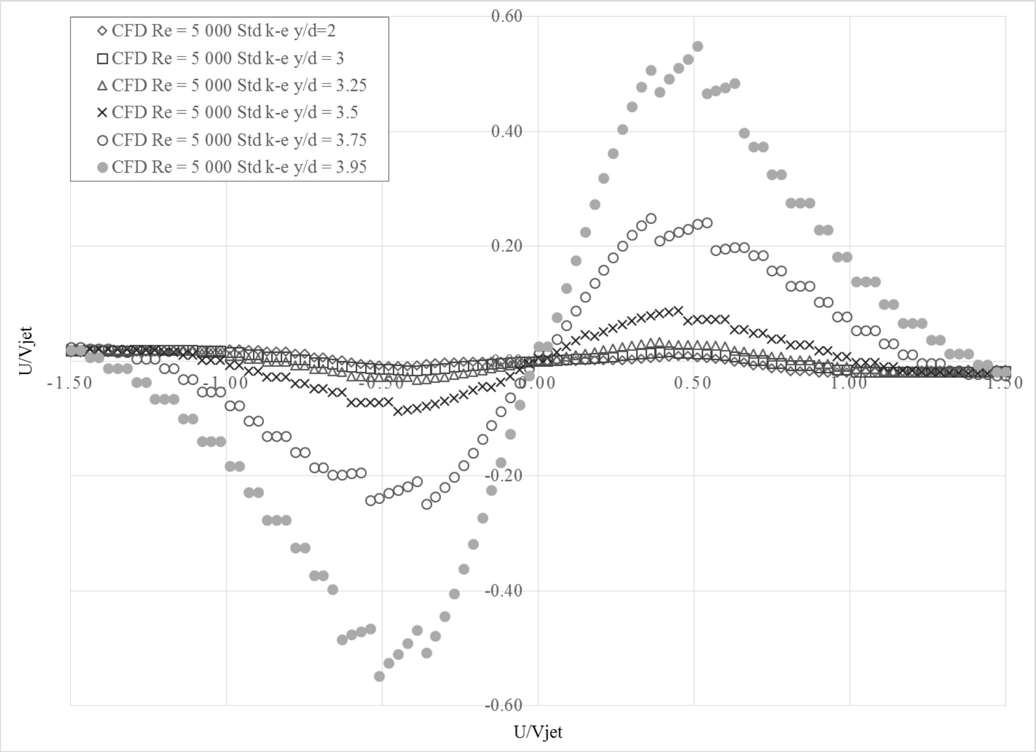

Figure 5.6: Typical U Velocity Profiles (CFD, Standard k-ε, Re = 5 000)

5.3 Performance of Turbulence Models

In comparing the CFD results with the experimental data it was found that, in general, the agreement was reasonably good, with the most obvious errors being the slight over-prediction of jet core width and normalized velocities. Figure 5.7 shows the Re = 10 000 experimental jet velocity data plotted against the results of the simulation results from the realizable *k-ε* model for illustration.

The agreement was best for the Re = 10 000 and 5 000 cases at 2 jet diameters from the cylinder. As the jet approached the cylinder, greater discrepancies began to arise. The CFD simulations both over-predict the normalized velocities in the inner shear layer near the impingement zone as well as under-predict the spreading of the jet. In the simulations, the core region of the jet was larger than was found in experiments, with the jet centreline velocity gradient beginning at between 0.25 and 0.35 diameters from the centreline, whereas the experiments showed the velocity beginning to drop off starting from the centreline

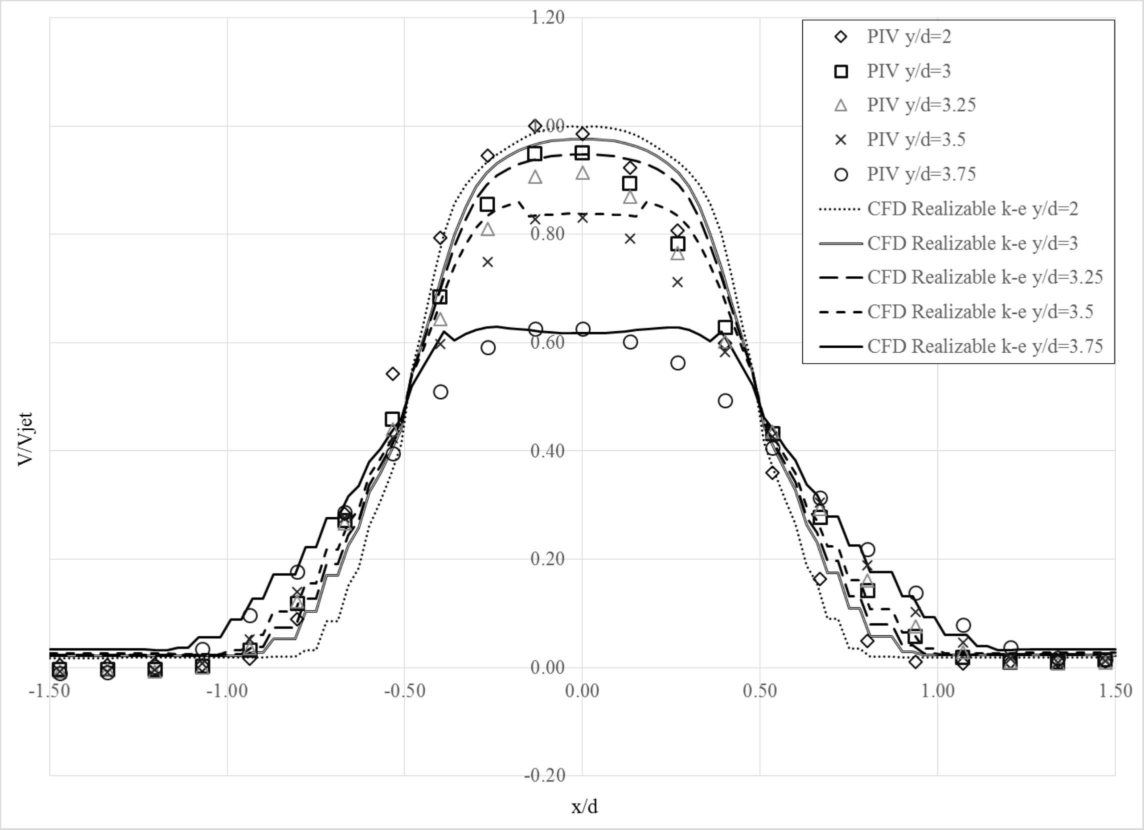

Figure 5.7: Comparison of CFD and PIV Results (Re = 10 000, Realizable k-ε Model)

5.3.1 Jet Velocity

5.3.1.1 V Velocities

As Figure 5.8 shows, all turbulence models over-predict the jet velocity as the jet impinges on the cylinder for the Re = 5 000 case. The shape of the velocity profile is best predicted by the standard k-ε model, however the results exceed the experimental data by approximately 20%. The k-ω model appears to predict a flattening in the velocity profile that does not occur in the experimental results. The emergence of this flattening in only present within 0.5 jet diameters of the cylinder, and appears to have a notable impact on the accuracy of the velocity prediction in the shear layer at a y/d of 3.75.

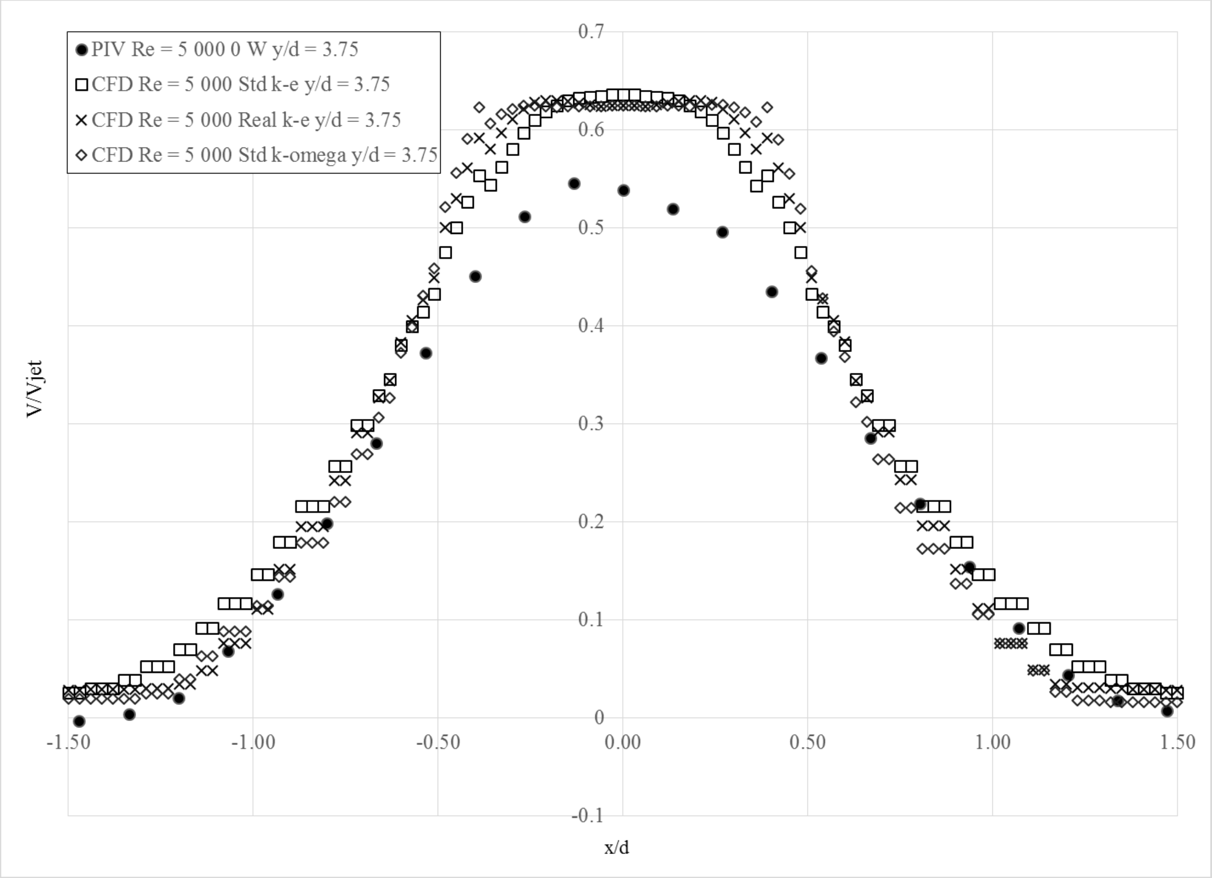

Figure 5.8: Comparison of Experimental and Simulation Results (y/d = 3.75, Re = 5 000)

The flattening of the velocity profile predicted at this distance by the *k-ω* and realizable *k-ε* models is also present in the Re = 10 000 results, however the over-prediction of the centreline velocity is no longer present. The Standard k-ε model provides an accurate prediction for all V Velocities in the Re = 10 000 case.

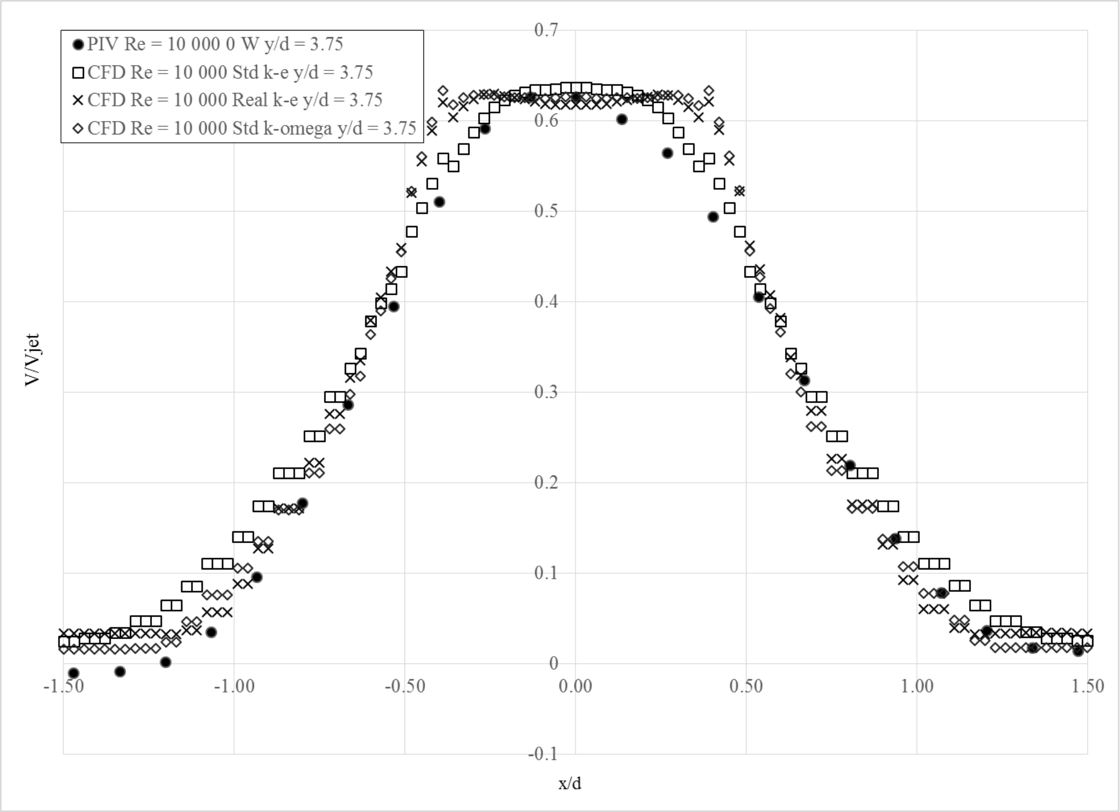

Figure 5.9: Comparison of Experimental and Simulation Results (y/d = 3.75, Re = 10 000)

The experimental results for the Re = 25 000 case exhibited some very different behaviour as compared to the Re = 5 000 and Re = 10 000 cases. As Figure 5.8 and Figure 5.9 show, the centreline velocities as the jet reaches the cylinder reduce to 50-65% of the maximum jet velocity, while outside of the shear layer the velocities are negligible. The Re = 25 000 data however shows significant negative velocities outside of the jet region, present at all jet distances investigated in the range of V/Vjet = -0.10 to -0.30. This flow reversal does not appear in any of the CFD results.

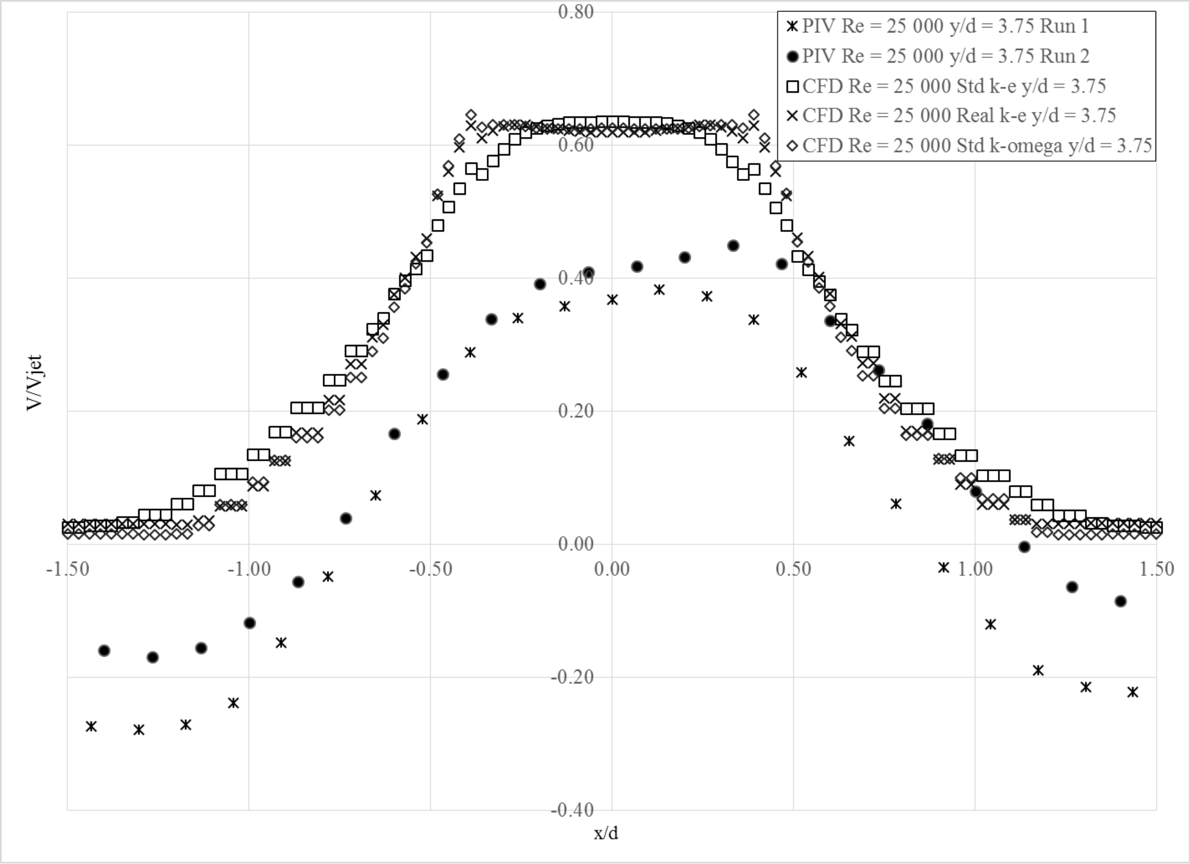

Figure 5.10: Comparison of Experimental and Simulation Results (y/d = 3.75, Re = 25 000)

As these experiments were repeated multiple times with complete disassembly and reassembly of the measurement equipment and experimental setup between runs, it is not likely that the effects are due to a measurement anomaly or setup error. As there are no reasonable physical explanations for why the flow should behave as it appears to, the setup of parameters used for the PIV data processing is the most likely reason for the odd behaviour as it was the same between runs.

5.3.1.2 U Velocities

The velocity profiles in the axis orthogonal to jet become meaningful near the impingement zone. As illustrated in Figure 1.4 for flat plates, at distances farther from the cylinder, there is no impact on the U velocities from the impingement, as such the focus for this will be on the area closest to the cylinder; in the case of these experiments this will be the measurements taken at y/d = 3.75.

As shown in Figure 5.11, all turbulence models predict the velocity profiles along the x axis well. There is negligible difference between the models, with the Standard *k-ε* model predicting slightly lower peak velocities and a slightly more gradual decline as the reflected flow progresses. A slight asymmetry can also be seen in the experimental results. This may be due to a minor misalignment or tilt in the jet. The velocity profiles and accuracy of the turbulence models for the Re = 5 000 case are very similar to those of the Re = 10 000, while the Re = 25 000 measurements suffer the same issues identified in the previous section.

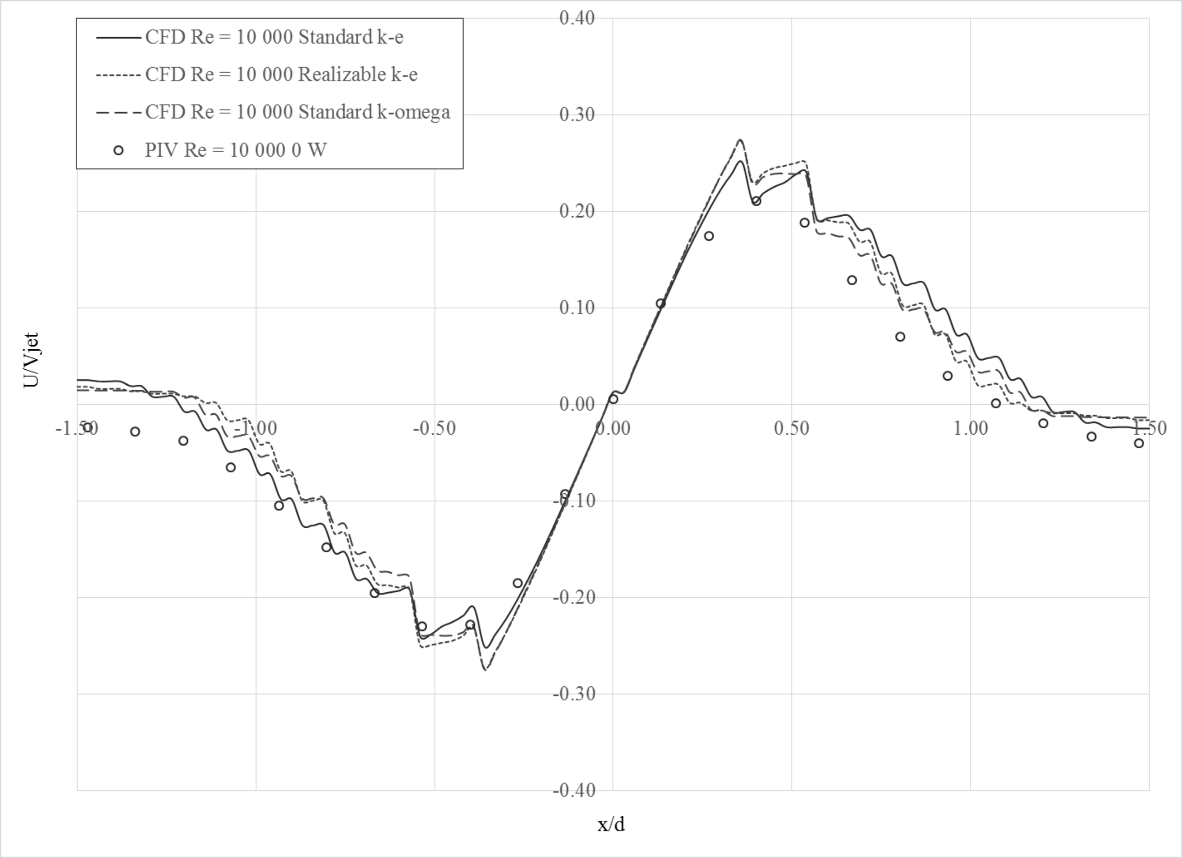

Figure 5.11: Velocity Profiles Perpendicular to Jet (Re = 10 000, y/d = 3.75)

5.3.2 Turbulence

Figure 5.12 - Figure 5.15 show a half-jet profile of the turbulence kinetic energy for the experimental results and each turbulence model for the Re = 5 000 at select distances from the cylinder. The general pattern present in all figures shows the expansion of the turbulent shear layer as the jet emerges and proceeds to impinge on the cylinder. One key failing common among all turbulence models presented is the over-prediction of the peaks in the normalized turbulence kinetic energy as the jet impinges the cylinder. In addition, the peaks in turbulence kinetic energy are predicted to be farther from the jet centreline than the experiments showed.

A possible explanation for this discrepancy is the Boussinesq approximation used to estimate turbulent shear stress. Linear eddy viscosity models such as the Boussinesq approximation have been known to over-predict the turbulence production term near the impingement area (Cooper, Jackson, Launder, & Liao, 1993). It is interesting to note that the error is largest in the standard *k*-*ε* model in the peaks in the shear layer, however it exhibits the most accurate predictions in the core region near the impingement zone.

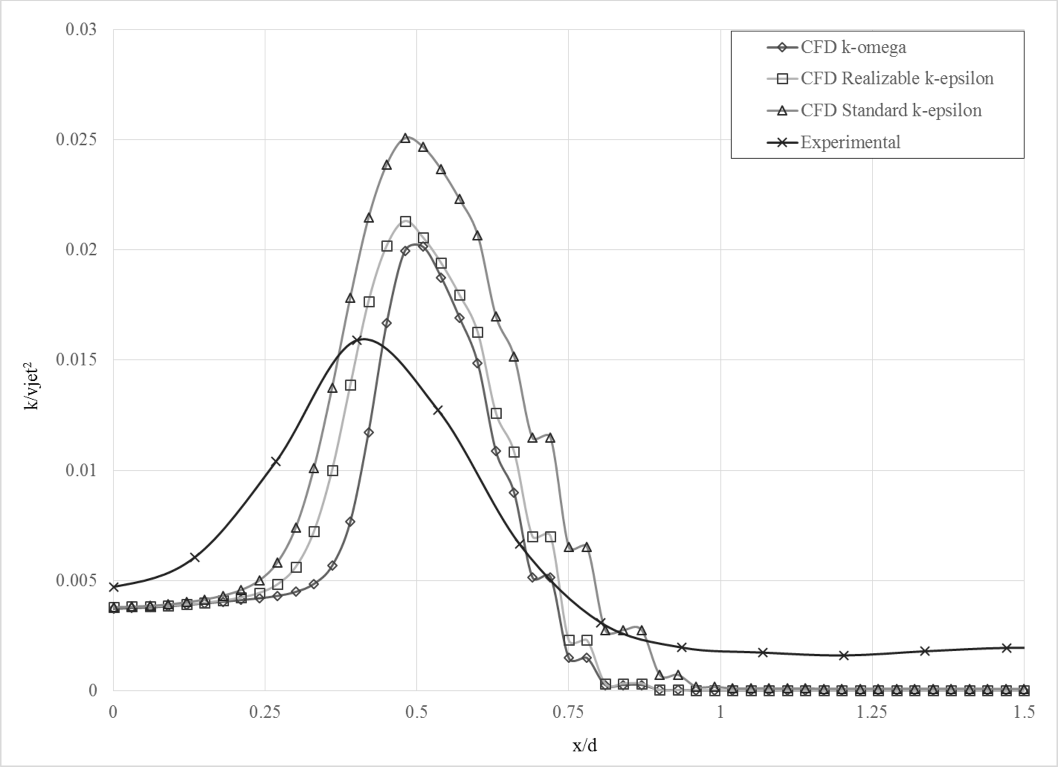

Figure 5.12: Comparison of TKE Profiles (y/d = 2, Re = 5 000)

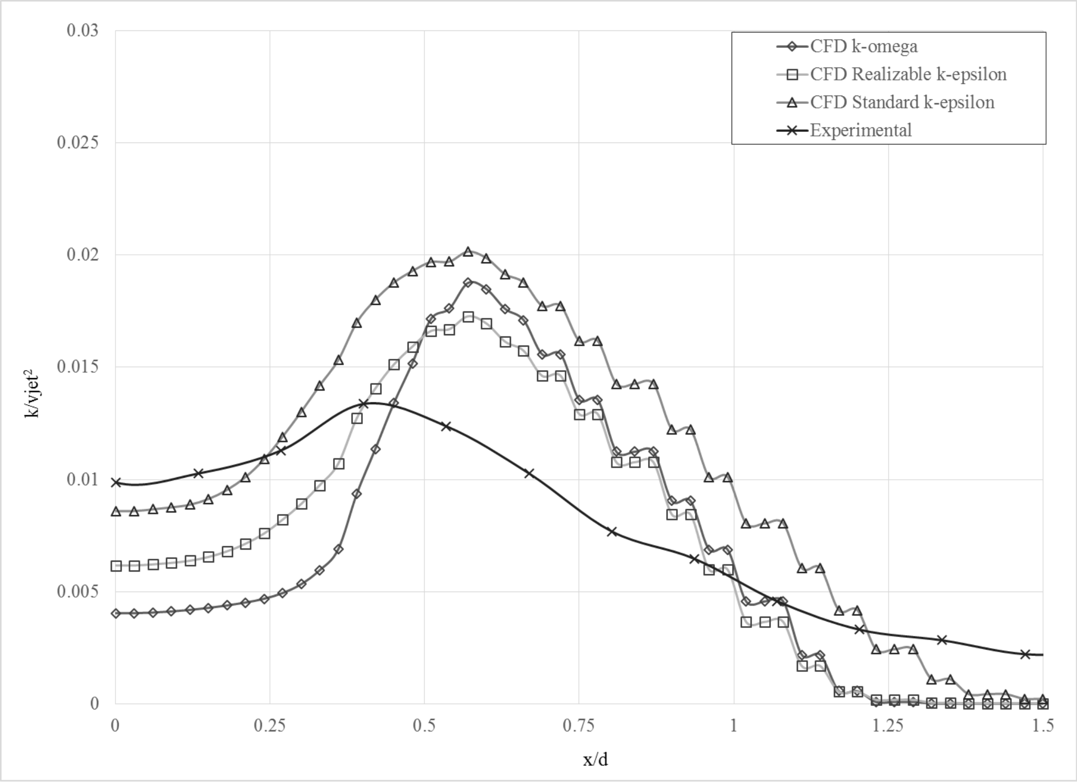

Figure 5.13: Comparison of TKE Profiles (y/d = 3.75, Re = 5 000)

While there appear to be some discrepancies between the simulations and experiments with regard to the magnitude of the turbulence kinetic energy profiles. The relative pattern of behaviour as the jet impinges the cylinder is reasonably well predicted. The peaks in the turbulence kinetic energy are highest and exhibit the steepest gradients farther from the cylinder, while the data closest to the cylinder exhibits a lower peak TKE and experiences a more gradual decline. Figure 5.14 and Figure 5.15 show an example of the patterns of TKE at varying distances from the cylinder for a simulation and the experiment, demonstrating the changes as the jet approaches the cylinder.

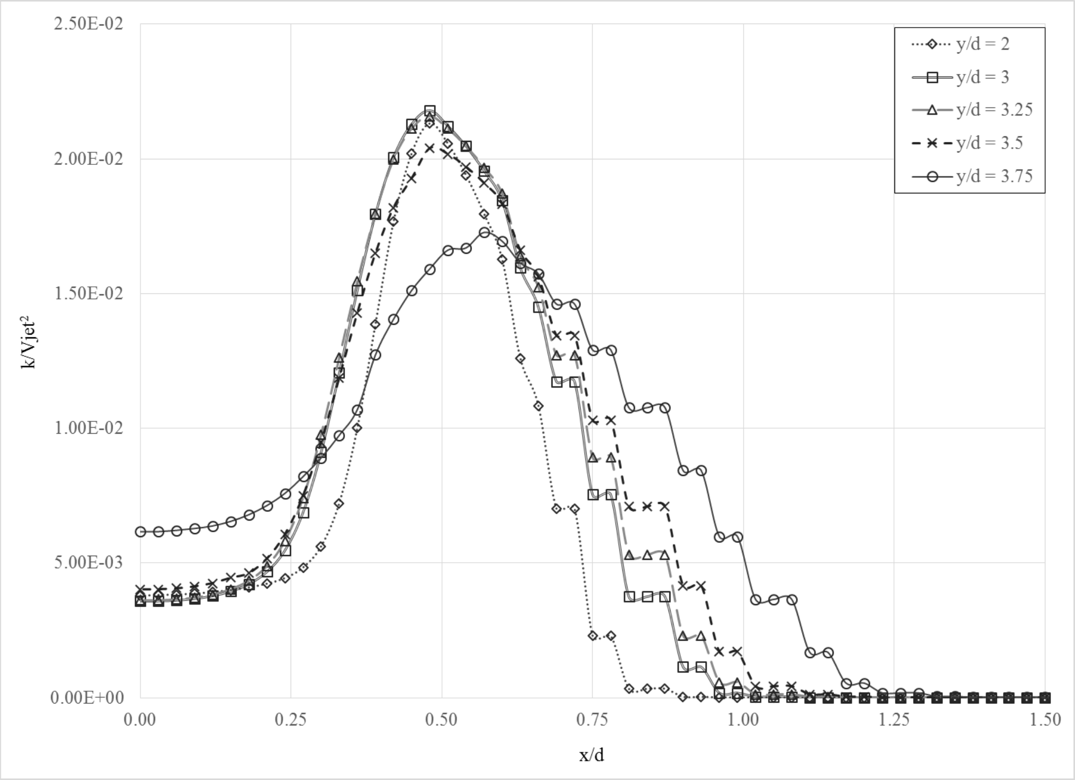

Figure 5.14: Realizable k-ε Turbulence Kinetic Energy Profile (Re = 5 000)

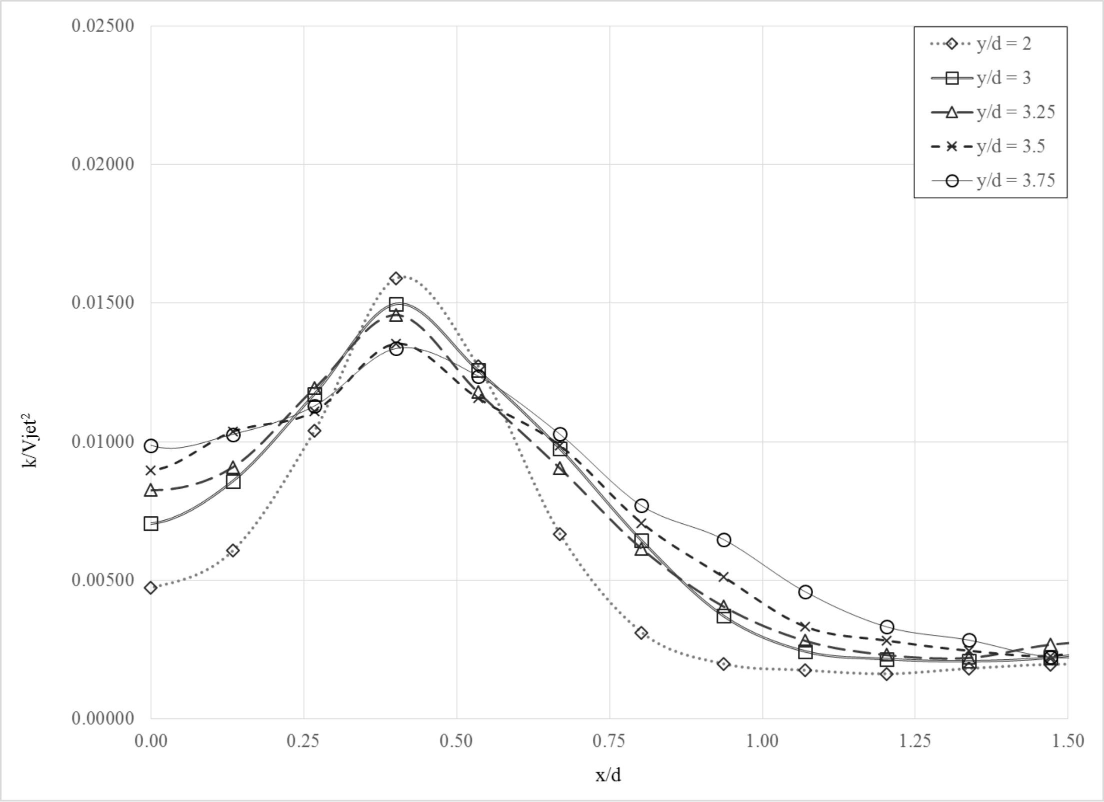

Figure 5.15: Experimental Turbulence Kinetic Energy Profile (Re = 5 000)

The turbulence profiles for the Re = 10 000 and 25 000 cases take a very similar shape to those in the Re = 5 000 case, see Figure 5.16. In the experimental data, there is an asymmetry in the magnitude of turbulence about the axis of the jet, with the simulation results generally falling between the values of equal distance on opposite sides. As such it is difficult to decisively assert which turbulence model provides the most accurate results. However the pattern of the turbulence kinetic energy profiles is predicted well by all turbulence models.

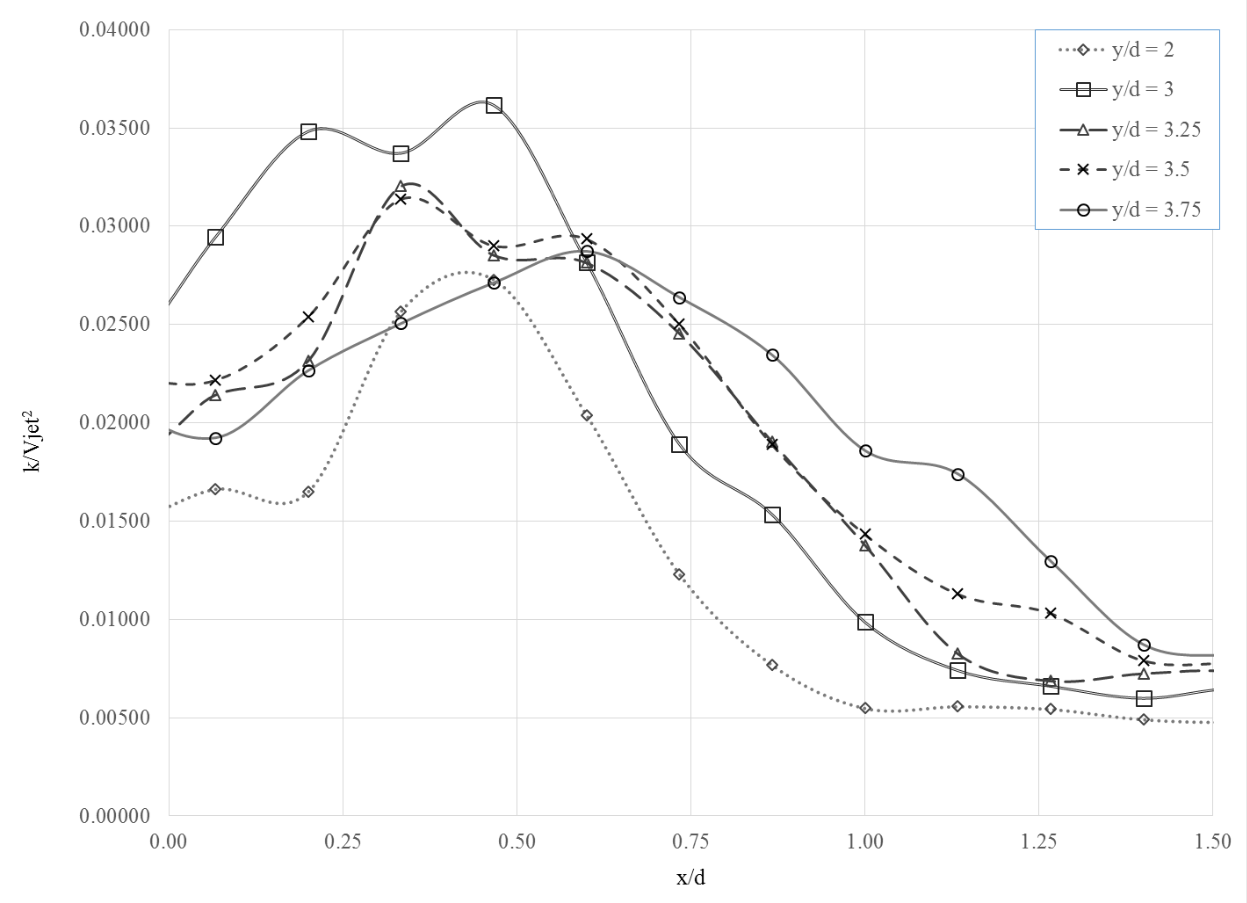

Figure 5.16: Experimental Turbulence Kinetic Energy Profile (Re = 25 000)

5.4 Reynolds Number Effects

5.4.1 Jet Velocity

While the absolute peak velocities will, by definition, differ based on Reynolds number, when normalized by the centreline jet velocity, the velocity profiles of the flow at the chosen cross sections are similar in the jet core region, often referred to as the self-similar region, while more substantial differences appear in the shear layer.

5.4.1.1 V Velocities

Figure 5.17 shows an example comparison of the Reynolds number cases for the Standard k-ε model. The differences seen here hold true for all turbulence models and experiments, the only variation being the magnitude and location of differences.

As a qualification of the following, it is important to note that the differences between the Reynolds numbers are very small and that uncertainties in the results may be as likely an explanation for the effects seen here as any physical explanation. Nevertheless a discussion of apparent impacts is conducted throughout the remainder of the section.

For all models, there is a self-similar region in the jet core where the Reynolds number has no effect on normalized velocities. Moving outwards toward the shear layer, the velocities of the lower Reynolds number case appear to decline slightly sooner than the higher Reynolds number, however the higher Reynolds number case exhibits a steeper gradient when it does begin to decline, with normalized velocities dropping below those of the Re = 5 000 case at the centre of the shear layer, approximately x/d = 0.5.

This comparison also allows an inference of the width of the shear layer. As the figure shows, the graphs for the Re = 5 000 case begin to diverge at x/d = 0.15 and do not recombine until x/d = 1.35, however the graphs for the Re = 25 000 case diverge much farther at approximately x/d = 0.30 and combine much sooner at x/d = 0.9, reflecting the smaller shear layer at this distance from the jet source.

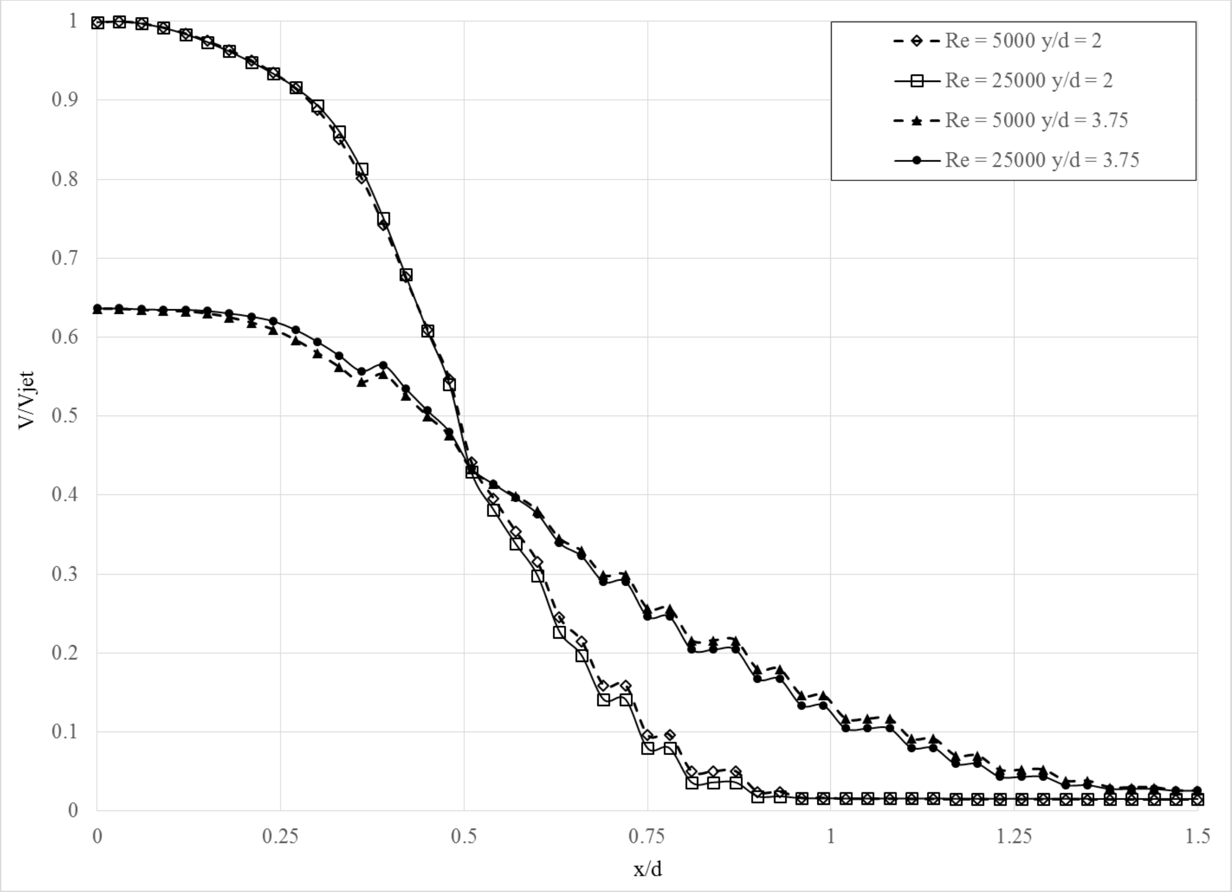

Figure 5.17: Impact of Reynolds Number on V Velocities

Given the similarities of the profiles at different Reynolds numbers, simply performing this comparison of the graphs of the V velocities may not be the clearest way to see the impact of

Reynolds number. Since the main differences caused by varying the Reynolds number occur in the shear layer, a common metric that is useful for comparing these cases is the jet half-width. This describes the x (or x/d) value at which the jet velocity reaches half that of the centreline velocity at a particular distance, giving an indication of the spreading of the jet.

Figure 5.18 seems to indicate that the half-width of the jet may vary with Reynolds number, particularly very near the cylinder, with the larger Reynolds number exhibiting a smaller half-width. This corresponds to a steeper gradient in the shear layer. This also illustrated some of the differences in turbulence models, with the *k-ω* model exhibiting the largest difference due to Reynolds number changes, while the Standard *k-ε* model results in the most spreading near the jet.

The apparent differences in the shear layer predictions for different Reynolds numbers are present for all turbulence models used. This seems to suggest that while the Reynolds number has minimal impact on the centreline velocity decay profile, the turbulent layer surrounding the jet core may be affected.

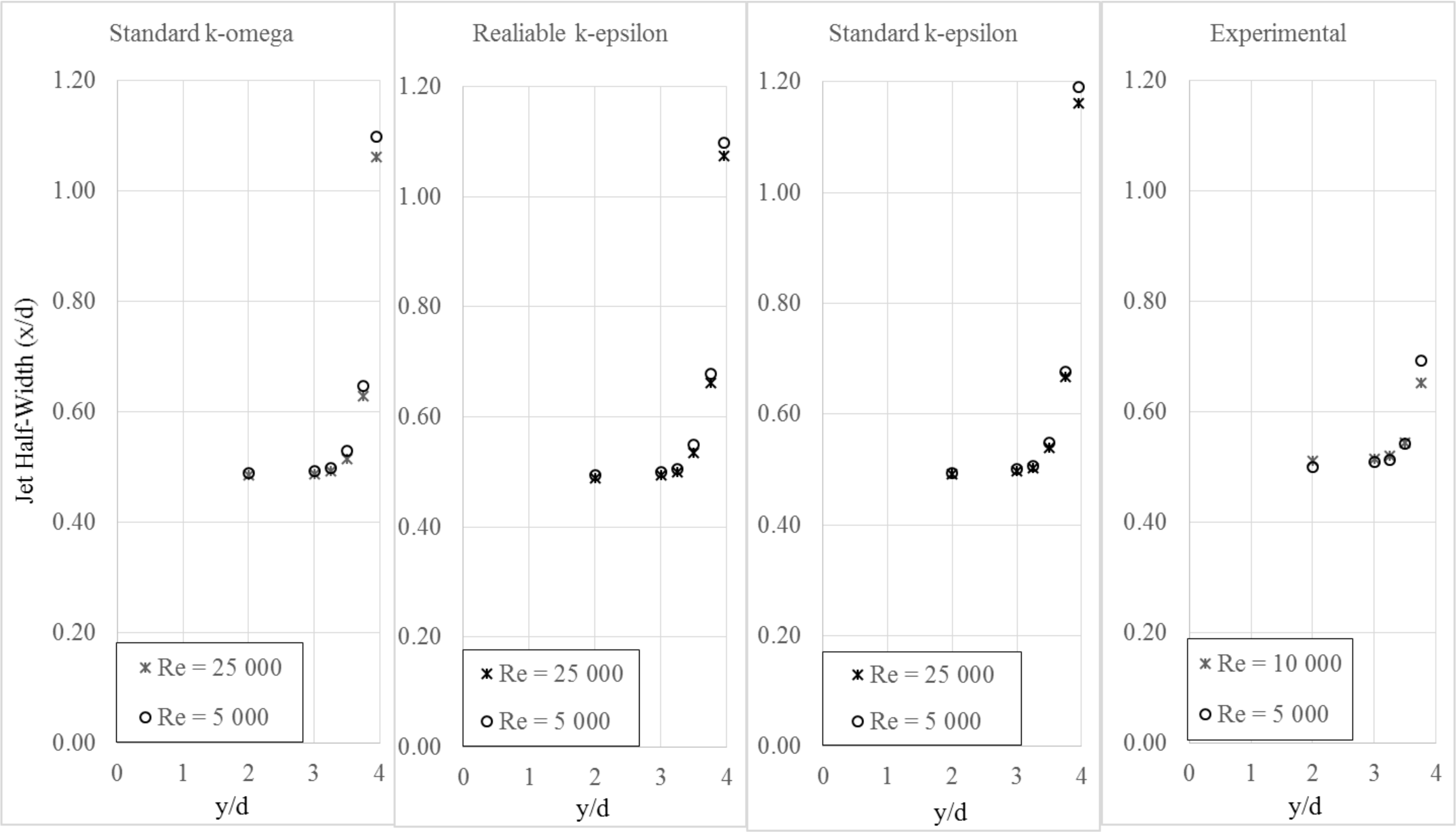

Figure 5.18: Impact of Reynolds Number on Jet Half-Width

5.4.1.2 U Velocities

When observing the effect of Reynolds number on the velocities perpendicular to the jet axis, again it is primarily of use to focus on the y/d = 3.75 case. Unfortunately there is no metric analogous to half-width that can assist in assessing the differences in U velocities. It must therefore be sufficient to observe the differences in the normalized u-velocities themselves.

A similar pattern is seen in the wall jet simulation results as appears in the impinging jet. The normalized velocities in the core region are the same for each Reynolds case until the shear layer begins, at which point the normalized velocities in the higher Re case begin to exceed those of the lower Re cases, reaching a slightly higher peak before exhibiting a steep decline, at which point the normalized velocities in the lower Reynolds number cases exceed the higher Re cases until the momentum dissipates. Figure 5.19 shows the realizable *k*-*ε* results which provide the clearest illustration of these differences.

The experimental results in Figure 5.20 appear to show a similar effect of Reynolds number on the U velocities that was seen in the simulation. As with the V velocities, any impact is largely confined to the shear layer, with minimal impact to the jet core. Again due to the magnitude of the differences, it is difficult to assert that these discrepancies are truly meaningful.

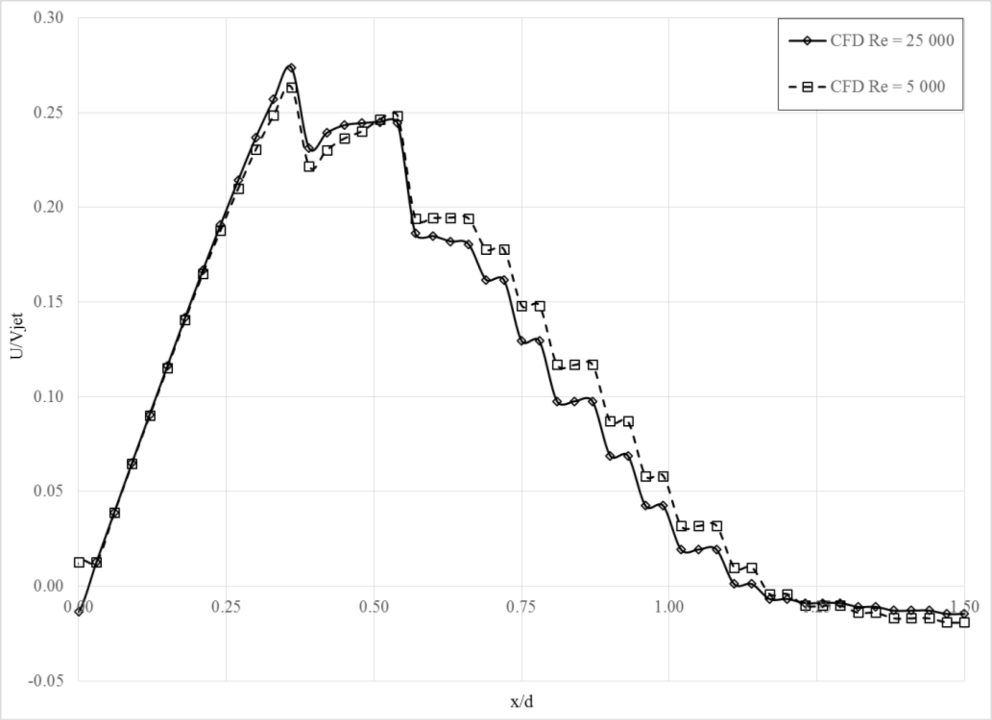

Figure 5.19: Impact of Reynolds Number on U Velocities (Realizable *k-ε*, y/d = 3.75)

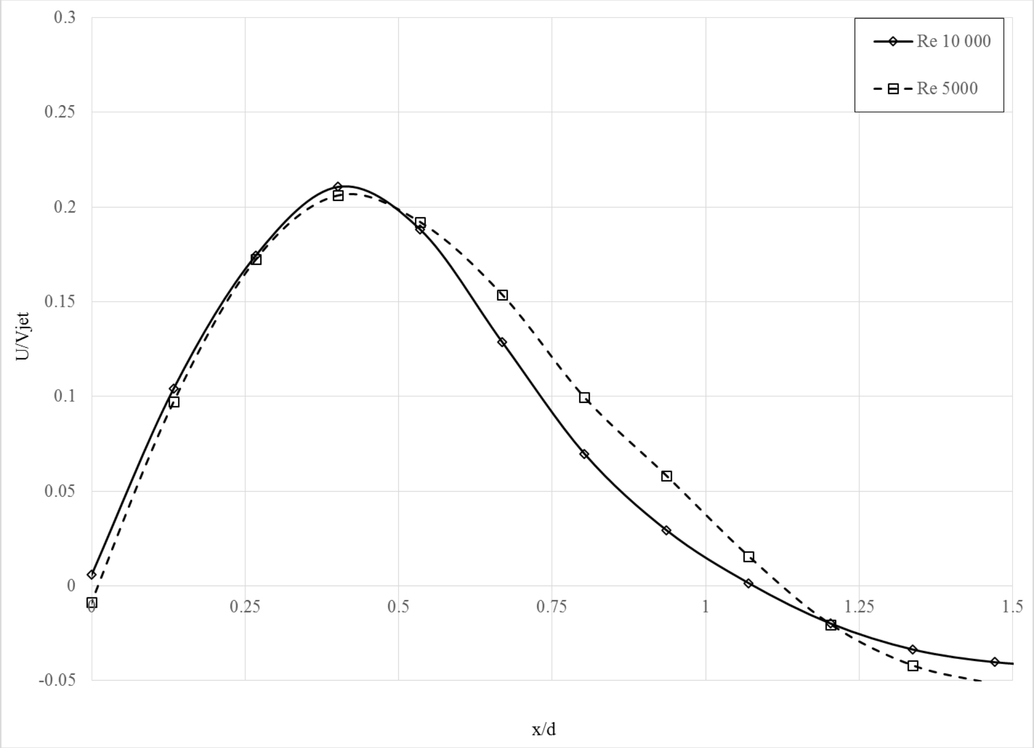

Figure 5.20: Impact of Reynolds Number on U velocities (Experimental Data, y/d = 3.75)

5.4.2 Turbulence

Clearly the turbulence kinetic energy in the jet will be larger at larger Reynolds number, however when normalized by the square of the jet velocity, the simulations give the result that the TKE is higher at lower Reynolds numbers, both in the core of the jet and the shear layer. Figure 5.21 - Figure 5.22 show the turbulence profiles at y/d = 2 for each turbulence model comparing the results from the different Reynolds numbers. Only one y-coordinate position is shown to ensure the graphs are readable, however the differences between the different Reynolds number jets are similar at all distances.

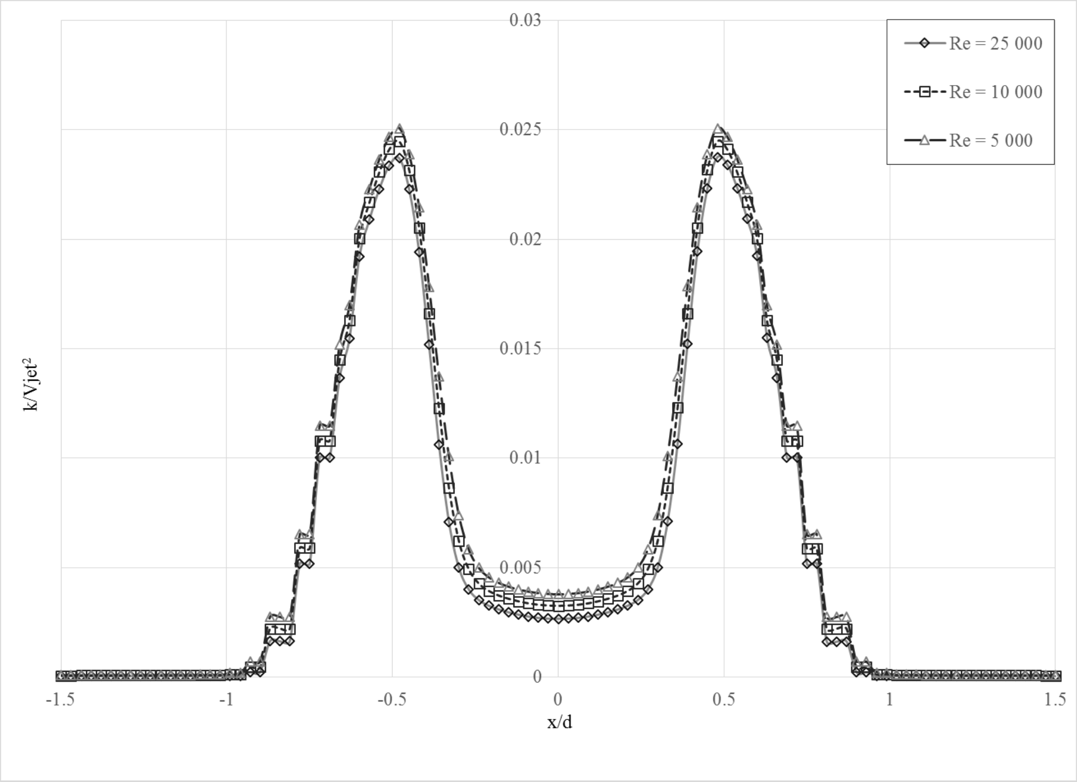

Figure 5.21: Normalized Turbulence Kinetic Energy – Standard k-ε (y/d = 2)

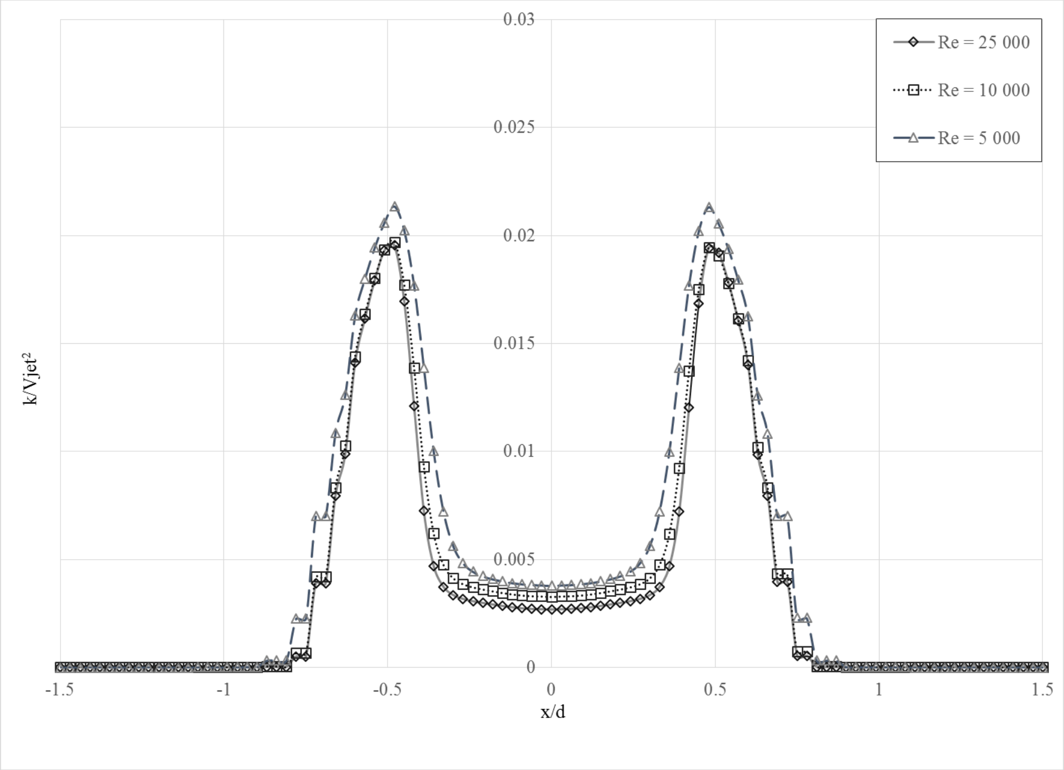

Figure 5.22: Normalized Turbulence Kinetic Energy – Realizable k-ε (y/d = 2)

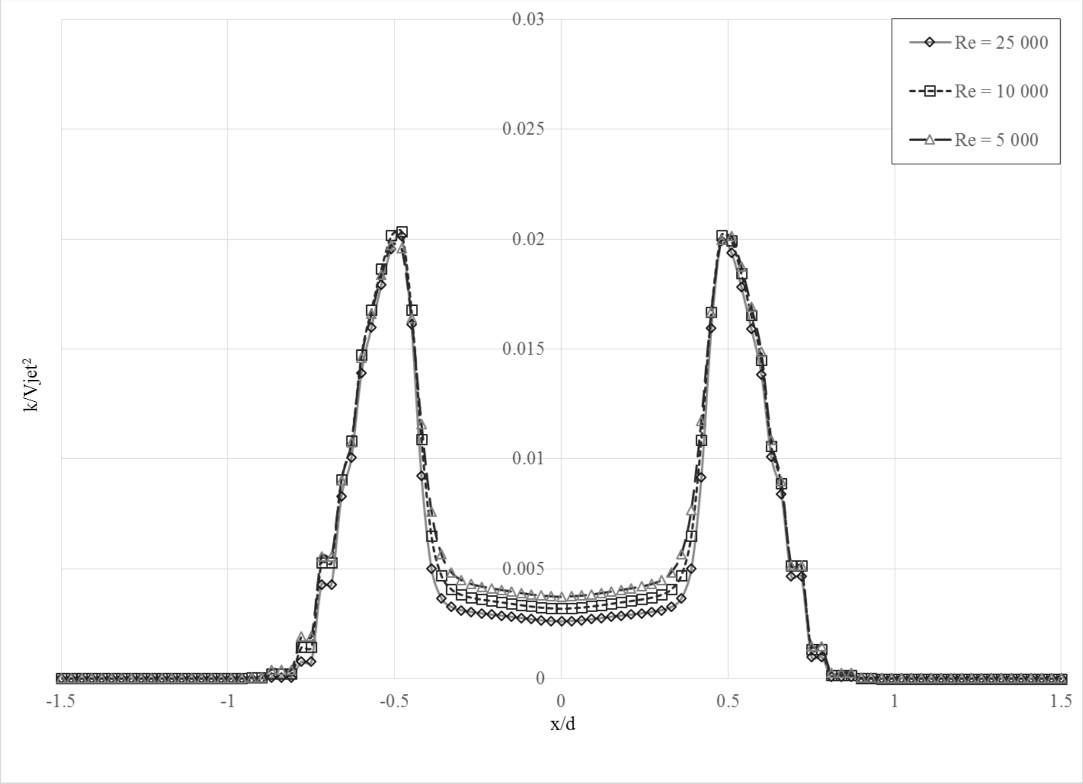

Figure 5.23: Normalized Turbulence Kinetic Energy – Standard k-ω (y/d = 2)

Figure 5.24 shows the experimental turbulence data at y/d = 2 for each Reynolds number. The previously discussed issues with the Re = 25 000 experiments persist so it will be of use to primarily focus on the Re = 5 000 and 10 000 cases. As predicted by the turbulence models, the peaks of the normalized turbulence kinetic energy are higher for the Re = 5 000 case, however in the core region, the TKE for the Re = 5 000 case drops below that of the Re = 10 000 case.

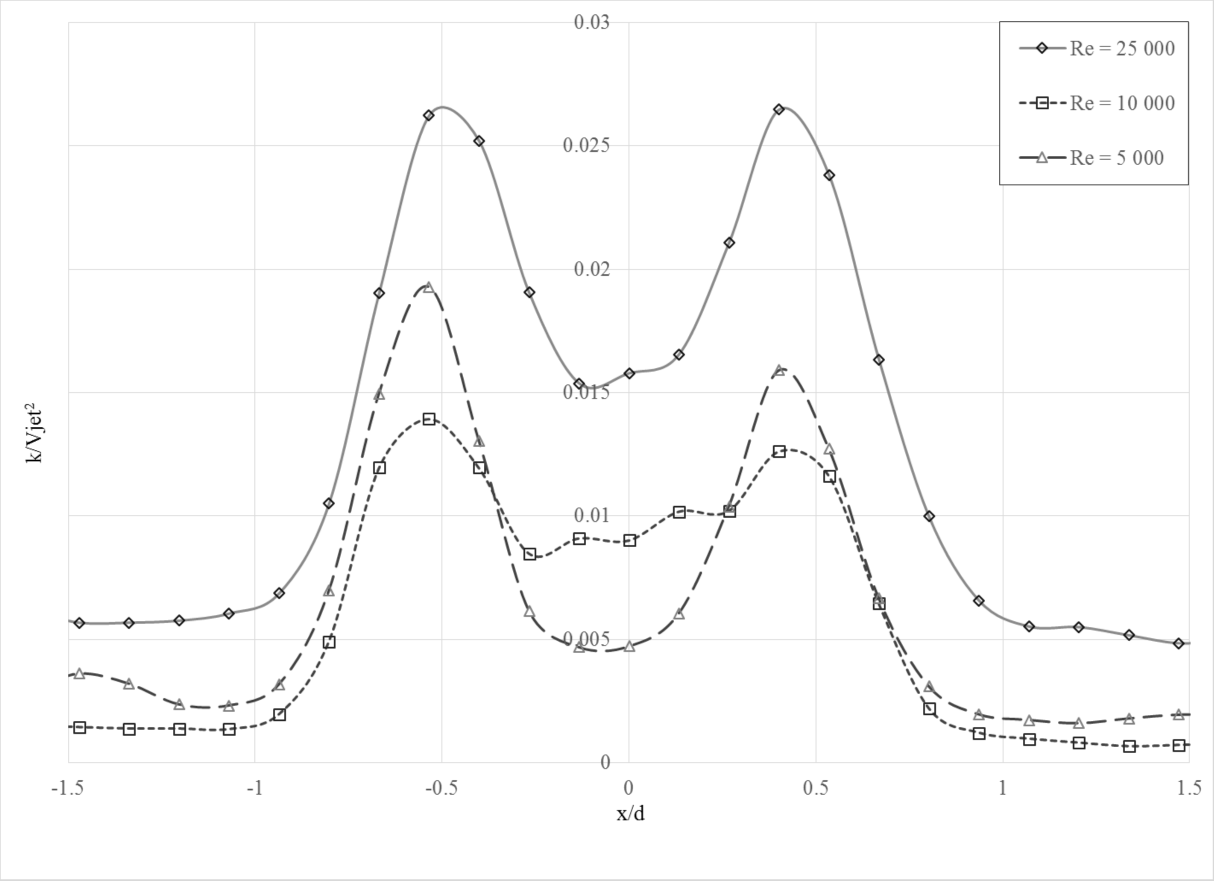

Figure 5.24: Normalized Turbulence Kinetic Energy – Experimental (y/d = 2)

5.5 Buoyancy Effects

As the cylinder is heated, it generates a buoyant force due to the density differences effected in the fluid. This section investigates the impact that this buoyant force has on the jet and seeks to explain any differences seen between the heated and unheated cases.

5.5.1 Jet Velocity

5.5.1.1 V Velocities

In the majority of the tests, the heat appeared to have very little impact on the core jet flow velocities in the experiments. Even in the case of the lower Reynolds number tests, the impact of the buoyant force from the heater in the limits of power levels applied shows a minimal difference in normalized centreline jet velocity and, given the uncertainties present in the experiment, it cannot be confidently asserted that the difference is significant.

Despite the minimal impact on the centreline velocity decay, at lower Reynolds numbers, the heated tests seems to show differences in the shape of the jet as it reaches the impingement point, as well as the orthogonal (U) velocities near the heated cylinder. Figure 5.25 shows how jet velocities decline from the centre of the jet to the surrounding fluid. There appears to be a difference seen in the slopes of the fit lines, suggesting that despite the similar centreline velocities, the heated tests may exhibit a steeper gradient in velocities in the surrounding shear layer, however confidence in the true nature of this effect is limited.

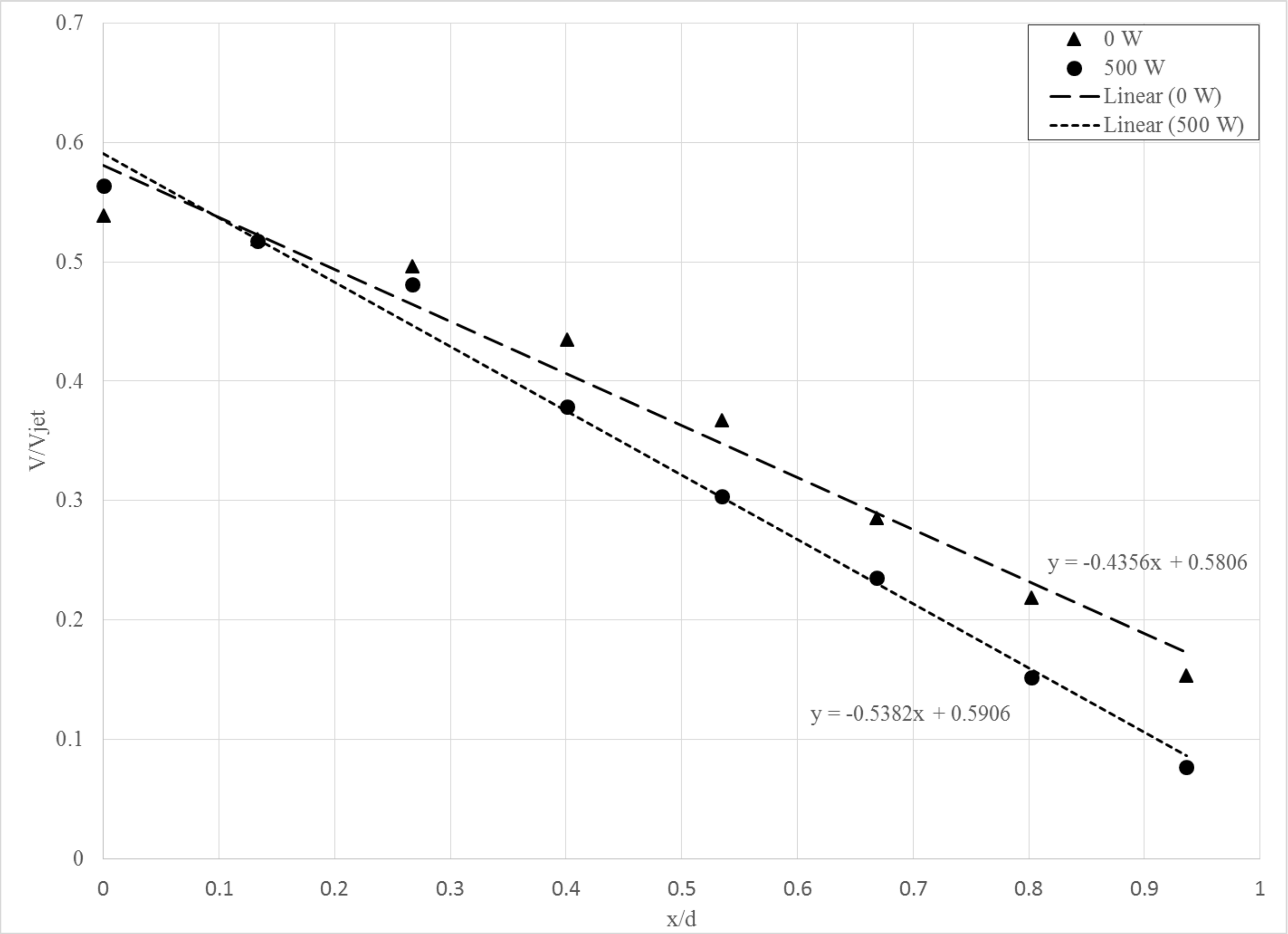

Figure 5.25: Jet Velocity Decay across Jet (Re = 5000, y/d = 3.75)

Figure 5.26 provides a look at the impact of heating on the decay of the jet centreline velocity. While slight discrepancies between the heated and unheated case as the jet approaches the cylinder, it cannot be asserted that these are significant. This chart indicates that the effect of the heating on the centreline of the jet is negligible and any potential effects of heating must therefore occur outside of the jet core.

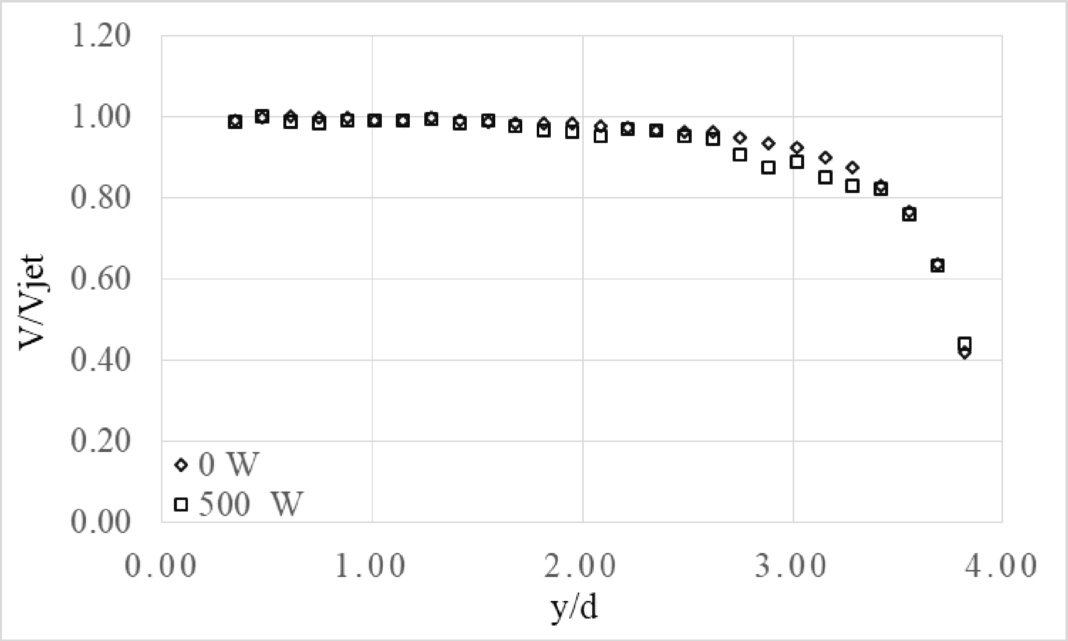

Figure 5.26: Comparison of Heated and Unheated Centreline Velocity Profiles (Re = 5 000)

As with the discussion on Reynolds number impact, there also appears to be some difference between the heated and unheated cases seen in the jet half-width profiles. Figure 5.27 shows the average jet half-width profiles for the heated and unheated cases for Re = 5 000. The half-width for the heated case is smaller than that of the unheated case, suggesting there may be an impact on the dissipation of jet velocity in the shear layer, although uncertainties in the experiments make it difficult to draw firm conclusions about the behaviour.

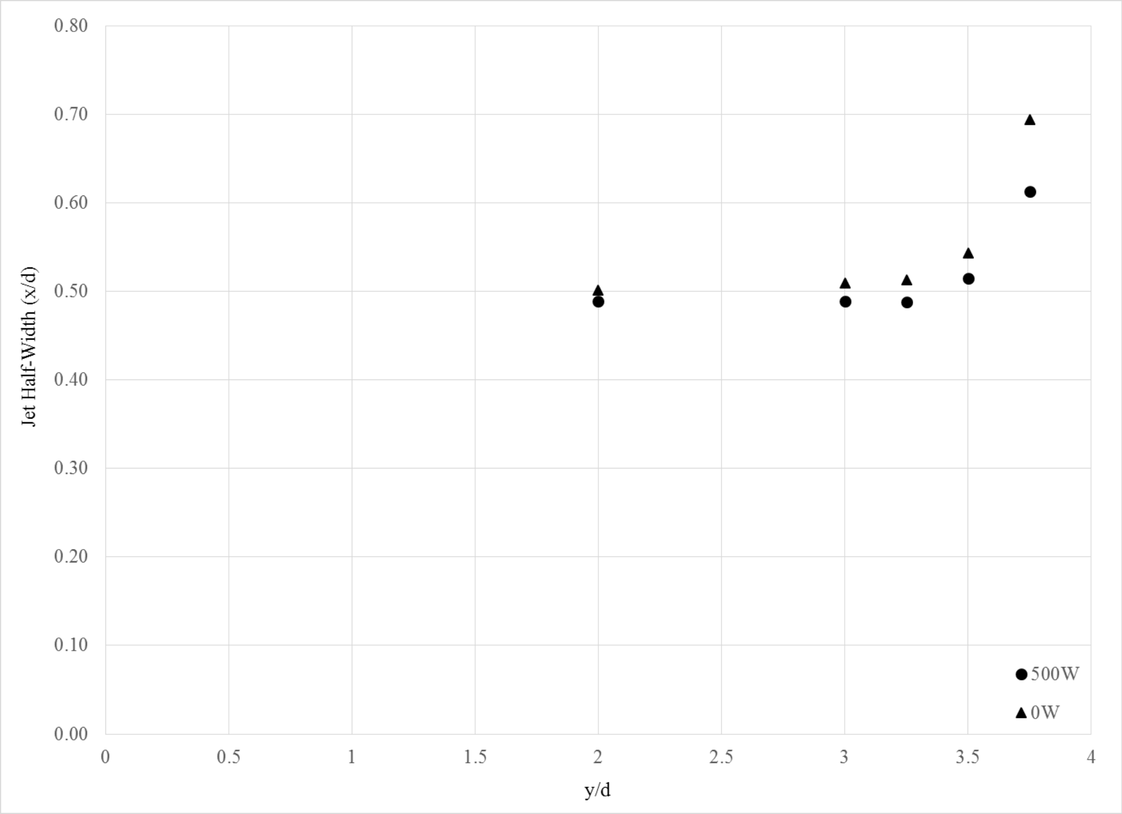

Figure 5.27: Jet Half-Width Profiles (Re = 5000, y/d = 3.75)

5.5.1.2 U Velocities

Figure 5.28 shows the velocities orthogonal to the jet axis for the heated and unheated experiments – as the results are reasonably symmetric, only one side of the jet is shown for simplicity. As with the axial velocities, these are normalized to the maximum jet centreline velocity to remove the impact of discrepancies in jet momentum and to compare the effect of Reynolds number on the profiles. In the Re = 5000 case, substantial differences can be seen in the velocity peaks at y/d = 3.75. The velocities for the unheated case are greater than those for the unheated case by approximately 20% at the peaks. One possible explanation for this effect is that the heating of the cylinder decreases the viscosity of the water near the cylinder, allowing the water to flow more easily around the cylinder rather than being diverted laterally.

The difference in the velocity peaks perpendicular to the jet becomes negligible at higher Reynolds numbers as can be seen in Figure 5.29. This is most likely due to the momentum of the jet and the influence on the surrounding layers dominating any buoyant forces or viscosity impacts arising from the heated cylinder.

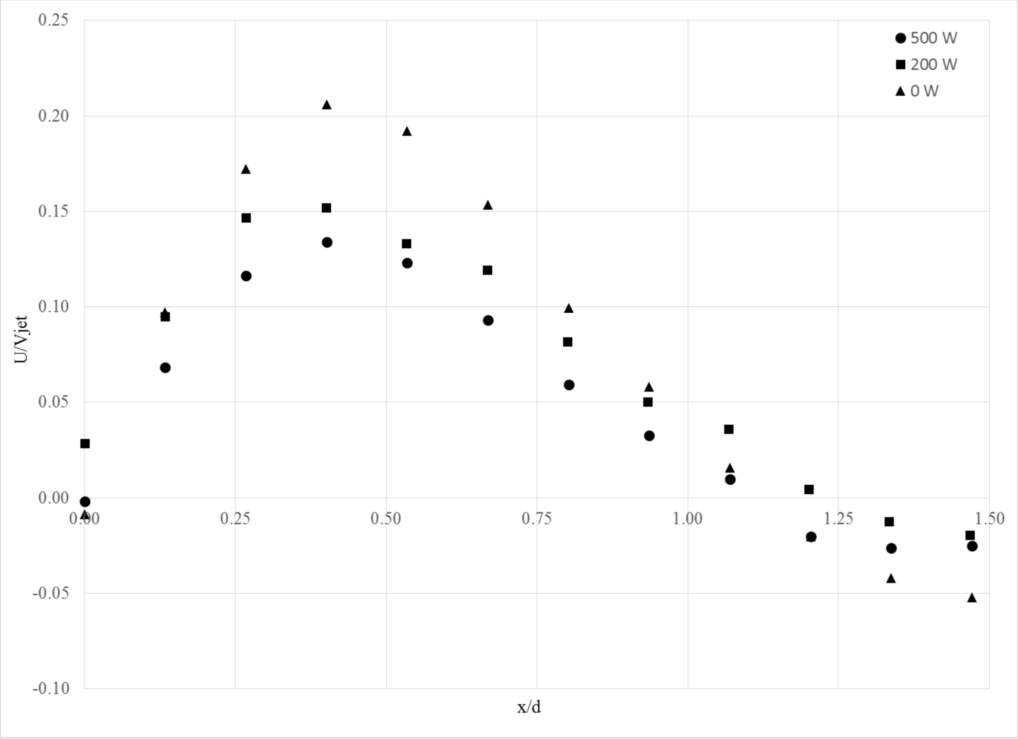

Figure 5.28: Effect of Heating on U Velocities (Re = 5000, y/d = 3.75)

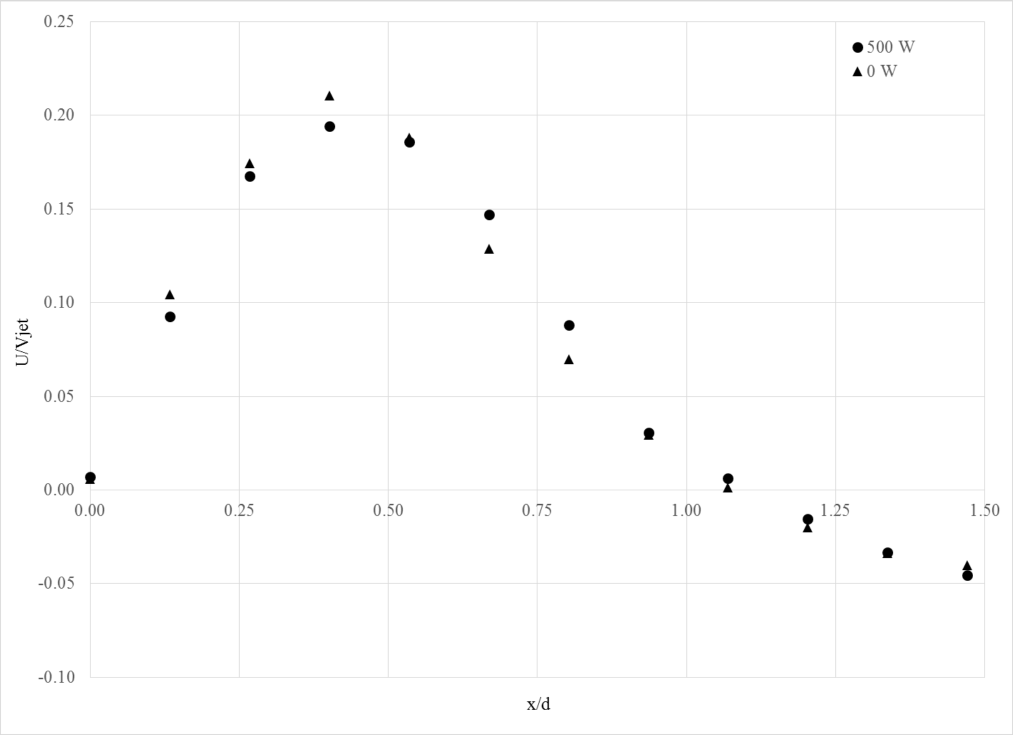

Figure 5.29: Effect of Heating on U Velocities (Re = 10 000, y/d = 3.75)

5.5.2 Turbulence

For the lower Reynolds number cases (Re = 5 000 and 10 000), the buoyant force provided by the heated cylinder appeared to increase the turbulence kinetic energy in the jet as seen in Figure 5.30: Turbulence Profile for Heated Test (Re = 5 000, 500 W)Figure 5.30 and Figure 5.31. However as the results from the simulation indicate negligible effect of heating on the turbulence kinetic energy, in addition to the fact that there appears to be minimal impact on the flow, the large differences seen in the experimental results are most likely artifacts of the heating of the flow affecting the PIV measurements rather than true changes in TKE.

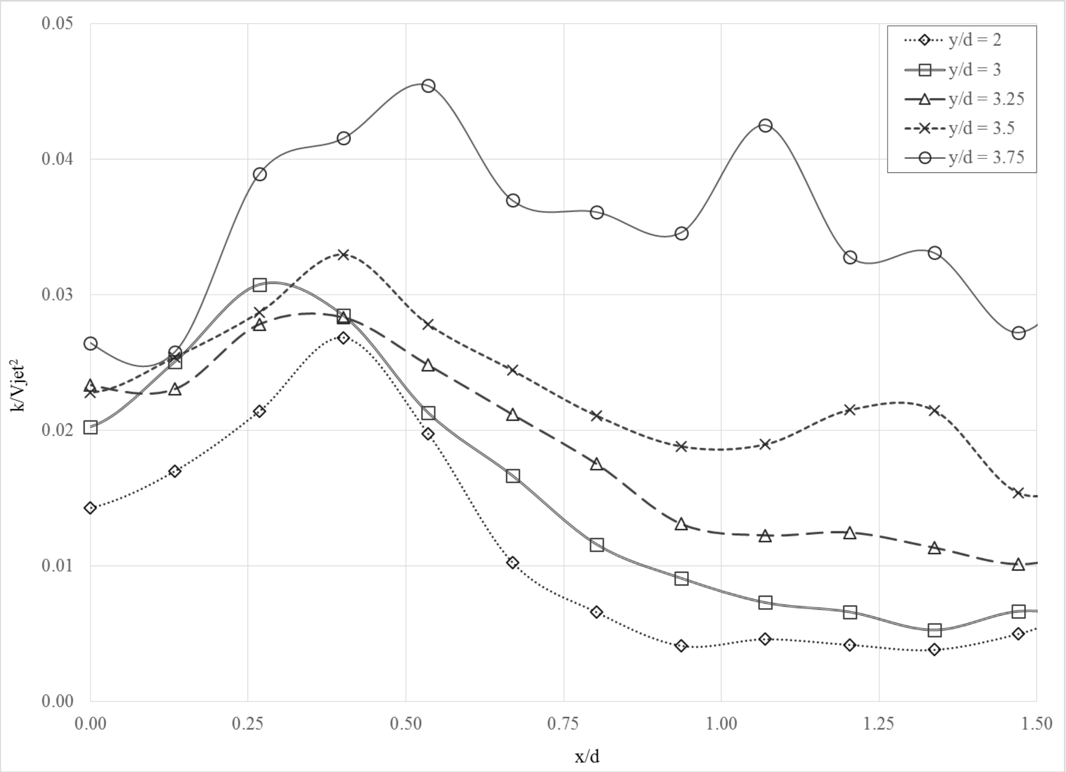

Figure 5.30: Turbulence Profile for Heated Test (Re = 5 000, 500 W)

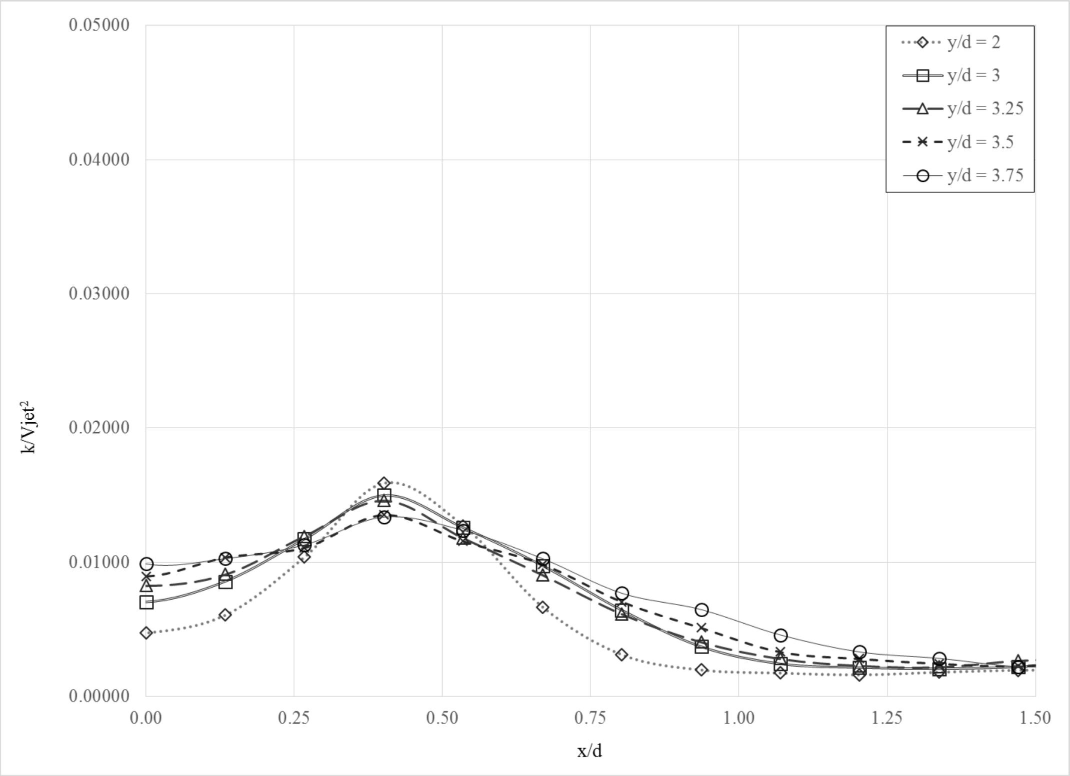

Figure 5.31: Turbulence Profile for Unheated Test (Re = 5 000, Zero Power)

5.5.3 Heated CFD

Simulations were also performed to investigate the impact of the heating on the cylinder. Figure 5.32 shows the effect that the buoyant forces generated by the heated cylinder have on the half width for the selected model. Although the differences are slight for the standard *k-ε* and standard *k-ω,* the difference exhibited in the simulation results matches that of the experiment in that the half widths are smaller for the heated runs. As with the experimental results, any differences in the higher Reynolds number cases were not significant.

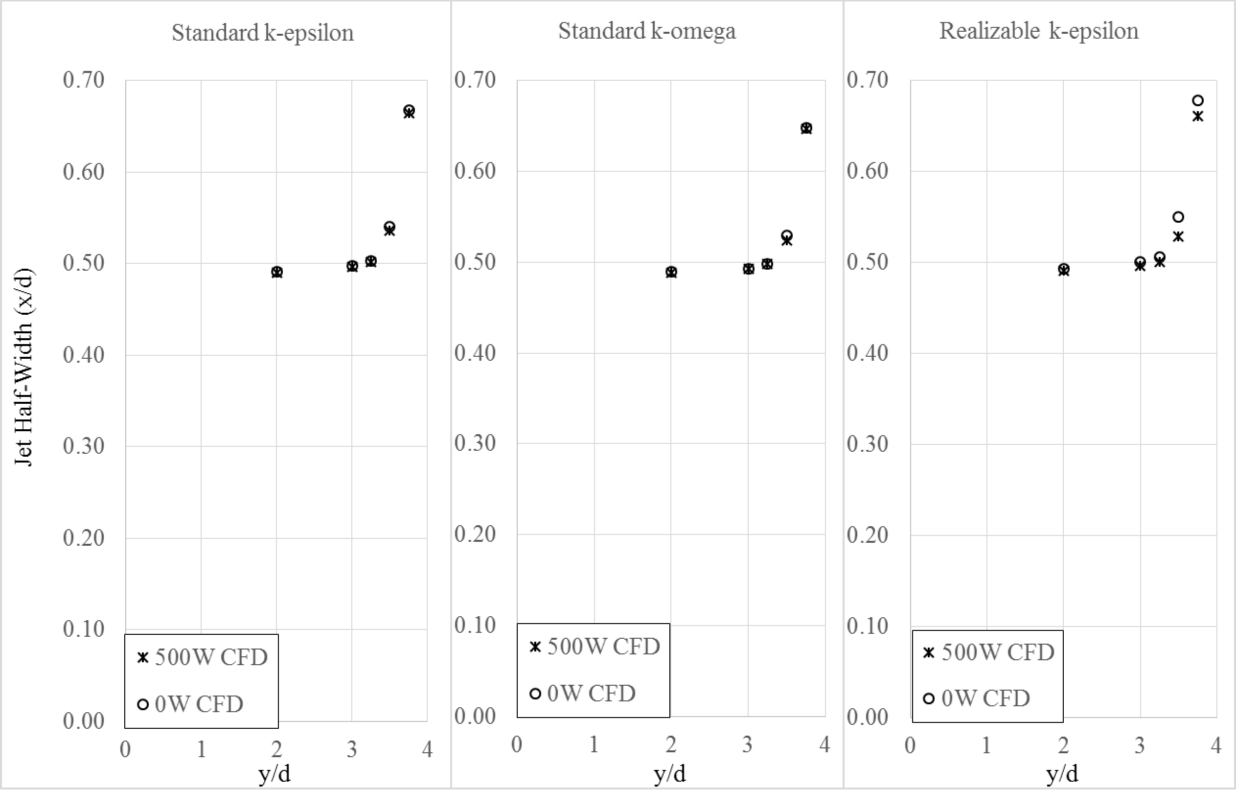

Figure 5.32: Comparison of Heated and Unheated Jet Half-Width

One unexpected result seen in the heated CFD was that the turbulence kinetic energy displayed an asymmetry, with a peak on the left side of the cylinder up to 10% higher than the peak on the right side. This may be due to the fact that the RANS models used were attempting to find a steady solution for mixed convection effects which are inherently unsteady. Regardless of the asymmetry, when taken as an average of both sides, the TKE for the heated simulations appears to exceed that of the unheated simulations in the shear layer, although given the uncertainty, it is difficult to assert this is a significant result.

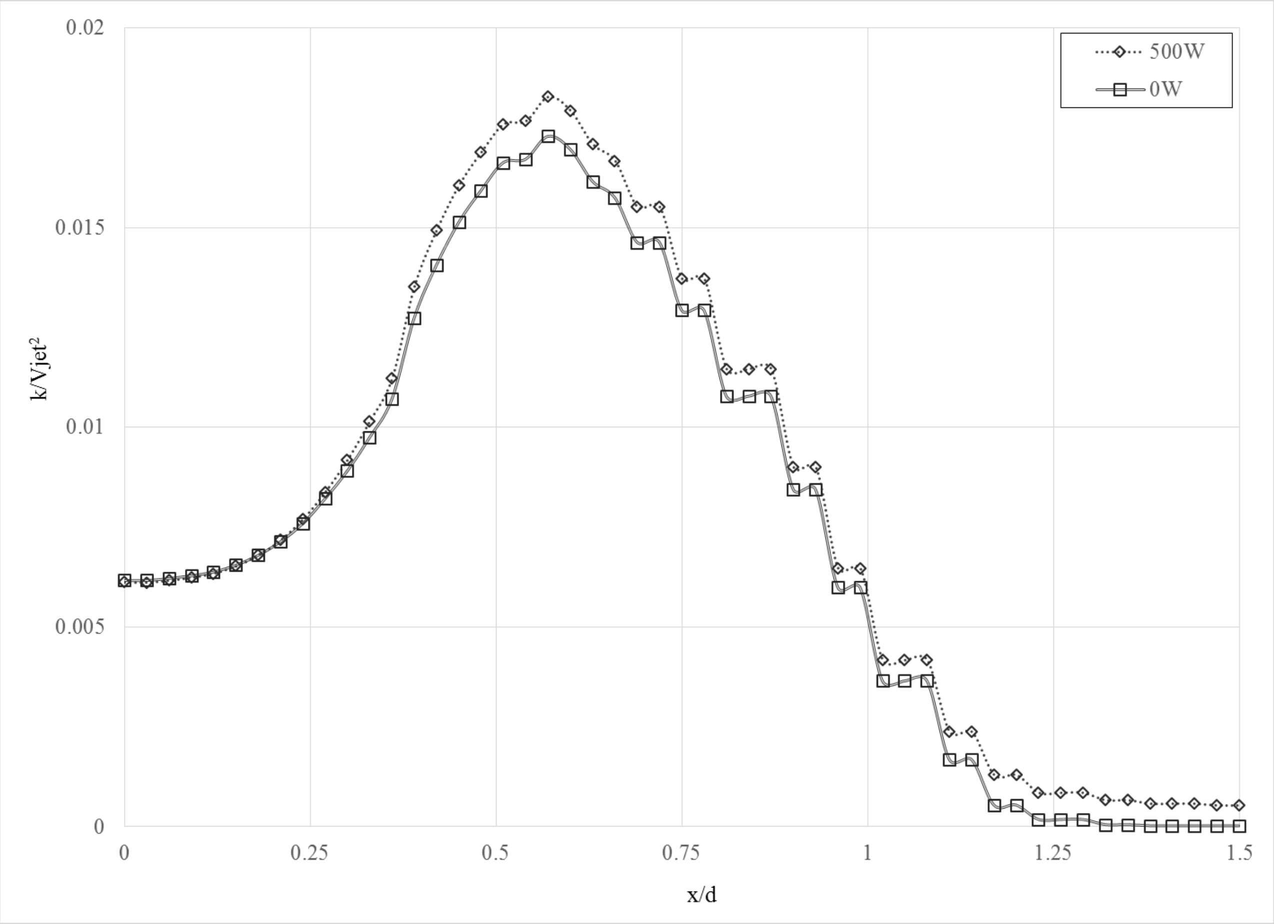

Figure 5.33: Heating Comparison of Average Normalized TKE Profile (Realizable k-e, y/d = 3.75)

Overall the impact of heating on the cylinder is clear, the results from both the experiment and the simulations show that the buoyant forces generated by the heated cylinder do not influence the core of the jet in any meaningful way, however their impact on the outer edges of the jet causes a steeper gradient and greater turbulence kinetic energy in the shear layer for the lower Reynold number cases.

6 CONCLUSION

A series of experiments and simulations were performed to investigate the behaviour of a turbulent jet impinging a cylinder – both heated and unheated. The experimental data was compared to the simulation to assess the performance of various turbulence models. In addition, the heated and unheated results were compared to determine the impact of the buoyant force generated by the heater on the jet flow.

When compared with the experimental data, the turbulence models performed reasonably well. Of the models investigated, the Standard k-ε model was most accurate in predicting both the velocity magnitudes and the shape of the profile as the jet impinges the cylinder, although it does under-predict the velocities very near the cylinder for the Re = 5 000 case. The turbulence model that was found to be the least accurate for the scenario was the Standard k-ω model, although it did perform quite well in the initial mixing region of the jet.

While the inertial forces dominate the flow as the jet impinges on the cylinder for the range of experimental conditions considered in the present study, the results presented show appreciable differences in velocities orthogonal to the jet for the lower Reynolds numbers between impingement onto the heated and unheated cylinders. The velocities orthogonal to the jet near the impingement zone are notably smaller in magnitude for the heated case than the unheated case. In addition, the jet half-width profiles may suggest that jet velocities drop off more quickly from the jet centre for the heated case.

In combination, these variations suggest that although the heating of the cylinder has a negligible impact on the centreline velocity of the jet, the buoyant forces may affect the shear layer near the cylinder and the viscosity of the fluid surrounding the heater, impacting the shape of the jet as it impinges and, as a result, the deflection of flow near the impingement region. In the context of the larger project to which this research is connected, this difference will have an impact on the overall flow patterns present in the moderator. The lower lateral velocities in the heated case may affect the heat transfer from surrounding heaters in the array.

6.1 Recommendations for Future Work

With this separate effect test complete, the next step is to see the effect of heating on flow patterns in the entire array of tubes in the CANDU moderator. This experiment has been constructed and testing is currently underway to investigate these phenomena.

Some other area of interest that may be less germane to the moderator flow or cooling problems, but nevertheless are of related interest to the research in this thesis would be to investigate impingement of a heated cylinder at lower Reynolds numbers. Of particular interest would be a case in which the buoyant forces produced by the heater are equivalent to those of the impinging jet.

7 References

Angioletti, M., Di Tommaso, R. M., Nino, E., & Ruocco, G. (2003). Simultaneous visualization of flow field and evaluation of local heat transfer by transitional impinging jets. *International Journal of Heat and Mass Transfer 46*, 1703-1713.

ANSYS, Inc. . (2013). *ANSYS Fluent User's Guide, Release 15.0.* Canonsburg, PA: SAS IP.

Badr, H. M. (1984). Laminar combined convection from a horizontal cylinder - parallel and contra flow regimes. *International Journal of Heat and Mass Transfer 27*, 15-27.

Ball, C. G., Fellouah, H., & Pollard, A. (2012). The flow field in turbulent round free jets. *Progress in Aerospace Sceiences 50*, 1-26.

Benedict, L. H., & Gould, R. D. (1996). Towards better uncertainty estimates for turbulence statistics. *Experiments in fluids, 22(2)*, 129-136.

Bereznai, G. (2005). *Nuclear Power Plant Systems and Operation.* CANDU.

Celik, I. B. (1999). *Introductory Turbulence Modelling.* Western Virginia University.

Chien, K. Y. (1982). Predictions of Channel and Boundary Layer Flows with a Low-Reynolds-Number turbulence model. *AIAA journal 20(1)*, 33-38.

Cooper, D., Jackson, D. C., Launder, B. E., & Liao, G. X. (1993). Impinging jet studies for surbulence model assessment - I. Flow-field experiments. *International Journal of Heat and Mass Transfer 36(10)*, 2675-2684.

Cornaro, C., Fleischer, A. S., & Goldstein, R. J. (1999). Flow visualization of a round jet impinging on cylindrical surfaces. *Experimental Thermal and Fluid Sciences, 20*, 66-78.

Craft, T. J., Graham, L. W., & Launder, B. E. (1993). Impinging jet studies for turbulence model assessment - II. An examination of the performance of four turbulence models. *International Journal of Heat and Mass Transfer, 36(10),* 2685-2697.

Dirita, C., De Bonis, M. V., & Ruocco, G. (2007). Analysis of food cooling by jet impingement, including inherent conduction. *Journal of Food Engineering, 81(1)*, 12-20.

Esirgemez, E., Newby, J. W., Nott, C., Ölçmen, S. M., & Ötügen, V. (2007). Expirimental study of a round jet impinging on a convex cylinder. *Measurement Science and Technology, 18*, 1800-1810.

Fand, R. M., & Keswani, K. K. (1973). Combined natural and forced convection heat transfer from horizontal cylinders to water. *International Journal of Heat and Mass Transfer, 16*, 1175-1191.

Fekklouah, H., Ball, C. G., & Pollard, A. (2009). Reynolds number effects within the development region of a turbulent round free jet. *International Journal of Heat and Mass Transfer, 52(17)*, 3943-3954.

Gandikota, G., Amiroudine, S., Chatterjee, D., & Biswas, G. (2010). The effect of aiding/opposing buoyancy on two-dimensional laminar flow across a circular cylinder. *Numerical Heat Transfer, Part A: Applications, 58(5),* 385-402.

Georgiadis, N. J., & Yoder, D. A. (2006). Evaluation of Two-Equation Turbulence Models for Jet Flow Predictions. *AIAA journal 44(12)*, 3107-3114.

Gillespie, G. E. (1981). An experimental investigation of heat transfer from a reactor fuel channel to surrounding water. *Second Annual CNS Conference.* Ottawa, Canada.

Gori, F., & Bossi, L. (2003). Optimal slot height in the jet cooling of a circular cylinder. *Applied Thermal Engineering, 23(7)*, 859-870.

Grafsrønningen, S., & Jensen, A. (2012). Simultaneous PIV/LIF measurements of a transitional buoyant plume above a horizontal cylinder. *International Journal of Heat and Mass Transfer 55*, 4195-4206.

Grafsrønningen, S., Reif, B. A., & Jensen, A. (2011). PIV investigation of buoyant plume from natural convection heat transfer above a horizontal heated cylinder. *International Journal of Heat and Mass Transfer*, 4975-4987.

Jambunathan, K., Lai, E., Moss, M. A., & Button, B. L. (1992). A review of heat transfer data for single circular jet impingement. *International Journal of Heat and Fluid Flow 13(2)*, 106-115.

Jewkes, J. W., King, A., & Chung, Y. M. (2011). Large Eddy Simulation of a Steady Circular Jet Issuing into Quiescent Fluid. *Proceedings of the 19th International Congress on Modelling and Simulation*, 12-16.

Kim, H. T., & Chang, S. (2015). Computational Fluid Dynamics analysis of the Canadua Deuterium Uranium Moderator Tests at the Stern Laboratories Inc. *Nuclear Engineering and Technology 47(3),* 284-292.

Kim, M., Yu, S., & Kim, H. (2006). Analyses on fluid flow and heat transfer inside Calandria vessel of CANDU-6 using CFD. *Nuclear Engineering and Design 236*, 1155-1164.

Madni, I. K., & Ahmad, S. Z. (1989). Prediction of turbulent, axisymmetric, dense jets discharged to quiescent ambients. *Mathematical and Computer Modelling 12(3)*, 363-370.

Mi, J., Nathan, G. J., & Nobes, D. S. (2001). Mixing characteristics of axisymmetric free jets from a contoured nozzle, an orifice plate and a pipe. *Journal of Fluids Engineering 123(4)*, 878-883.

Moukalled, F., Mangani, L., & Darwish, M. (2016). *The Finite Volume Method in Computational Fluid Dynamics.* Springer International Publishing.

Olsson, E. M., Ahrne, L. M., & Trägårdh, A. C. (2004). Heat transfer from a slot air jet impinging on a circular cylinder. *Journal of Food Engineering, 63(4)*, 393-401.

Pope, S. B. (1975). A more general effective-viscosity hypothesis. *Journal of Fluid Mechanics*, 331-340.

Pope, S. B. (1978). An explanation of the turbulent round-jet/plane-jet anomaly. *AIAA journal 16(3)*, 279-281.

Singh, D., Premachandran, B., & Kohli, S. (2013a). Experimental and numerical investigation of jet impingement cooling of a circular cylinder. *International Journal of Heat and Mass Transfer, 60*, 672-688.

Singh, D., Premachandran, B., & Kohli, S. (2013b). Numerical simulation of the jet impingment cooling of a circular cylinder. *Numerical Heat Transfer, Part A, 64*, 153-185.

Singh, D., Premachandran, B., & Kohli, S. (2015). Effect of nozzle shape on jet impingement heat transfer from a circular cylinder. *International Journal of Thermal Sciences 96*, 45-69.

Singh, S. K., & Singh, R. P. (2008). Air impingement cooling of cylindrical objects using slot jets. *Food Engineering: Integrated Approaches,* 89-104.

Smith, E. J., Mi, J., Nathan, G. J., & Dally, B. B. (2004). Preliminary examination of a "Round jet initial condition anomaly" for the k-ε turbulence model. *15th Australasian Fluid Mechanics Conference*.

Sparrow, E. M., & Lee, L. (1976). Analysis of mixed convection about a horizontal cylinder. *International Journal of Heat and Mass Transfer 19*, 229-231.

Tanase, A., Szymanski, J., El-Hawary, M., & Delja, A. (2015). Numerical predictions of heat transfer and pressure tube/calandria tube deformation during Calandria-Tube Strain Contact Boiling (CSCB) tests. *7th International Conference on Modelling and Simulation in Nuclear Science and Engineering.* Ottawa, Canada: CNSC.

Tawfek, A. A. (1999). Heat transfer due to a round jet impinging normal to a circular cylinder. *International Journal of Heat and Mass Transfer 35*, 327-333.

Teyssedou, A., Necciari, R., Reggio, M., Zadeh, F. M., & Étienne, S. (2014). Moderator flow simulation around calandria tubes od CANDU-6 nuclear reactors. *Engineering Applications of Computational Fluid Mechanics 8(1)*, 178-192.

Thies, A. T., & Tam, C. K. (1996). Computation of turbulent axisymmetric and nonaxisymmetric jet flows using the k-epsilon model. *AIAA journal 34(2)*, 309-316.

White, F. M. (1999). *Fluid Mechanics, WCB.* Boston: McGraw Hill.

Wilcox, D. C. (1998). *Turbulence Modelling for CFD.* La Canada, CA: DCW Industries.

Xu, G., & Antonia, R. A. (2002). Effect of different initial conditions on a turbulent round free jet. *Experiments in Fluids 33*, 677-683.

Yoon, C., Rhee, B. W., & Min, B. J. (2004). Development and validation of the 3-D computational fluid dynamics model for CANDU-6 moderator temperature predictions. *Nuclear Technology 148(3)*, 259-267.

Appendix A: Experimental Setup

This appendix includes some pictures of the experimental setup to aid in visualization of the experiment.

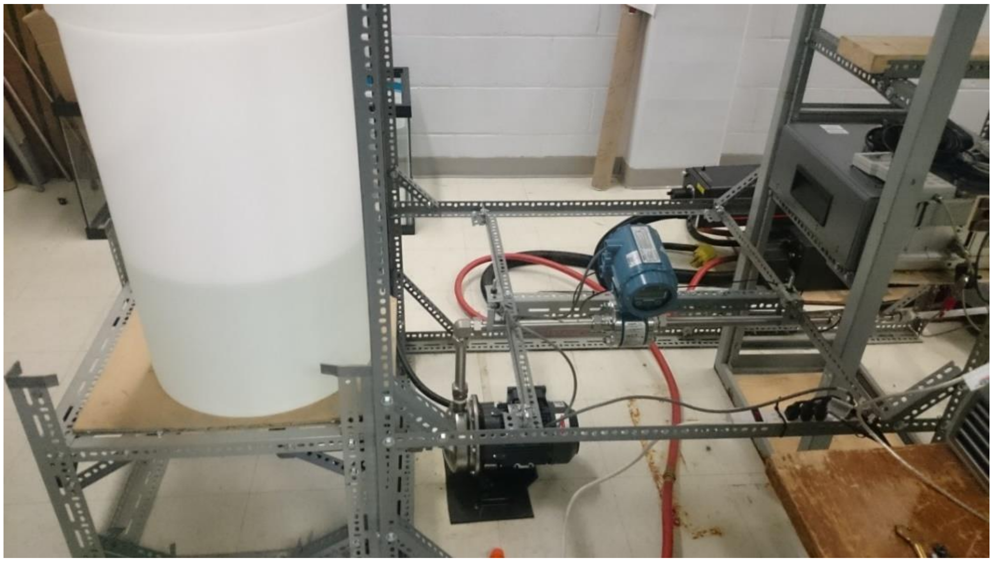

Holdup Tank, Pump, and MAG Flow Meter

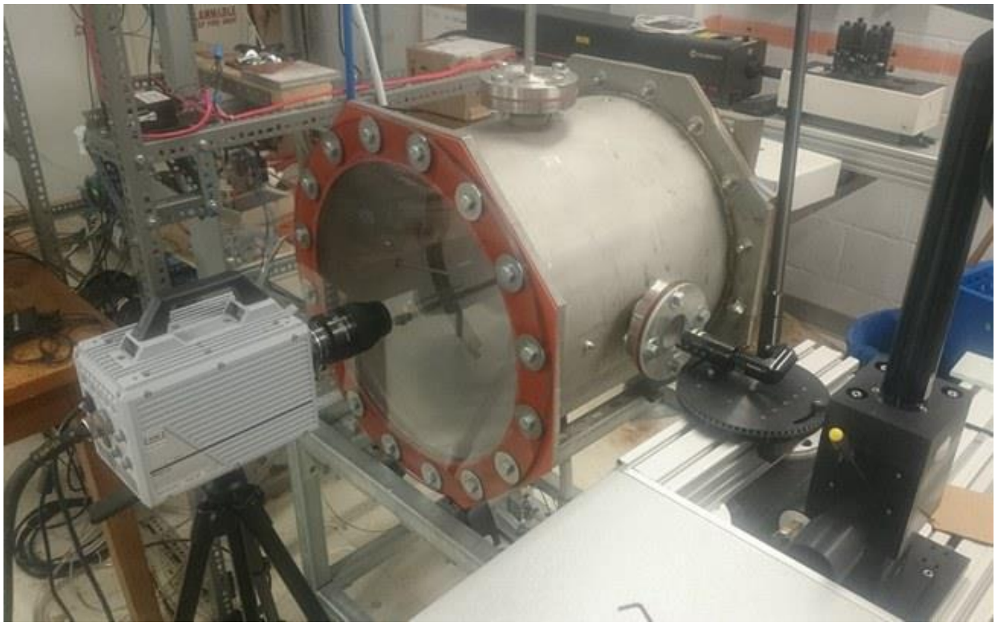

PIV Setup – Laser Light Arm at the Side, Camera in Front

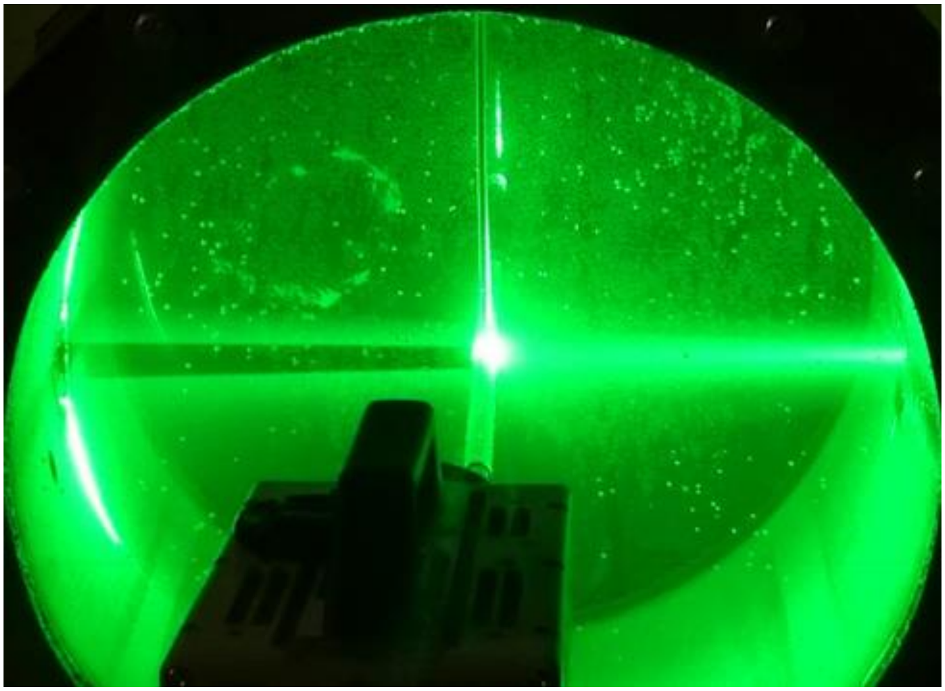

PIV Sheet and Camera

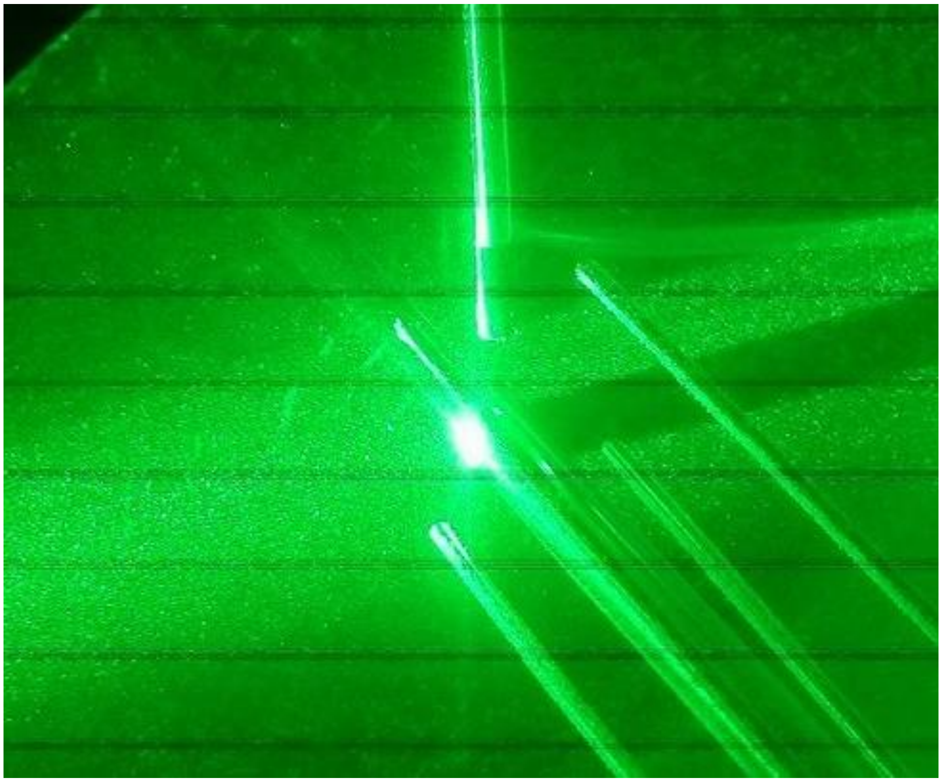

Close-up of Jet and Thermocouples in Light Sheet

Appendix B: Vector Fields

The vector field provided by the simulation and experiment are derived from the velocities calculated or measured respectively. For the purposes of this thesis, these field were not a useful tool for visualising differences given the magnitude of the differences. The field however may be useful for understanding or visualising the discussed results. A sample of the raw vector fields is included in this appendix.

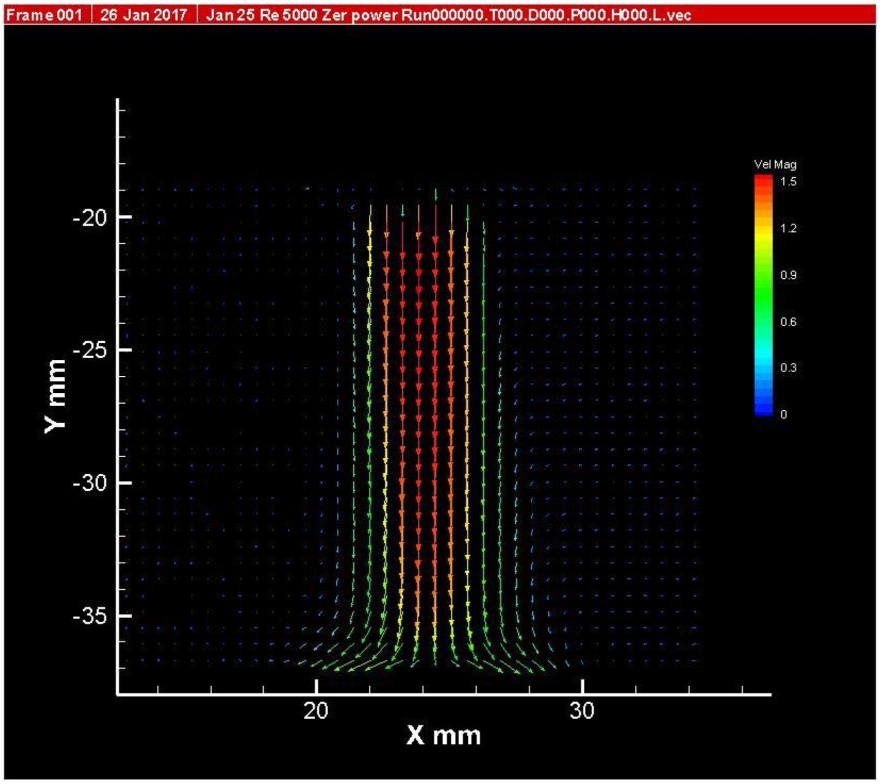

PIV Data, Re = 5 000, 0 W

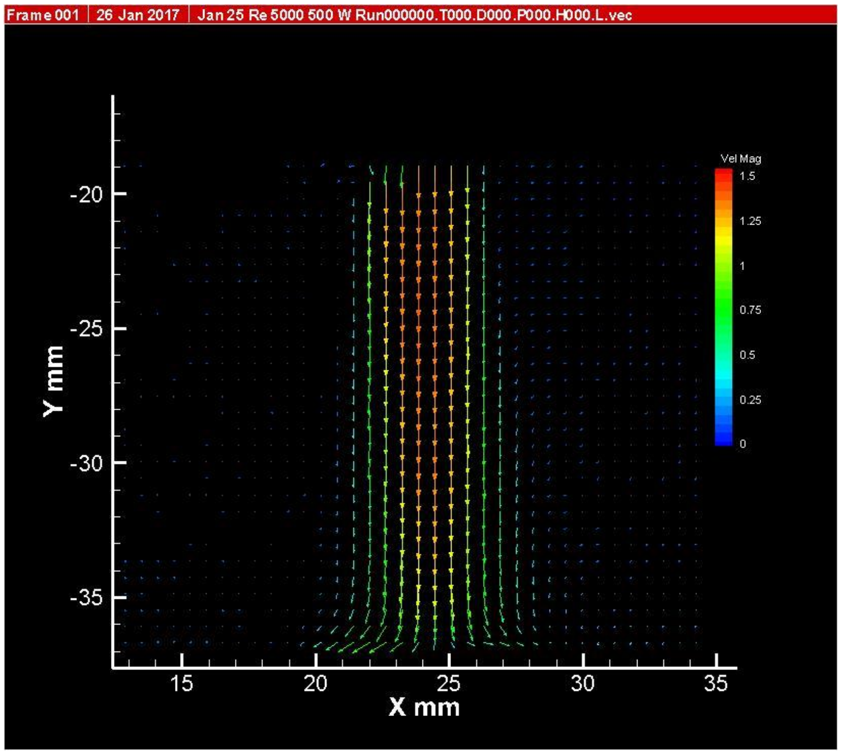

PIV Data, Re = 5 000, 500 W

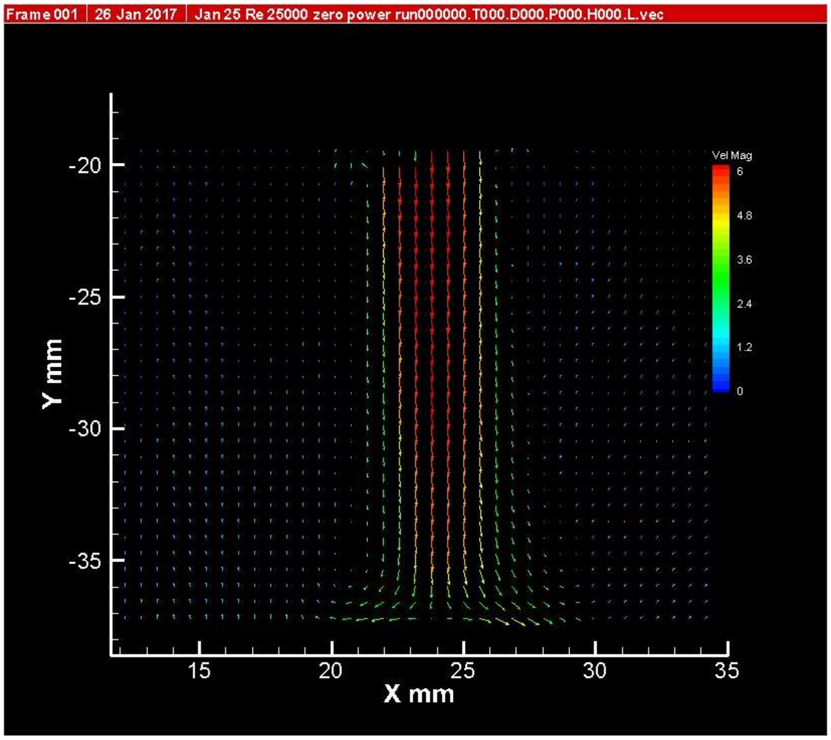

PIV Data, Re = 25 000, 0 W

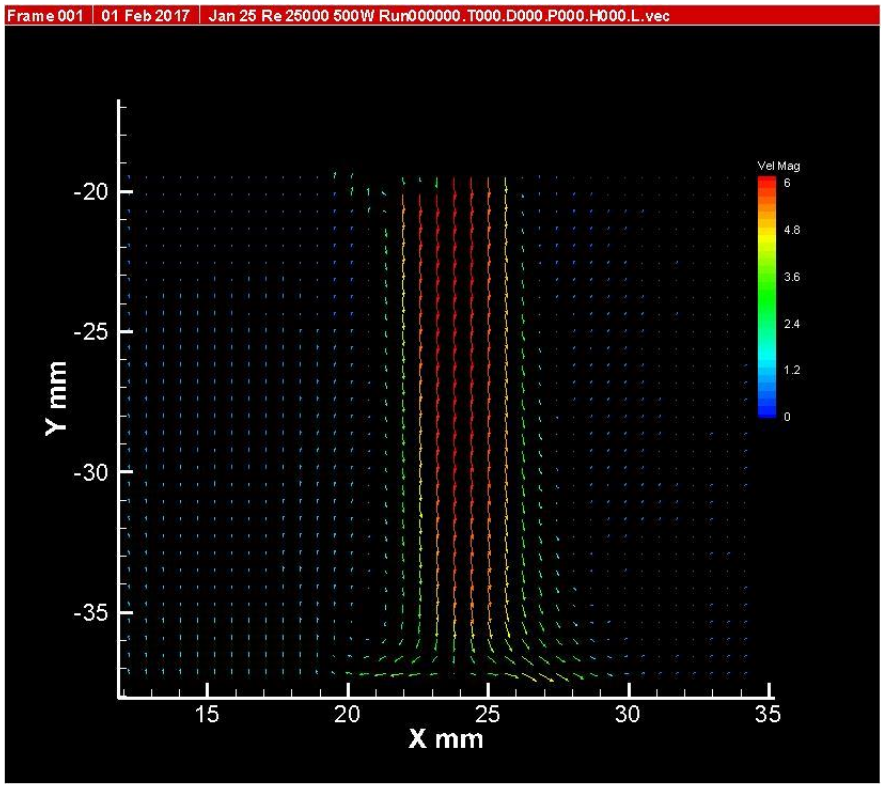

PIV Data, Re = 25 000, 500 W

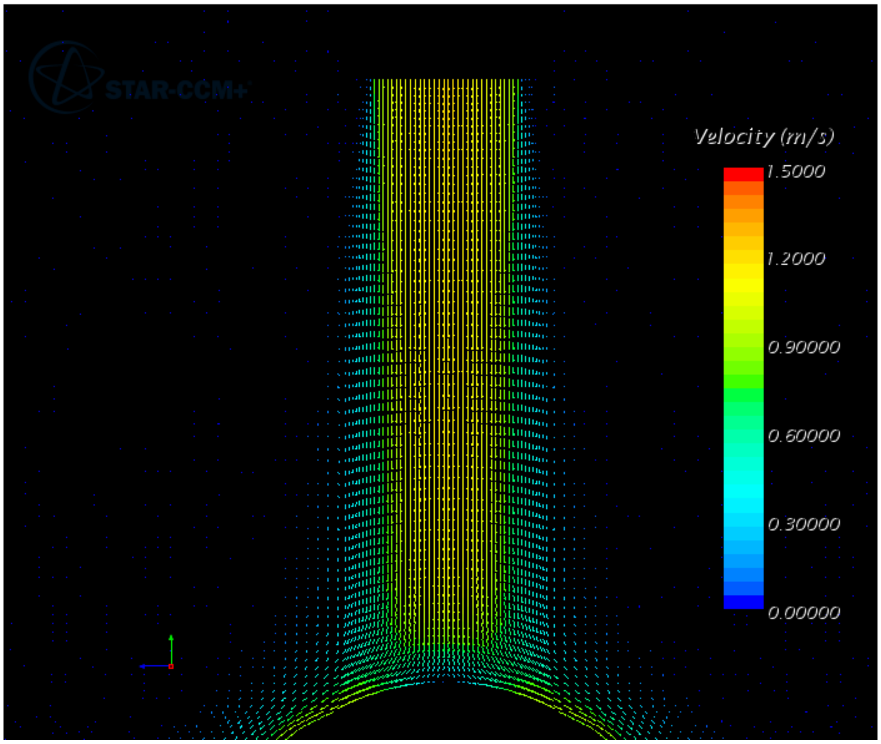

CFD Data, Re = 5 000, Standard *k*-*ε*

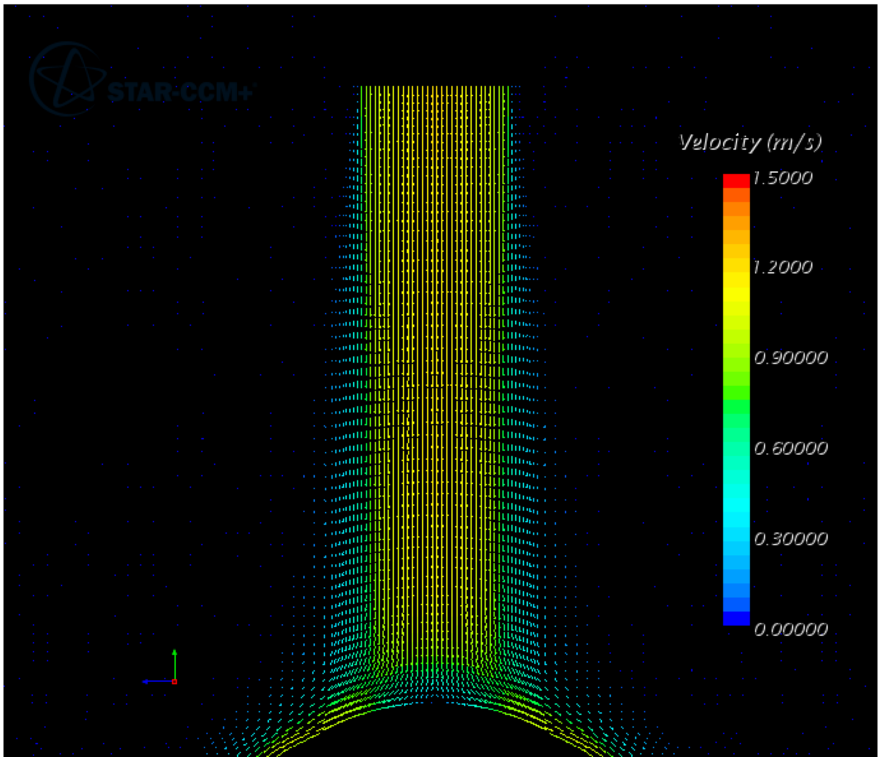

CFD Data, Re = 5 000, Standard *k-ω*

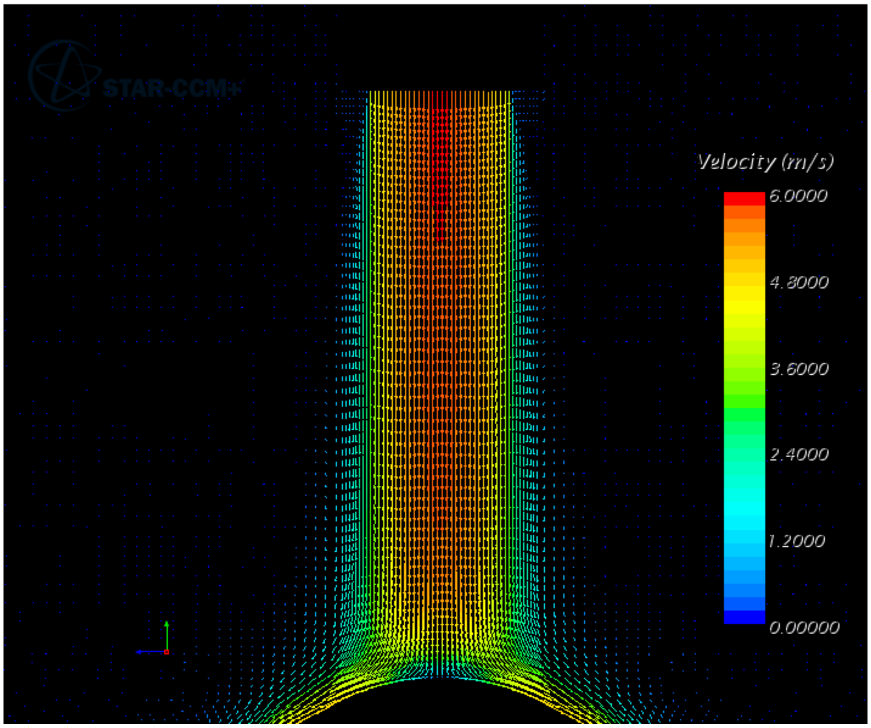

CFD Data, Re = 25 000, Standard *k-ε*

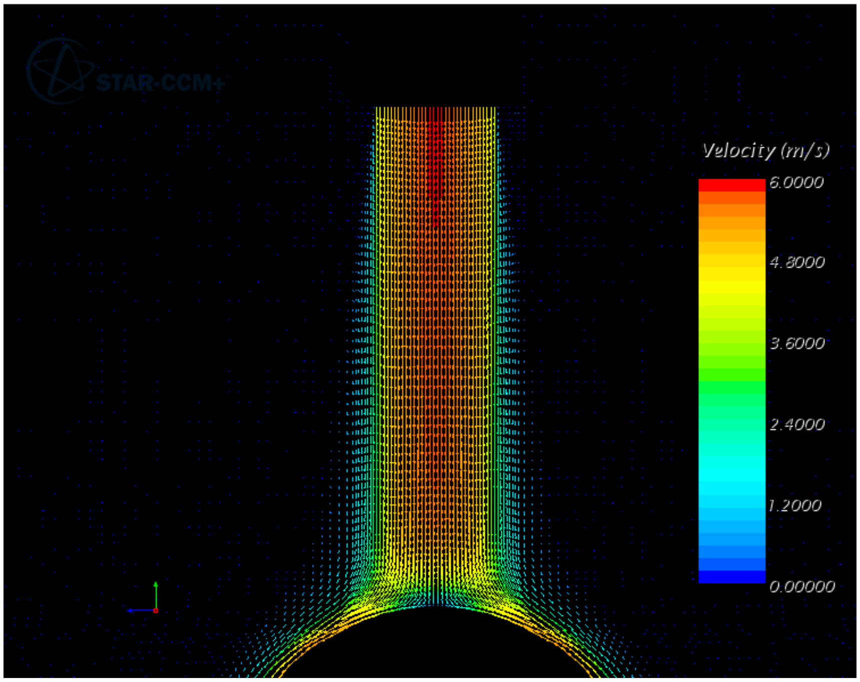

CFD Data, Re = 25 000, Standard *k*-*ω*